A.I. Alikhanyan National Science Laboratory
(Yerevan Physics Institute)

Karyan Gevorg Ararat

A study of charged hadron yields and the multidimensional nuclear attenuation effect at the HERMES experiment

DISSERTATION

Thesis for acquiring the degree of candidate of physical and mathematical sciences in division 01.04.16 "nuclear, elementary particles and cosmic ray physics"

Scientific supervisor:
doctor of physical and mathematical sciences, professor N.Z. Akopov

Contents

Introduction

Many centuries people were struggling to explain what everything around us is made of. It is not strange that the first debates on this held in Greece in one of the ancient centers of human civilization. The story starts with Thales(624 - 546 B.C.) from Miletus whose philosophy of nature based on the fundamental doctrine that water was the basis of all life and everything was made of water. As Arystotle says later "Of those who first philosophized the majority assumed only material principles or elements, Thales, the originator of such philosophy, taking water for his principle". This was the challenging achievement since he was the first, whome explanation of the world has shown scientific tendency based on "atomistic" view of everything in contrast with the ancient poets whose interpretations about the world were based on the mythical things.

The idea of the "atomistic" world then was developed by Anaximander(610 - 546 B.C.), the disciple of Thales, who also believed that all things originated from one original material element, the principle, but in opposition to his teacher, Anaximander assumed that this principle is undetermined in quality and infinite in quantity and he called it the aperion, translated as "limitless".

Then the disciple of Anaximander, the Anaximenes(585 - 528 B.C.) of Miletus, formulated his concept of the world based on the air as the first principle and fire, wind, clouds, water and earth produced from it by condensation and rarefaction.

But the "atomistic" ideas of Thales about the nature of matter around us were philosophically crystallized in 180 years later in works of Leucippus and Democritus(460 - 370 B.C) from Abdera who were known as the founders of the atomistic philosophy. As the Democritus quotes the Leucippus "The atomists hold that splitting stops when it reaches indivisible particles and

does not go on infinitely." The idea of the Democritus was based on a logic that if a matter could be infinitely divided, then it can never be put back together. Although a matter can be destroyed, it can also put back together by joining a simpler pieces which means the process of disintegration and reintegration is reversible. Hence, there must be a lower limit for the splitting of matter, otherwise it can be split infinitely, and nothing will be able to stop it from going on forever and destroying all matter.

The modern era of "atomistic" ideas starts with Newton(1642 - 1727) who in his "Principa" says " ... I am induced by many reasons to suspect that the phenomena of nature depends on certain forces by which the particles of bodies, by some causes hitherto unknown, are either mutually impelled towards each other cohere in regular figures, or are repelled and recede from each other, which forces being unknown philosophers have hitherto attempted the search of nature in vain." But still the atomic ideas were qualitative until an English chemist, John Dalton(1766 - 1844), in 1803 gave them a quantitative form in his work of "New System of Chemical Philosophy". The main idea of Dalton was that the atoms of the same element have identical properties and masses. And, as a consequence, it was possible to estimate the relative atomic weights measuring the relative combining weights of chemical elements, with various compounds, observed in nature.

But only more than ten years later, in 1815, William Prout(1785 - 1850) had observed that the relative atomic weights of the elements were very close to the numbers which are an integral multiples of hydrogen atoms. Based on this observation he hypothesized that atoms of all elements are the compounds of the hydrogen atoms. But more accurate measurements provided later showed that many of atomic weights did not have an integral values.

In 1833 Michael Faraday(1791 - 1867) found the laws of electrolysis showing in the first time that the electric charge is somehow associated with the atoms and also it has an atomistic structure.

With discovery of the radioactivity, in 1896, by the French physicist Henri Becquerel(1852 - 1908), the idea of "indivisible" atom seemed to be wrong. Becquerel found that uranium salts emit a penetrating radiation which have an influence on a photographic plate. More later, the Ernest Rutherford(1871 - 1937) discovered that there are different kinds of radiations. Some

of them are less penetrating than the rest. He called the less penetrating radiation the $\boldsymbol{\alpha}$ rays and the more powerful ones the $\boldsymbol{\beta}$ rays just using the first two letters of the Greek alphabet.

But finally the concept of "indivisible" atom broke down in 1897 when an English physicist J.J Thomson(1856 - 1940) pronounced the discovery of the electron, a unit of the electric charge, to be a constituent part of an atom. He calculated that the electron has to had a mass about 1837 times lighter than the mass of a hydrogen atom. In 1904, he proposed his "plum pudding" model of atom where negatively charged electrons, the "plums", are surrounded by positively charged "pudding", forming an electrically neutral atom.

But in 1911 Ernest Rutherford disproved Thomson's "plum-pudding" model of an atom in his famous gold-foil experiment where he showed that the atom has a very tiny, but massive, positively charged core, the nucleus. He proposed his model of atom known as the dynamic model (or planetary model in analogous with the solar sytem) according to which atoms consist of the nucleus surrounded by the negatively charged electrons. According to this model Rutherfort calculated that the angular distribution of the scattared $\boldsymbol{\alpha}$ particles should follow to $\sin^{-4}(\frac{\phi}{2})$, where $\boldsymbol{\phi}$ is the scattering angle. These calculations were done assuming that nucleus has no structure, it is a "point-like".

Continuing his experiments, in 1919, bombarding hydrogen and other light atoms with $\boldsymbol{\alpha}$ particles, Rutherford discovered the proton. He concluded, that positively charged particles produced in these reactions are nuclei of the hydrogen atoms. At this stage only two fundamental particles were known: the electron and the proton.

In 1930, bombarding beryllium atoms with $\boldsymbol{\alpha}$ particles, the German physicists Walther Bothe(1891 - 1957) and Hans Becker(1911 - 1944) observed a neutral radiation coming from the beryllium atoms. Then in 1932 the French physicists Frederic Juliot-Curie(1900 - 1958) and Irene Juliot-Curie(1897 - 1956) found that this radiation could eject protons from materials containing the hydrogen atoms.

In the same year, James Chadwick(1891 - 1974), repeated Juliot's experiment, directing beryllium radiation to the different materials such as lithium, beryllium and boron. He found that protons were ejected from nuclei of these elements too. According to his calculations the beryllium radiation was corespond to the neutral particles of approximately the same mass as

the proton. He had discovered the neutron.

The discovery of neutron alive the assumption proposed by the Heisenberg(1901 - 1976) and the Ivanenko(1904 - 1994) that the atomic nucleus consists of neutrons and protons and that the electrons in atoms are outside from the nucleus.

In 1950's, with development of the accelarator technologies when beam energies became much higher the deviations were observed from Rutherfort "point-like" nucleus assumption. The pionering experiment was done by Robert Hofstadter(1915 - 1990) and colleagues using the 125 MeV energy electron beam at the Stanford Linear Accelarator Center(SLAC). They measured the angular distribution of elastically scattered electrons from gold and observed a significant deviation from the "point-like" nucleus prediction. The Hofstadter and his team explained the observation as a combination of two effects. The first effect is corresponding to the scattering off a "point-like" target and the second effect caused by a spatial extension of target charge density which they called a "form factor". This was the clear indication that nucleus is not a "point-like" but has a size which they estimated to be a few fermi(1fm = 10^{-13} cm).

In 1964, Gell-Mann Murray and George Zweig, independently, had proposed that protons and other hadrons(strongly interacting particles) known at that time built from more basic blocks, which they called "quarks". Three years later, in 1967, MIT(Massachusetts Institute of Technology) - SLAC collaboration performed electron-proton elastic scattering which gave no evidence for quark substructure. In late 1967, they performed the first Deep Inelastic Scattering(DIS) experiment using 20 GeV electron beam and proton target. Data analysis showed that a DIS cross section(interaction probability) is decreasing very slowly with transfered four momentum squared(Q^2) than that for the elastic scattering. This was a clear indication of some hard core inside a proton.

As suggested first by the Bjorken in 1967, DIS experiments might being a tool to investigate an elementary constituents of matter. Subsequently, many DIS experiments are provided(ing) in various scientific laboratories to deepen our knowledge of matter constituents and a large variety of elementary particles.

Chapter 1

Physics Motivation

1.1 Deep-Inelastic Scattering(DIS)

A simple example of deep-inelastic scattering process might be the scattering of high energetic leptons(electrons, muons) on free nucleons, such as protons.

$$\mathbf{l(k) + N(P) \rightarrow l(k') + X} \tag{1.1}$$

Using an appropriate energy regime, one can suppress the weak interaction(due to the high masses of the exchange bosons) and thus only the electromagnetic interaction will be relevant. In one photon approximation, also known as the Born first approximation, an incoming charged lepton with four-momentum : $\mathbf{k}$($\mathbf{E}$, $\vec{\mathbf{k}}$) interacts, via a single virtual photon, with a proton, which in it's rest frame characterized by a four-momentum: **P(M, 0)**. A simple illustration diagram for this process is shown in Figure 1.1.

Detecting the scattered lepton with four-momentum : $\mathbf{k'}$($\mathbf{E'}$, $\vec{\mathbf{k'}}$), one can define the four-momentum transfer between the lepton and the proton as : $\mathbf{q = k - k'}$. Since the four-momentum of a virtual photon is a spaclike vector we can introduce the Lorentz invariant quantity : $\mathbf{Q^2 \equiv -q^2}$, as a negative squared four-momentum transfer from the lepton to the virtual photon. In order to touch the substructure of a nucleon(a "deepness" of the process) one needs to have a transfered momentum high enough than the mass of a nucleon : $\mathbf{Q^2 \gg M^2}$. In this regime it is possible to apply the **p**erturbative **Q**uantum **C**hromo**D**ynamics(**pQCD**)

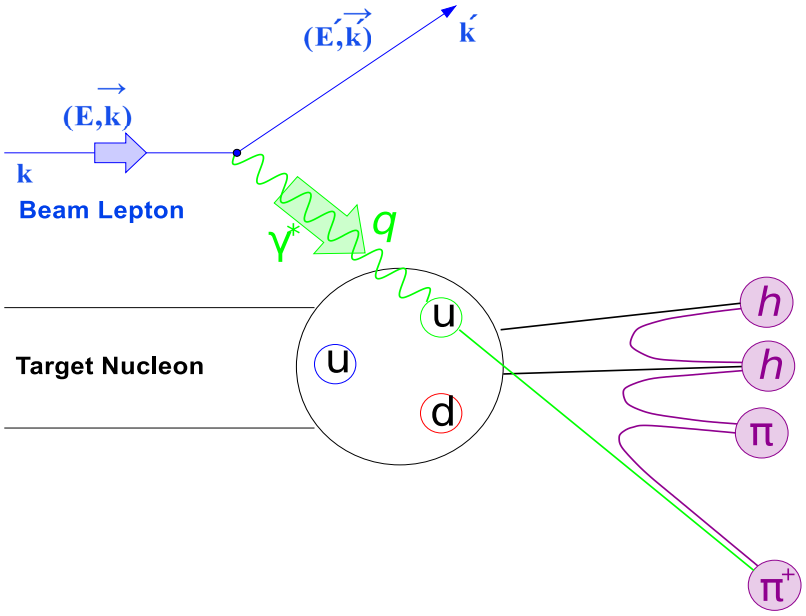

Figure 1.1: A simple illustration of deep-inelastic scattering process.

for the hard scattering process. The "inelasticity" of the process can be characterized by the invarint mass (or the invariant mass square) of the virtual photon-nucleon system which can be defined as : $\mathbf{W^2 = (P + q)^2}$ and it should be well above from a nucleon resonance region to consider the quark fragmentation only : $\mathbf{W^2 \gg M^2}$.

Let's consider a simple act of a lepton-nucleon **DIS** process. With increasing of the hard scattering scale : $\mathbf{Q}$, a lepton interaction with a nucleon can be considered as a superposition of independent scatterings on it's point-like consistuents: the quarks. The scattering time can be estimated by $\mathbf{1/Q}$ which at large $\mathbf{Q}$ allows to consider the quarks inside a nucleon as a non-interacting themselves. In this short time scale the virtual photon interacts with the frozen quarks distributed over the whole nucleon.

How we can estimate the cross-section for such a process? A very basic level is to start with a spin-less non-relativistic electron with mass $\mathbf{m}$ and let's assume it is moving in a potential field $\mathbf{V}(\vec{\boldsymbol{r}}, \mathbf{t})$. This motion is describing by the Schrödinger equation which in natural unit system $\mathbf{h = c = 1}$ can be written as :

$$\mathbf{i}\frac{\partial \boldsymbol{\psi}}{\partial \mathbf{t}} = (-\frac{\mathbf{1}}{\mathbf{2m}} \bigtriangledown^{\mathbf{2}} + \mathbf{V}(\vec{\boldsymbol{r}}, \mathbf{t}))\boldsymbol{\psi} \tag{1.2}$$

Having an assumption that we already know the solution of the Schrödinger equation

$$\mathbf{H}\boldsymbol{\psi} = \mathbf{E_k}\boldsymbol{\psi} \tag{1.3}$$

for a free particle :

$$\boldsymbol{\psi} = \sum_{\mathbf{k}} \boldsymbol{\chi}(\mathbf{t})\boldsymbol{\varphi}_{\mathbf{k}}(\vec{\boldsymbol{r}})\mathbf{e}^{-\mathbf{iE_k t}} \tag{1.4}$$

one can put then the solution (1.4) into the equation (1.2) and using the orthonormality of the eigenfunctions :

$$< \boldsymbol{\varphi}_{\mathbf{f}} \mid \boldsymbol{\varphi}_{\mathbf{i}} >= \mathbf{0} \tag{1.5}$$

we can integrate over the whole volume where the $\mathbf{V}(\vec{\boldsymbol{r}}, \mathbf{t})$ is nonzero and find the unknown coefficetns $\boldsymbol{\chi}(\boldsymbol{t})$:

$$\boldsymbol{\chi}(\mathbf{t}) = -\mathbf{i}\int_{-\boldsymbol{\zeta}}^{\boldsymbol{\zeta}} \mathrm{d}\mathbf{t} \int \mathrm{d}\vec{\boldsymbol{r}}\{\boldsymbol{\varphi}_{\mathbf{f}}(\vec{\boldsymbol{r}})\mathbf{e}^{-\mathbf{iE_f t}}\}^{*}\mathbf{V}(\vec{\boldsymbol{r}}, \mathbf{t})\{\boldsymbol{\varphi}_{\mathbf{i}}(\vec{\boldsymbol{r}})\mathbf{e}^{-\mathbf{iE_i t}}\} \tag{1.6}$$

Here we have considered a case that a particle is initialy in an unperturbed eigenstate $\mathbf{i}$ and an interaction takes place during a short time $\boldsymbol{\zeta}$ which leads to the change of the particle state to the final $\mathbf{f}$. The equation (1.6) can be written as :

$$\mathbf{T_{fi}} \equiv \boldsymbol{\chi}(\mathbf{t}) = -\mathbf{i}\int \boldsymbol{d}^{\mathbf{4}}\mathbf{x}\boldsymbol{\varphi}^{*}_{\mathbf{f}}(\mathbf{x})\mathbf{V}(\mathbf{x})\boldsymbol{\varphi}_{\mathbf{i}}(\mathbf{x}) \tag{1.7}$$

where $\mathbf{T_{fi}}$ is somthing related to the transition probability(transition amplitude) from eigenstate $\mathbf{i}$ to $\mathbf{f}$ and one can define a physically meaningfull value for the transition probability per unit time as :

$$\mathbf{W_{fi}} = \lim_{\boldsymbol{T}\to\boldsymbol{\infty}} \frac{\mid \mathbf{T_{fi}} \mid^{\mathbf{2}}}{\mathbf{T}} \tag{1.8}$$

Finally the integration over whole sets of initial and final states leads to the Fermi's golden rule

$$\mathbf{W_{fi}} = \mathbf{2}\boldsymbol{\pi} \mid \mathbf{M_{fi}} \mid^{\mathbf{2}} \boldsymbol{\rho}(\mathbf{E_i}) \tag{1.9}$$

where $\mathbf{M_{fi}}$ is a matrix element of the interaction caused by the potential $\mathbf{V}(\mathbf{x})$ which changes

the system state from $\mathbf{i}$ to $\mathbf{f}$ and $\boldsymbol{\rho}(\mathbf{E_i})$ is a density of an initial particle system in a diferent energy states.

Coming to the real case, consider a relativistic electron, which indeed has a spin and describes by the wave function :

$$\boldsymbol{\psi} = \boldsymbol{\varphi}(\mathbf{p})\mathbf{e}^{-\mathbf{i}\mathbf{p}_\mu \mathbf{x}^\mu} \tag{1.10}$$

Assume that this electron scatters on the electromagnetic field $\mathbf{A}_\mu$. Now it should satisfy the Dirac equation :

$$[\boldsymbol{\gamma^\mu}(\mathbf{i}\partial_\mu - \mathbf{e}\mathbf{A}_\mu) - \mathbf{m}]\boldsymbol{\psi} = \mathbf{0} \tag{1.11}$$

where the $\boldsymbol{\gamma^\mu}$ are the Dirac matrices. For this case the scattering amplitude can be defined as :

$$\mathbf{T_{fi}} = -\mathbf{i}\int \mathrm{d}^4\mathbf{x}\mathbf{j}^{\mathbf{fi}}_\mu \mathbf{A}^\mu \tag{1.12}$$

Here $\mathbf{j}_\mu$ is a charged current which can be written in the following way :

$$\mathbf{j}_\mu = -\mathbf{ie}\overline{\boldsymbol{\psi}}\boldsymbol{\gamma}^\mu\boldsymbol{\psi} \tag{1.13}$$

Let's assume a role of the electromagnetic potential plays an electromagnetic field of another charged lepton(like in electron-muon scattering). Here we have an interaction of two charged currents. In contrast to non-relativistic case for relativistic electron-muon scattering we should sum over the all spin states and using the charged current notation one can define the electron tensor as :

$$\mathbf{L}^{\mathbf{e}}_{\mu\nu} = \sum_{\mathbf{k}} [\overline{\boldsymbol{\varphi}}(\mathbf{p'})\boldsymbol{\gamma}^\mu\boldsymbol{\varphi}(\mathbf{p})][\overline{\boldsymbol{\varphi}}(\mathbf{p'})\boldsymbol{\gamma}^\nu\boldsymbol{\varphi}(\mathbf{p})]^* \tag{1.14}$$

The similar thing can be defined for the muon. The cross section for such a scattering will be proportional to :

$$\boldsymbol{\sigma} \sim \mathbf{L}^{\mu\nu}_{\mathbf{electron}}\mathbf{L}^{\mathbf{muon}}_{\mu\nu} \tag{1.15}$$

Finally coming to electron-nucleon scattering the only thing to do is to replace the muonic

tensor by the hadronic tensor $\mathbf{W}_{\mu\nu}$:

$$\boldsymbol{\sigma} \sim \mathbf{L}^{\mu\nu}_{\mathbf{electron}} \mathbf{W}^{\mathbf{nucleon}}_{\mu\nu} \tag{1.16}$$

But the situation here is more complicated because the hadronic tensor can not be calculated theoretically but only measured experimentally. For the inelastic electron-nucleon scattering assuming that the scattered lepton is not polorized the hadronic tensor can be represented by the inelastic structure functions as follows :

$$\mathbf{W}_{\mu\nu} = \mathbf{W_1 g}_{\mu\nu} + \mathbf{W_2 p}_\mu \mathbf{p}_\nu + \mathbf{W_4 q}_\mu \mathbf{q}_\nu + \mathbf{W_5}(\mathbf{p}_\mu \mathbf{p}_\nu + \mathbf{q}_\mu \mathbf{q}_\nu) \tag{1.17}$$

The gauge invariance and the current conservation lead only two independent inelastic structure functions $\mathbf{W_1}$ and $\mathbf{W_2}$ which then can be measured in **DIS** process. This information is very important in understanding of the structure of a nucleon.

In case of semi-inclusive deep-inelastic scattering(**SIDIS**) process, in addition to the scattered lepton we are detecting the produced hadrons($\mathbf{h}$) as well.

$$\mathbf{l(k) + N(P) \to l(k') + h + X} \tag{1.18}$$

According to the factorization theorem[1] and using leading order **QCD** approximation we can write a cross section for such a process in the following way :

$$\boldsymbol{\sigma}^{\mathbf{eN \to ehX}} \propto \sum_{\mathbf{f}} \mathbf{e_f^2} \cdot \mathbf{q_f(x_{Bj}, Q^2, P_T)} \otimes \boldsymbol{\sigma}^{\mathbf{eq \to eq}} \otimes \mathbf{D_f^h(z_h, Q^2, K_T)} \tag{1.19}$$

where $\mathbf{e_f}$ is an electric charge of a quark with flavor $\mathbf{f}$, $\mathbf{q_f(x_{Bj}, Q^2, P_T)}$ is the parton distribution function(**PDF**), $\boldsymbol{\sigma}^{\mathbf{eq \to eq}}$ is the hard scattering cross-section and $\mathbf{D_f^h(z_h, Q^2, K_T)}$ is the quark fragmentation function. Here $\mathbf{P_T}$ is a parton transverse momentum inside a nucleon and $\mathbf{K_T}$ is the intrinsic transverse momentum of a parton inside a produced hadron. In contrast to the hard scattering cross section a parton distribution functions and a quark fragmentation functions are non-perturbative objects and they can be only measure in experiment. Considering the collinear factorization only when we integrate over quark transverse momentum there is a believe that

these functions are universial[2] which means they can be extracted from different processes like semi-inclusive electron-positron anihilation and proton-proton hard scattering. On the other hand, going from free nucleon to the nucleuse and considering a hadron production in a nuclear medium one can investigate a possible modification of these fragmentation functions inside a nuclear environment.

1.2 Hadronization in Nuclear Enviorement

The process of hadronization is not yet fully understood. The key tool is the nuclear **DIS** experiment like lepton-nucleon(in nuclear target) scattering and the usage of the **Quark-Parton Model**(**QPM**) as a theoretical framework. The first measurement was performed by **SLAC**[3] using a **20.5 GeV** electron beam and liquid hydrogen, liquid deuterium, beryllium, carbon and copper targets. They found the effect of attenuation for forward hadrons which was increasing with atomic mass of the target. Then the same effect was studied in the **EMC** collaboration[4] with much higher beam energies using deutron, carbon, copper and tin targets. They observed that nuclear attenuation is very small for very high energies of a virtual photon and a hadron transverse momentum was broadened in the nuclear targets. More recently the new studies for the nuclear attenuation effect were performed by the **HERMES** collabortion at **DESY**[5] and the **CLAS** collaboration at **JLAB**[6]. Despite the large variety of experimental data mentioned above the main part of them are extracted within the so-called one dimensional approach or in very limited kinematic regimes which means the possible correlations between different kinematical variables are averaged. The same is true for the phenomenological models which use the parameterization of the available experimental data in one-dimension. Anyway there are some attempts to parametrize non one-dimensional data[7] based on the **HERMES** previous publication which has the first attempt to make slices on another kinematic variable for pions[5]. In this sense the new multidimensional approach to study the nuclear attenuation effect for charge separated pions, kaons and protons is very important to check the existing models and make new parametrizations.

There are several models to explain a dynamics of the quark-gluon interactions in semi-inclusive deep-inelastic scattering process. The commonly used one is the **LUND string**

fragmentation model[8]. According to this model the quark-atiquark pair moving apart from their common vertex forming a colour tube with transverse dimensions of order of typical hadronic size about **1 fm**. The energy density along the tube lenght is deduced to be **1 fm/c** and within the assumption of uniformity of energy distribution along it's lenght one gets a linearly increasing potential with further development of string due to the **QCD** confinement.

The hadron formation process or quark fragmentation into hadrons happens too late(due to the **Lorentz dilation effect**) hence the final hadron carries almost no information about the initial stage of the process. In this sense, using a nuclear target, it is possible to touch on the very initial step of the hadronization and investigate it's development up to several fermi distances[9]. A simple space-time development diagram for the hadronization process is shown in Figure 1.2 : Here the process of hadronization is considered in two time

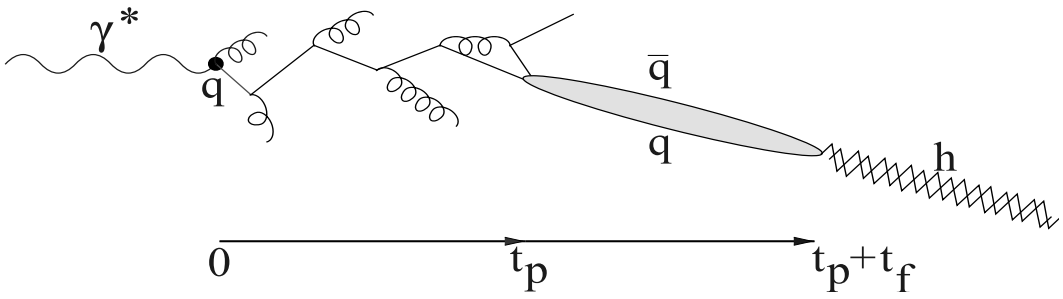

Figure 1.2: A simple diagram for the space-time development of the hadronization process.

scales : the partonic scale which describes by a production time $\mathbf{t_p}$, where the partonic effects(**gluon radiation,parton rescattering**) take place and the hadronic scale when the colorless pre-hadron state is already formed and it can interact with the surrounded nuclear medium(**colorless pre-hadron interaction**, **final state interaction** : **FSI**) during a formation time $\mathbf{t_f}$. These two effects together lead to the nuclear attenuation effect which experimentally can be observed considering **DIS** normalized hadron yields produced from nuclear target heavier than deuterium compared with the last one. The experimental observable called the hadron multiplicity ratio and reads as :

$$\mathbf{R_A^h(\nu, Q^2, z, p_t^2) = \frac{(\frac{N^h(\nu,Q^2,z,p_t^2)}{N^e(\nu,Q^2)})_A}{(\frac{N^h(\nu,Q^2,z,p_t^2)}{N^e(\nu,Q^2)})_D}} \tag{1.20}$$

where $\mathbf{N^h}$ is the number of semi-inclusive hadrons in a given $(\boldsymbol{\nu}, \mathbf{Q^2}, \mathbf{z}, \mathbf{p_t^2})$ bin and $\mathbf{N^e}$ is the number of inclusive deep-inelastic scattered leptons in the same $(\boldsymbol{\nu}, \mathbf{Q^2})$ bin. This ratio depends on leptonic variables such as the energy of virtual photon $\boldsymbol{\nu}$ and it's virtuality $\mathbf{Q^2}$ and on hadronic variables like the fraction $\mathbf{z}$ of the virtual photon energy carried by the produced hadron and the square of the hadron momentum component $\mathbf{p_t^2}$ transverse to the virtual photon direction.

The lack of a complete theory for the hadronization process leads to the phenomenological approach for quark fragmentation into hadrons, furthermore, in nuclear medium possible modifications caused by a surrounded nuclear environment are happen, thus an experimental data play a crucial role to study this process and to make predictions for further studies by making various parameterizations.

1.2.1 The Two-Scale Model

This model proposed by the **EMC**[4] collaboration, which then developed by **YerPhI HERMES** group[10], is the string model. It based on the formula :

$$\mathbf{R_A} = \mathbf{2\pi} \int_{\mathbf{0}}^{\infty} \mathbf{bdb} \int_{\infty}^{\infty} \mathbf{dx} \boldsymbol{\rho}(\mathbf{b}, \mathbf{x}) [\mathbf{1} - \int_{\mathbf{x}}^{\infty} \mathbf{dx'} \boldsymbol{\sigma}^{\mathbf{str}}(\boldsymbol{\Delta}\mathbf{x}) \boldsymbol{\rho}(\mathbf{b}, \mathbf{x'})]^{\mathbf{A-1}} \tag{1.21}$$

where the $\mathbf{b}$ is an impact parameter, $\mathbf{x}$ and $\mathbf{x'}$ are the longitudinal coordinates of the **DIS** and string-nucleon interaction points respectively, $\boldsymbol{\sigma}^{\mathbf{str}}(\boldsymbol{\Delta}\mathbf{x})$ is the string-nucleon cross section on distance $\boldsymbol{\Delta}\mathbf{x}$, $\boldsymbol{\rho}(\mathbf{b}, \mathbf{x})$ is the nuclear density function and finally $\mathbf{A}$ is an atomic mass number. The hadronization process within this model described by two time(length) scales : constituent formation time(length) $\boldsymbol{\tau}_\mathbf{c}$ $(\mathbf{l_c})$ and a formation time(length) of colorless system $\boldsymbol{\tau}_\mathbf{h}(\mathbf{l_c})$ with valence content and quantum numbers of final hadron without a sea partons. There is a simple link between $\boldsymbol{\tau}_\mathbf{c}$ and $\boldsymbol{\tau}_\mathbf{h}$:

$$\boldsymbol{\tau}_\mathbf{h} - \boldsymbol{\tau}_\mathbf{c} = \frac{\mathbf{z}\boldsymbol{\nu}}{\mathbf{k}} \tag{1.22}$$

where $\mathbf{k}$ is the string tension. The important thing to mention is, a non-monotonous behaviour of string-nucleon cross section within this model which has a jump at $\boldsymbol{\Delta}\mathbf{x} = \boldsymbol{\tau}_\mathbf{c}$ and $\boldsymbol{\Delta}\mathbf{x} = \boldsymbol{\tau}_\mathbf{h}$

because the string-nucleon cross section reads as :

$$\boldsymbol{\sigma^{str}(\Delta x) = \theta(\tau_c - \Delta x)\sigma_q + \theta(\tau_h - \Delta x)\theta(\Delta x - \tau_c)\sigma_s + \theta(\Delta x - \tau_h)\sigma_h} \tag{1.23}$$

where $\boldsymbol{\sigma_q}$ is a cross section of an initial string with nucleon, $\boldsymbol{\sigma_s}$ is an open string-nucleon cross section and $\boldsymbol{\sigma_h}$ is the hadron-nucleon cross section. But in reality, we are expecting to have a cross section which is increasing monotonously until it reaches the size of hadronic cross section. To satisfy a smooth enhancement of the cross section on can introduce a parameter **c** which lies between **0** and **1**, within an assumption that the string starts to interact with hadronic cross section when the first constituent quark of final hadron is already created. What happens after **DIS** point is the enhancement of the string-nucleon cross section until it becomes a hadron-nucleon cross section at point $\boldsymbol{\Delta x = \tau}$. But at this region $\boldsymbol{\Delta x \sim \tau}$ perturbative **QCD** is not able to give an exact formula for $\boldsymbol{\sigma^{str}}$ that is why one has to use some model prediction for this region. One of the models used here based on the quantum diffusion :

$$\boldsymbol{\sigma^{str}(\Delta x) = \theta(\tau - \Delta x)[\sigma_q + (\sigma_h - \sigma_q)\Delta x/\tau] + \theta(\Delta x - \tau)\sigma_h} \tag{1.24}$$

here $\boldsymbol{\tau = \tau_c + c\Delta\tau}$ and $\boldsymbol{\Delta\tau = \tau_h - \tau_c}$.
There are also two different representations of $\boldsymbol{\sigma^{str}}$ within this model :

$$\boldsymbol{\sigma^{str}(\Delta x) = \sigma_h - (\sigma_h - \sigma_q)e^{-\frac{\Delta x}{\Delta\tau}}} \tag{1.25}$$

and

$$\boldsymbol{\sigma^{str}(\Delta x) = \sigma_h - (\sigma_h - \sigma_q)e^{-(\frac{\Delta x}{\Delta\tau})^2}} \tag{1.26}$$

which are turn into (1.24) with $\boldsymbol{\frac{\Delta x}{\Delta\tau} \ll 1}$.

On the other hand for the nuclear density function(**NDF**), the Shell model is used for $\boldsymbol{^4He}$ and $\boldsymbol{^{14}N}$ which assumes that two protons together with two neutrons fill the s-shell and the remaining **A-4** nucleons are on the p-shell. The **NDF** in this model reads :

$$\boldsymbol{\rho(r) = \rho_0(r)(\frac{4}{A} - \frac{2}{3}\frac{A-4}{A}\frac{r^2}{r_A^2})e^{-\frac{r^2}{r_A^2}}} \tag{1.27}$$

In case of ^{20}**Ne**, ^{84}**Kr** and ^{131}**Xe** the **Woods-Saxson distribution** is used for the nuclear density function :

$$\boldsymbol{\rho(r) = \frac{\rho_0(r)}{(1 + e^{\frac{r - r_A}{a}})}} \tag{1.28}$$

where $\mathbf{a = 0.545fm}$ and the $\boldsymbol{\rho_0(r)}$ can be determined from normalization condition :

$$\boldsymbol{\int d^3 r \rho(r) = 1} \tag{1.29}$$

The comparison of the model predictions with the **HERMES** one dimensional nuclear attenuation data for different nuclear targets for charged pions is shown in Figure 1.3 :

N. Akopov et al. / Eur. Phys. J. C(2010): 5-14

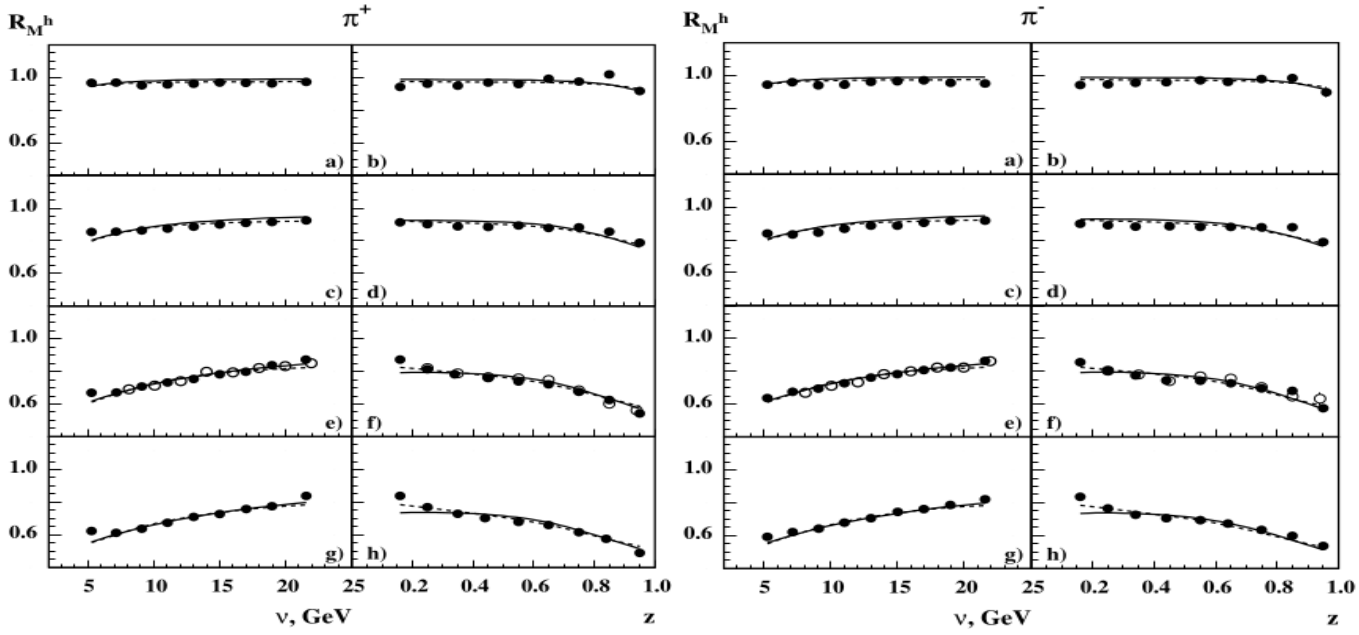

Figure 1.3: One dimensional **HERMES** data. Hadron multiplicity ratio for positively charged pion as a function of a virtual photon energy $\boldsymbol{\nu}$(the first column, left plot) and an energy fraction of a virtual photon $\mathbf{z}$ carried by the produced hadron(the second column left plot) and negatively charged pion(right plot) comparison with the improved two-scale model for helium(a,b), neon(c,d), krypton(e,f) and xenon(g,h) targets. The dashed and solid curves correspond to the different choices of the constituent formation length.

In Figure 1.4 the nuclear attenuation effect for charged kaons from different nuclear targets are shown with comparison of the improved two-scale model.

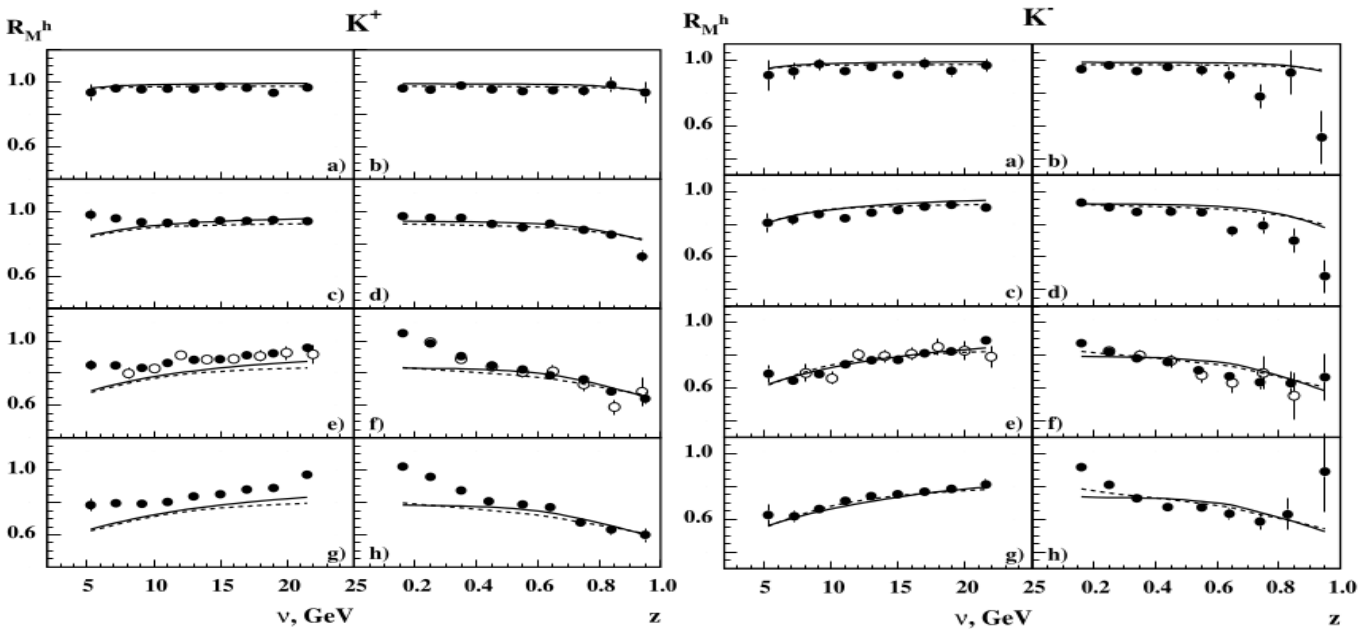

Figure 1.4: The same as described in caption of the Figure 1.3 but now its for the charged kaons.

In these calculations the proton data are not included because an influence of the additional mechanisms such as color interaction(string-flip) and the final hadron rescattering are essential for them which are not considered within this model.

1.2.2 Gluon Bremmstrahlung Model(GBM)

In this model[11] the hadron production is considered as a result of the highly virtual quark which formed in **DIS** process. The dominant role in energy losses plays the absorbtion of the colorless prehadron state in the nuclear medium. Due to the hardness of the process (**DIS**) the gluon bremsstrahlung also can play an essential role for energy losses. This radiation energy loss increasing linearly with path lengh **L** :

$$\mathbf{E_{rad}} = \frac{\mathbf{2}}{\mathbf{3\pi}}\boldsymbol{\alpha}_\mathbf{s}(\mathbf{Q^2})\mathbf{Q^2L} \tag{1.30}$$

The main question here has to be ansewerd is how much time this radiation takes? The emission time for a gluon with a part of quark's momentum $\boldsymbol{\alpha}$ which has a transverse momentum $\mathbf{k_t}$ can

be estimated as :

$$\mathbf{t_{radiation}} \approx \frac{\mathbf{2\nu}}{\mathbf{k_t^2}}\boldsymbol{\alpha}(\mathbf{1}-\boldsymbol{\alpha}) \tag{1.31}$$

To form a leading hadron each radiated gluon can be considered as a quark-antiquark pair and the fastes pair will produce a leading hadron later.

B.Z. Kopeliovich et al. / Nuclear Physics A 740 (2004) 211-245

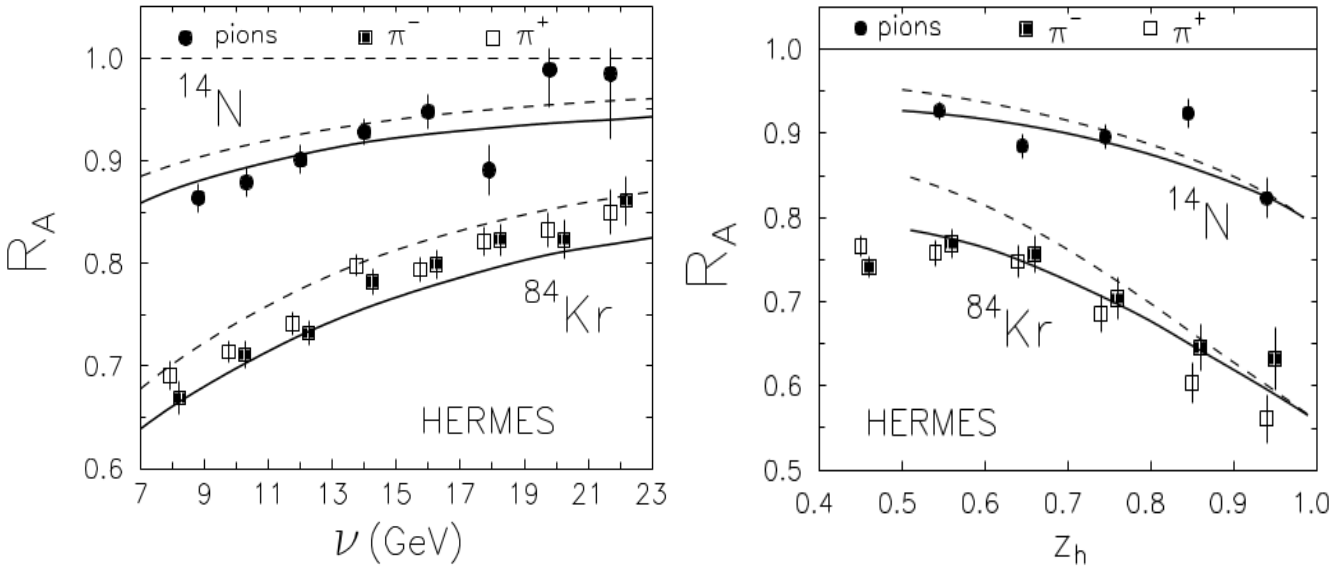

Figure 1.5: The **HERMES** one dimensional data comparison with **GBM** model predictions for charged pions from nytrogen and krypton targets. The solid and dashed curves correspond to calculations with and without the effects of induced radiation, respectively.

When a time required for a quark to neutralize it's colour (**production time**) is large, the non-perturbative effects are dominated, hence to describe the hadronization process perturbatively one should consider fast hadrons i.e. hadrons with $\mathbf{z_h > 0.5}$. The produced colorless object, the prehadron needs a time(**formation time**) proportional to the hadron energy $\mathbf{z_h\nu}$ to form a final state hadron. If the leading hadron produced with fractional energy $\mathbf{z_h \to 1}$ the gluon radiation is not allowed due to the energy conservation, leading to the **Sudakov's suppression effect**. The model predictions compared with the **HERMES** one dimensional data are presented in the Figure 1.5.

1.2.3 Rescaling Models(RM)

In **RMs** (also known as deconfined models) the gluon radiation effect and the absorbtion of produced hadrons taken into account[12]. In **semi-inclusive DIS**(**SIDIS**) process, due to the factorization, the cross section can be factorized into parton distribution functions(**PDF**) and the quark fragmentation functions (**FF**). If a $\boldsymbol{\lambda}$ is the confinement scale then $\mathbf{Q^2 \sim 1/\lambda^2}$ and according to the deconfined models the $\boldsymbol{\lambda}_A$ confinement scale for nucleons inside a nucleus should be greater than this for a free nucleon $\boldsymbol{\lambda}_0$.

$$\boldsymbol{\lambda_A > \lambda_0} \tag{1.32}$$

Since both **PDF** and **FF** are $\mathbf{Q^2}$ dependent, now due to the change of the confinement scale

A. Accardi et al. / Nuclear Physics A 720 (2003) 131-156

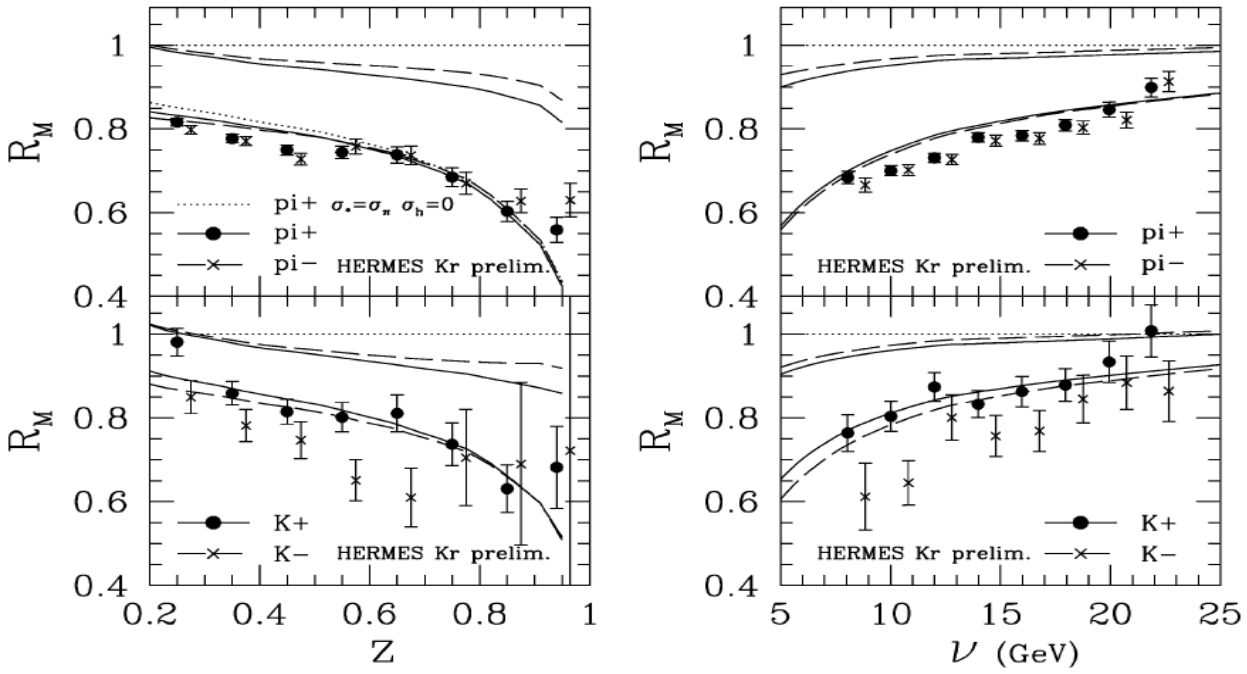

Figure 1.6: The **HERMES** multiplicity ratio for charged pions and kaons compared with the rescaling model. The uper pair of curves includes rescaling without absorbtion for pisitively and negatively charged particles and the lower pair includes rescaling and also the nuclear absorbtion by Bialas-Chmaj(BC) model.

this dependence should be rescalad as :

$$\mathbf{Q^2} \equiv (\frac{\boldsymbol{\lambda_A}}{\boldsymbol{\lambda_0}})^2 \mathbf{Q^2} \tag{1.33}$$

Taking into account also the $\mathbf{Q^2}$ dependence of **QCD coupling constant** the modification can be done as :

$$\mathbf{q_f^A}(\mathbf{x}, \mathbf{Q^2}) = \mathbf{q_f}(\mathbf{x}, \xi_\mathbf{A}(\mathbf{Q^2})\mathbf{Q^2}) \tag{1.34}$$

$$\mathbf{D_f^A}(\mathbf{z}, \mathbf{Q^2}) = \mathbf{D_f}(\mathbf{z}, \xi_\mathbf{A}(\mathbf{Q^2})\mathbf{Q^2}) \tag{1.35}$$

With good approximation the **DIS** normalized hadron yeilds can be considered as a key to touch on the fragmentation functions. In this sense the behavior of hadron multiplicity ratio $\mathbf{R_A^h}$ can be interpreted as a consequence of such a modification. It is assumed that this approach is available for the kinematic range $\mathbf{z \geq 0.1}$ and $\mathbf{0.1 < x_{Bj} < 0.6}$. In Figure 1.6 the comparison of the model with the **HERMES** krypton data is provided.

1.2.4 BUU (Boltzmann-Uehling-Uhlenbeck) Transport Model

To describe the nuclear **DIS** process within the **BUU** model[13], the lepton-nucleuse interaction considered in two steps. At first there is an interaction between high energetic virtual photon with bounded nucleon inside a nucleus. This performed by the **PYTHIA** and **FRITIOF** generators for two invariant mass ranges of the virtual photon-nucleon system : $\mathbf{W > 4\ GeV}$ and $\mathbf{2 < W < 4\ GeV}$ respectively. For a nucleon in a nuclear medium the possible nuclear effects are also considered such as **binding energy**, **Fermi motion** and **nuclear shadowing**. Then the coupled-chanel transport model used to describe the propogation of a final state through the nuclear medium. The important thing has to be mentioned is the different interpretations of the pre-hadron states in **LUND** and in **transport** models. This difference caused by the production time concept in this two approaches. In the **Lund** model it depends on the momentum of the string fragments while in the transport model the string decays into color neutral pre-hadrons instantaneously. Therefore, here the hadron production describes only with one scale, the formation time, when the interaction with nuclear medium

happens only by the beam and the target remnants. The formation time assumed to be a constant in the hadron rest frame. During this time the pre-hadron interacts with surrounding nuclear medium with a cross section which can be determined using the constituent quark model.

$$\boldsymbol{\sigma^*_{\mathbf{prebaryon}}} = \frac{\mathbf{n_{org}}}{\mathbf{3}}\boldsymbol{\sigma_{\mathbf{baryon}}}, \qquad \boldsymbol{\sigma^*_{\mathbf{meson}}} = \frac{\mathbf{n_{org}}}{\mathbf{2}}\boldsymbol{\sigma_{\mathbf{meson}}} \tag{1.36}$$

where $\mathbf{n_{org}}$ is the number of (anti)quarks the pre-hadron consists which coming from beam or a target. This means that for the vacuum created quark-antiquark pairs which formed a hadron there is no interaction considered during the formation trime and those hadrons are move freely in nuclear medium. Figure 1.7 shows the comparison of **BUU** model with the **HERMES** data for pions, kaons and protons.

T. Falter et al. / Phys. Rev. C 70, 054609 (2004)

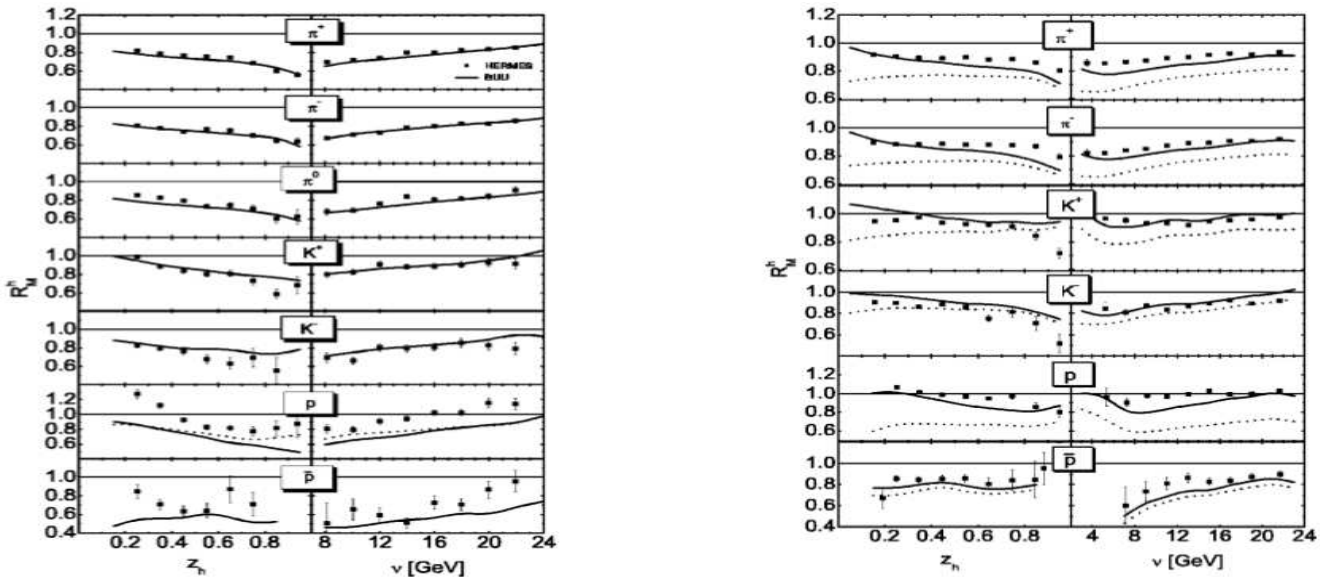

Figure 1.7: The **HERMES** multiplicity ratio from for different hadron species from krypton(left) and neon(right) plots compared with **BUU** model simulations. The solid line represents the results of simulation where the constituent quark concept for the prehadronic cross section is used and a formation time is selected to be 0.5 fm/c. The dotted line on the left plot for the proton spectrum indicates the result of simualtion for virtual photon-nucleon scattering by PYTHIA and the dotted line on the right plot represents the result of a simualtion with a purely absorptive treatment of the final state interaction.

Chapter 2

The HERMES Experiment

The **HERA** measurement of spin (**HERMES**) data-taking program started in **1995** on **HERA** acclereator at **DESY** in **Hamburg**. It was one of the four experiments on **HERA** and had a goal to measure the spin structure of a nucleon. More than ten years of operation(the data-taking was stopped in 2007) it had acumulated a large variaty of data allowing to investigate different aspects of the **DIS** process. The lepton ring used at **HERMES** stored

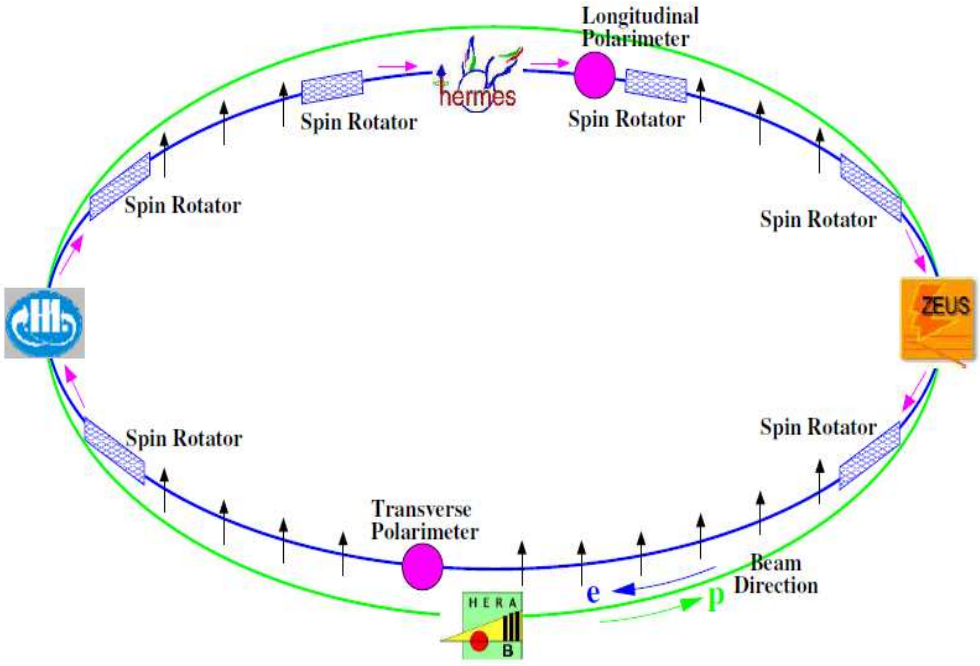

Figure 2.1: Schematic view of the **HERA** beam line with four experiments **HERMES**,**ZEUS**,**H1** and **HERA B**.

electrons or positrons at an energy of **27.6 GeV** with typical beam current between **30-50**

mA. In Figure 2.1 the scheme of the **HERA** accelerator is shown with four experimental halls.

2.1 The target system

The **HERMES** experiment uses a target[14] system with abilities to operate with pure gaseous **H**, **D**, **He**, **Ne**, **Kr**, **Xe** in polorized(**H**,**D**) and unpolorized(**H**,**D**,**He**,**Ne**,**Kr**, **Xe**) modes. It is internal to the beam line(see Figure 2.2) with **40 cm** long storage cell which is cooling up to **70 K** and has an elliptical cross section of **9.8 x 24 mm^2**. To provide as much areal density as possible the gas injected to the storage cell aligned collinear to the beam line.

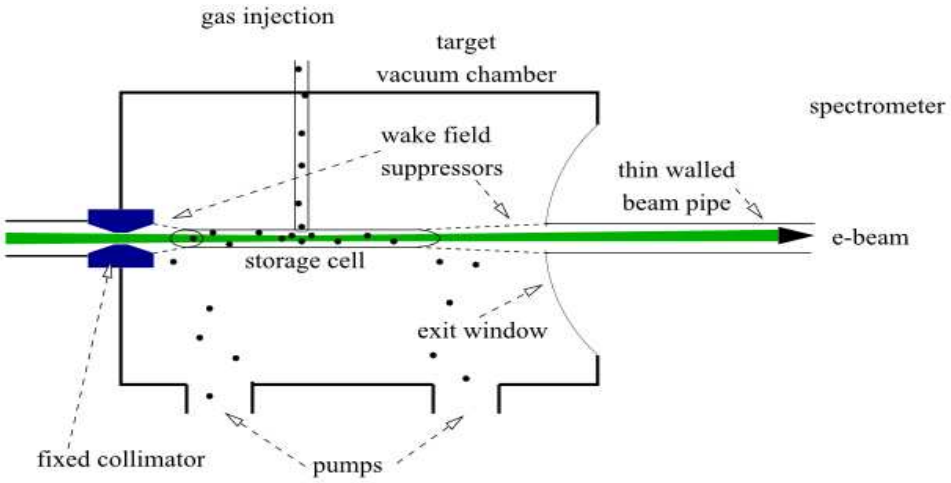

Figure 2.2: The **HERMES** target system.

This allowes to get a target density up to $\sim$ **10^{16}** nucleons per **cm^2** for polorized hydrogen and deuterium targets.

2.2 The HERMES spectrometer

The **HERMES** spectrometer[15] is the forward angle spectrometer with angular acceptance of $\pm$**(40 - 140) mrad** in vertical and $\pm$ **170 mrad** in horizontal directions(see Figure 2.3). The **HERMES** coordinate system has a **z** axis along the beam lepton momentum with coordinate zero in the center of target cell. The **xy** axis construct in such a way that **y** pionts to the up direction and **x** points to the left when looking to the downstream of the beam pipe. The spectrometer consists of two detector subsystems : the tracking system which provides particle

track reconstruction and the particle identification(**PID**) system : to separate leptons from hadrons and ability to identify between different hadron flavors.

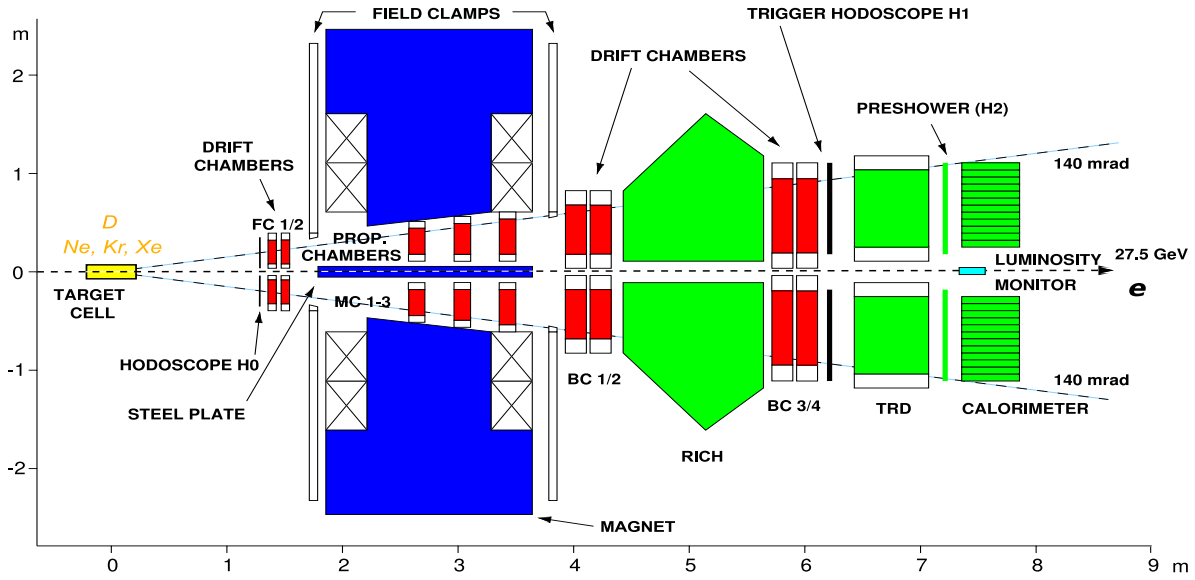

Figure 2.3: The **HERMES** spectrometer(tracking detectors in red and **PID** detectors in green).

2.2.1 The Spectrometer Magnet

The **HERMES** spectrometer has a dipole magnet with integrated deflecting power equal to **1.3 Tm**. To avoid from possible influence of the spectrometer magnet on the **HERA** beam, the beam pipe is shielded by **11 cm** thick septum steel plate which limits the lower vertical acceptance of the spectrometer to $\pm$**40 mrad**. On the other hand the spectrometer magnet limits the upper acceptance in the vertical direction in $\pm$**(140) mrad** window.

2.2.2 Tracking Detectors

In order to reconstruct a particle track the tracking chambers are used which are placed in front of the magent inside the magnet and behind the magnet. They are the wirechambers except the silicon detector which is installed right after the target. The goal of the tracking system is to provide a determination of the origin, angles and momentum of charged particle tracks.

The Silicon Detector

To increase the acceptance for long-living particles such as $\mathbf{\Lambda, \Lambda_c, K_s}$ the silicon detector[16] was installed. In this analisys the data from this detector is not used.

The Drift Vertex Chambers (DVC)

The goal of **DVC** chambers was to improve the momentum resolution. They have a **200** $\boldsymbol{\mu}$**m** spatial resolution with **2 mm** wire spacing.

The Front Chambers (FC)

The front chambers[17] were used to reconstruct the front tracks. They filled with a gas mixture $\mathbf{Ar/CO/CH_4}$ and consist of two modules with **7 mm** width and **8 mm** depth. The spatial resolution provided by these chambers is **225** $\boldsymbol{\mu}$**m** and the efficiencies are varied between $\mathbf{97-99\%}$ depending on the position in the cell.

The Magnet Chambers (MC)

The magnet chambers[18] were installed inside the spectrometer magnet gap. There were three sets of wire chambers allowing to reconstruct a momentum of low energy particles which have been not reached to the back part of the spectrometer.

The Back Chambers (BC)

In order to reconstruct a particle tracks behind the spectrometer magnet the two sets of back chambers[19] were installed in front of and behind the **Ring-Imaging Čerenkov** detector. They had the spatial resolution **210** $\boldsymbol{\mu}$**m** for the first set($\mathbf{BC1/2}$) and **250** $\boldsymbol{\mu}$**m** for the second set($\mathbf{BC3/4}$). The efficiency for the lepton track is about **99%** while for hadron track it is a bit lower : **97%** which caused by the lower ionization for hadrons compared with the leptons.

In Figure 2.4 a schematic view for short and long tracks reconstructed by the HERMES tracking system is shown.

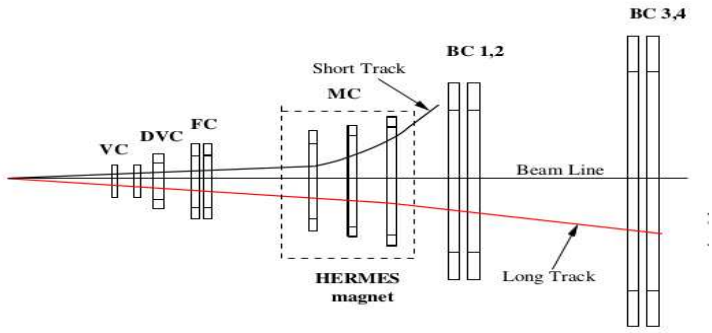

Figure 2.4: A **long**(in red) and **short**(in black) track reconstruction by the **HERMES** tracking system.

2.2.3 Particle Identification (PID)

The aim of the **HERMES** particle identification system is to identify the tracks reconstructed by the tracking system. In this sense the first thing to do is to distinguish a lepton track from a hadron track. The idea is to use different detectors taking into account the fact that a lepton(either electron or positron) and a hadron will have a different energy deposites in these detectors thus one can separate between lepton and hadron tracks combining the results from different detectors with the unified algorithm called as **PID** algorithm.

The Transition Radiation Detector (TRD)

When the particles travers the boundary of two different media with different dielectric indices the transition radiation emits and the intensity of this radiation depends on the **Lorentz factor** ($\boldsymbol{\gamma = E/mc^2}$). The usage of a multilayer radiator **TRD** allowes to use the threshold condition to distinguish between different particles. The electron/positrons exceed threshold which is around $\boldsymbol{\gamma \sim}$ 1000 at energies greater than **0.5 GeV** while for the lightest hadron : the pion this limit is around **140 GeV** due to about two order mass differences between them.

The **HERMES T**ransition **R**adiation **D**etector consists by six identical layers each of which constructed with a fiber radiator and a wire chamber. Each track being either lepton or hadron has an energy deposition in wire chamber and with combination of the transition radiation it turns out that the energy deposit for leptons is twice larger than for the hadrons.

The Calorimeter

The **HERMES** has a lead glass **electromagnetic calorimeter** consisted of **420** radiation blocks[20]. The particles deposit their energy in the calorimeter making electromagnetic showers which for leptons caused the loss of the almost all their energy. This means that the energy deposit to momentum ratio for leptons will be very close to unity while for hadrons this value is about two times smaller.

On the other hand the calorimeter allowes to reconstruct electroneutral particles such as $\boldsymbol{\pi^0}$ and $\boldsymbol{\eta}$ mesons registerating a decay components: the photons. It is also used as a fast first-level trigger for scattered beam leptons.

The Preshower Detector

The **HERMES** hodoscope system which used for the triggering consists of three hodoscopes : **H0**, **H1** and **H2** where **H2**: **the preshower** provides also the **PID** information. It has **11 mm** lead between **1.3 mm** stainless steel sheets which leads a very small energy deposition for hadrons at the level of few **MeV** while for leptons the energy deposition in magnitude is one order higher.

2.2.4 The RICH Detector

The **HERMES RICH** detector[21] provides the identification of charged hadrons such as pions, kaons, protons and antiprotons in momentum range : $\mathbf{2\ GeV < p_h < 15\ GeV}$. It uses the Čerenkov radiation effect i.e. the radiation of a relativistic, charged particles moving through the medium with velocities greater than the velocity of the speed in the same medium:

$$\mathbf{v > c/n} \tag{2.1}$$

where **n** is the refractive index of the medium and **c** is the speed of light. The angle of Čerenkov radiation depends on a particle velocity and the medium refractive index and can be written as :

$$\mathbf{cos\theta = c/nv} \tag{2.2}$$

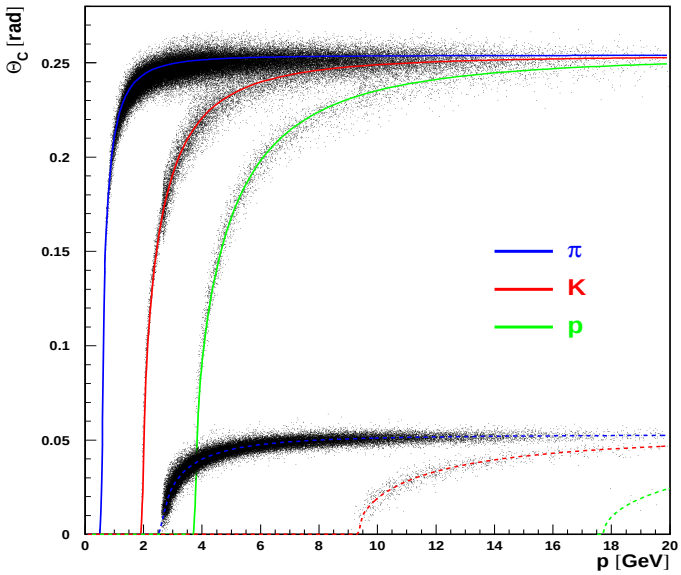

Figure 2.5: Momentum dependence of the Čerenkov angle for different hadron types and radiators. The upper band corresponds to the aerogel and the lower band to the C_4F_{10} gas respectively.

Thus particles with the same momentum will have a different radiation angles depending on their masses(or types).

Two radiators are used in the **HERMES RICH** detector. A **silica aerogel** with refractive index **1.0304** and a $\mathbf{C_4F_{10}}$ gas which has the refractive index equal to **1.00137**. The combination of these two radiators allows to separate between pions, kaons and protons as it is shown in Figure 2.5.

2.2.5 The PID Algorithm

Using the signal information from the **particle identification detectors** the **PID** algorithm used to manipulate with tracks to make the identity for them. The **HERMES PID** algorithm based on the **Bayes theorem** which can be read as :

$$\mathbf{P(x \mid y) = \frac{P(y \mid x)P(x)}{P(y)}} \tag{2.3}$$

where $\mathbf{P(x \mid y)}$ is the probability for $\mathbf{x}$ to be an $\mathbf{y}$ and $\mathbf{P(x)(P(y))}$ is the overall probability for $\mathbf{x(y)}$. Thus the **PID** value can be defined as :

$$\mathbf{PID} = \mathbf{P(T_{l(h)} \mid R, k)} \tag{2.4}$$

where $\mathbf{P(T_{l(h)} \mid R, k)}$ is the probability that the track with parameter $\mathbf{k(p, \theta)}$(the $\mathbf{k}$ parameter describes a track with momentum $\mathbf{p}$ and the polar angle $\boldsymbol{\theta}$) lepton(hadron) having a detector response $\mathbf{R}$. Using the **Bayes** theorem one can get :

$$\mathbf{P(T_{l(h)} \mid R, k)} = \frac{\mathbf{P(R \mid T_{l(h)}, p)P(T_{l(h)} \mid k)}}{\mathbf{P(R \mid k)}} \tag{2.5}$$

Here $\mathbf{P(R \mid k)}$ is the probability for a track with parameter $\mathbf{k}$ to have a response $\mathbf{R}$ in a detector. It can be presented as :

$$\mathbf{P(R \mid k) = P(R \mid T_{l,h}, k)P(T_{l,h}, k)} \tag{2.6}$$

which is summed over all lepton(hadron) tracks with parameter $\mathbf{k}$. In equation (2.6) the first component of this product is the overall probability named as the parent distributions which is detector dependent and the $\mathbf{P(T_{l,h}, k)}$ represents the flux of leptons(hadrons) which depends on track atributes : the parameter $\mathbf{k}$. Eventually the **PID** value for lepton-hadron separation can be defined in following way :

$$\mathbf{PID} = \mathbf{log_{10}} \frac{\mathbf{P(T_l \mid R, k)}}{\mathbf{P(T_h \mid R, k)}} \tag{2.7}$$

where the logarithm is used just for a technical reason to provide a **PID** sign difference between leptons and hadrons. Using the equations (2.5) and (2.6) this logarithmic ratio can be transformed as :

$$\mathbf{PID} = \mathbf{PID_{Detector}} - \mathbf{log_{10}(Flux)} \tag{2.8}$$

where $\mathbf{PID_{Detector}}$ is the ratio of detector dependent parent distributions and the **Flux** and can be written as :

$$\mathbf{Flux} \equiv \frac{\mathbf{P(T_l \mid k)}}{\mathbf{P(T_h \mid k)}} \tag{2.9}$$

In Figure 2.6 the **PID** distribution is presented which clearly shows the separation of hadrons

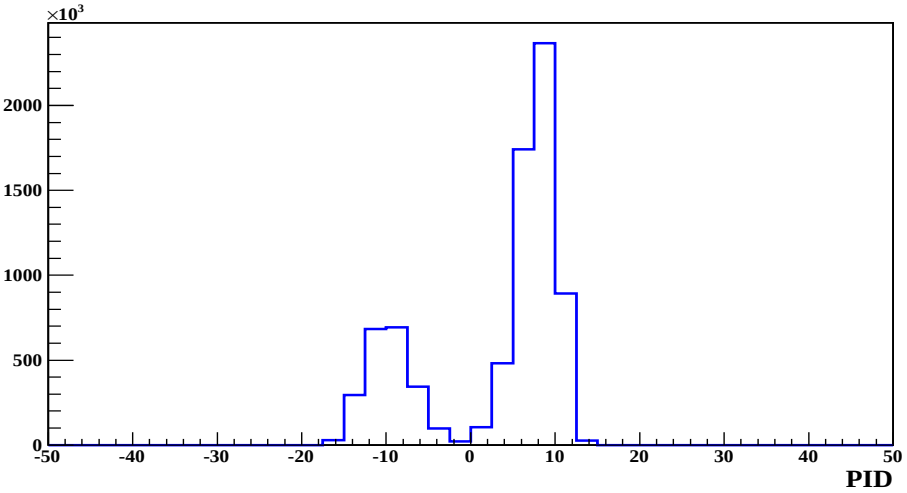

Figure 2.6: The **PID** distribution for **DIS** event sample from the **HERMES** data.

from leptons at **PID** value equal to zero. The **HERMES PID** provides a very efficient separation with less than one percent contamination of leptons with hadrons.

2.2.6 The HERMES Luminosity Measurement

The **HERMES** luminosity measurement is based on the measurement of the elastic **Möller** and **Bhabha** scattering for electron and positron respectively. When the beam is a positron, apart from **Bhabha** scattering also an anihillation takes place. The reaction products are detecting by two calorimeters installed at the left and right sides of the beam pipe.

The **Möller** and **Bhabha** scattering processes and the **electron-positron anihillation** is calculable within quantum electrodynamics(**QED**). To have the luminosity of the experiment the measured rate of the luminosity monitors(calorimeters) is divided on **QED** calculated cross sections of **Möller** and **Bhabha** processes[22].

2.3 Data Analysis

For this analysis we have used data from **DIS/SIDIS** processes on **D**, **Ne**, **Kr**, **Xe** targets using either **electron** or **positron** beams. The **HERMES** provides a large data set

for charged separated hadrons in **DIS** regime which allowed us to make a multidimensional view of the effect of our interest : **the nuclear attenuation effect**.

2.3.1 Data Selection

The **HERMES** data are organized using the concept of : **run**, **burst**, **event**, **track**. In the **run** level one can select the gas type and the operational mode(the target polarization mode). To ensure that we use a data within the normal experimental/instrumental conditions the **burst** level quality criteria are used which reject a data in case of the problems related to the experimental apparatus. Depending on the analysis the **event, track** cuts provide the reasonable selection of the effect of interest. The data in this analysis are selected in such a way :

run level: All runs coresponding to **D, Ne, Kr, Xe** which are analysable

burst level: All burst having reasonable data for **RICH**, **TRD** and the reasonable deadtime rejecting every first burst in a run

event level: All events which have the main **DIS** trigger fired and with low/high calorimeter threshold for polorized/unpolorized data

track level: All tracks accepted the fiducial volume of the **HERMES** spectrometer

Leptons: $\mathbf{Q^2 > 1GeV^2}$, $\mathbf{W^2 > 4GeV^2}$, $\mathbf{0.1 < \nu/E_{beam} < 0.85}$

Hadrons: $\mathbf{z > 0.2}$, $\mathbf{x_F > 0}$, $\mathbf{2\ GeV < p_h < 15\ GeV}$

The cut on $\mathbf{Q^2}$ select the deep-inelastic scattering regime. To suppress a contribution from resonance region into data the cut on $\mathbf{W^2}$ is applied. For high values of $\boldsymbol{\nu}/\mathbf{E_{beam}}$ the radiative corrections are very large and the restriction on $\boldsymbol{\nu}/\mathbf{E_{beam}}$ has applied to suppress such a correction.

Concerning to hadron selection criteria we are interested on hadrons produced in current fragmentation region. The cuts on $\mathbf{z}$ and $\mathbf{x_F}$ provide such a selection.

2.4 The RICH Unfolding

The hadron identification is one of the main topics of this analysis. It performs by **RICH** which uses the spherical mirrors to reflect the Čerenkov radiation into the photon detector which is an array of photomultiplier tubes placed above the mirror(Figure 2.7). Knowing the track momentum from the tracking system and measuring it's velocity using the opening angle of the Čherenkov photons one can reconstruct a particle type by reconstructing it's mass. The

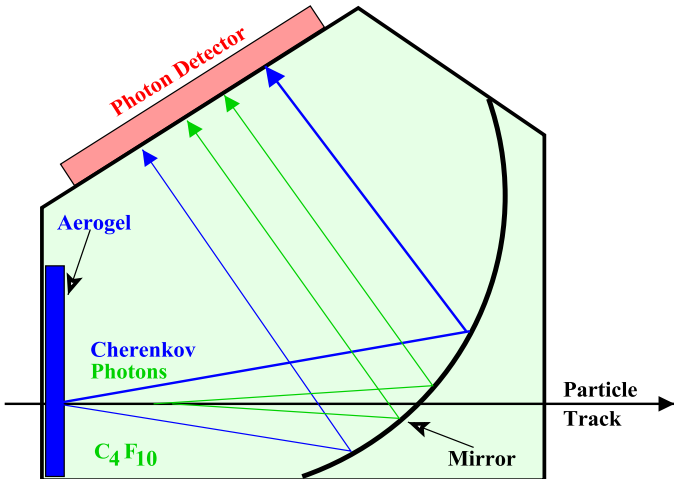

Figure 2.7: Particle identification by the **RICH** detector.

problems begin when the two tracks are very close to each other. In this case the overlaping of the photon rings can be the cause for the track misidentification. This issue is dominated in case of the electron track combined with any of the hadron track especially with the proton track. Assume the electron track satisfy the threshold conditions for the Čherenkov radiation in both radiators and the proton track which is very close to it, does not(Figure 2.8 b). Using the information from the tracking system the proton track can be misidentified as a kaon using the fake identity of lepton ring with kaon one. The another possiblity is low momentum particles mainly the protons bended at the edges of the detector and that is why misidentifyded, using lepton rings pattern, into kaons(Figure 2.8 a). In order to avoid from such an effect there is a necessity to tune the **RICH** parameters such as the yields of Čherenkov photons and the distribution of the Čherenkov angles. There are two ways to do this, first use the experimental data sample to reconstruct the decaying particles with known invariant masses and the second method is the usage of the Monte Carlo simulation. The first way has problems concerning

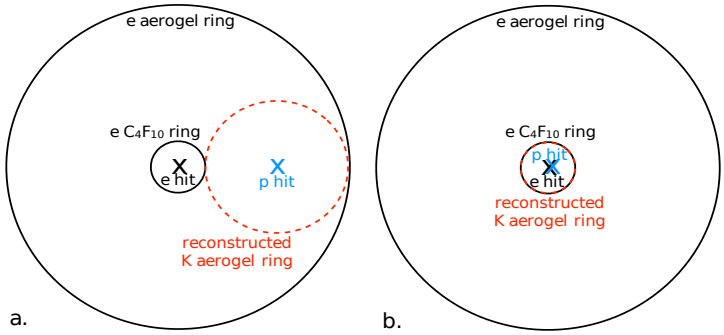

Figure 2.8: Particle misidentification in the **RICH** detector.

to statistics which is very important in studies of topologies for different kinematical regiems. Hence the **RICH** Monte Carlo simualtion is used to construct the so-called **P martrices** which are the statistical weights for given track to be a pion, kaon or a proton. The goal of the **RICH** unfolding to reweight the identity of tracks using these weigths. Since the effective performance of **RICH** detector depends on track momentum and the event topology(how many tracks there are in detector half). Having this information from data sample one can unfold the identified hadrons to get the true ones using the equation (2.10) :

$$\begin{pmatrix} I_\pi \\ I_K \\ I_p \\ I_X \end{pmatrix} = \begin{pmatrix} P_\pi^\pi & P_\pi^K & P_\pi^p & P_\pi^X \\ P_K^\pi & P_K^K & P_K^p & P_K^X \\ P_p^\pi & P_p^K & P_p^p & P_p^X \end{pmatrix} \begin{pmatrix} T_\pi \\ T_K \\ T_p \\ T_X \end{pmatrix} \tag{2.10}$$

In this equation $\mathbf{I_i}$ represents the identified/nonidentified hadrons($\boldsymbol{\pi}$, **K**, **p** and **X** is nonidentified hadron tracks) and $\mathbf{T_i}$'s are the true hadron type after the unfolding. The values for $\mathbf{P_i^j}$ are the probability that the true type hadron **i** will be identify as a type **j**. To get the final true hadron type distributions one should solve this matrix equation just inverting the **P** matrix. To do this we should truncated the **P** matrix(make it the square matrix eliminating the column for non identified probabilities) assuming that the contamination of nonidentified tracks is very small which is the case for the **HERMES RICH** detector.

$$\vec{\mathbf{T}} = \mathbf{P}^{-1}\vec{\mathbf{I}} \tag{2.11}$$

A momentum dependence of non-unfolded(raw) and **RICH** unfolded hadron yields is shown in Figure 2.9. We can see the clear indication of the **RICH** radiator transition between **8 - 11 GeV** region. The large discrepancies between raw and unfolded data at low momentum region caused by the **RICH** identification problems for those tracks due to the large bending which leads the tracks to hit the edges of the detector where the registration efficiencies are relatively small.

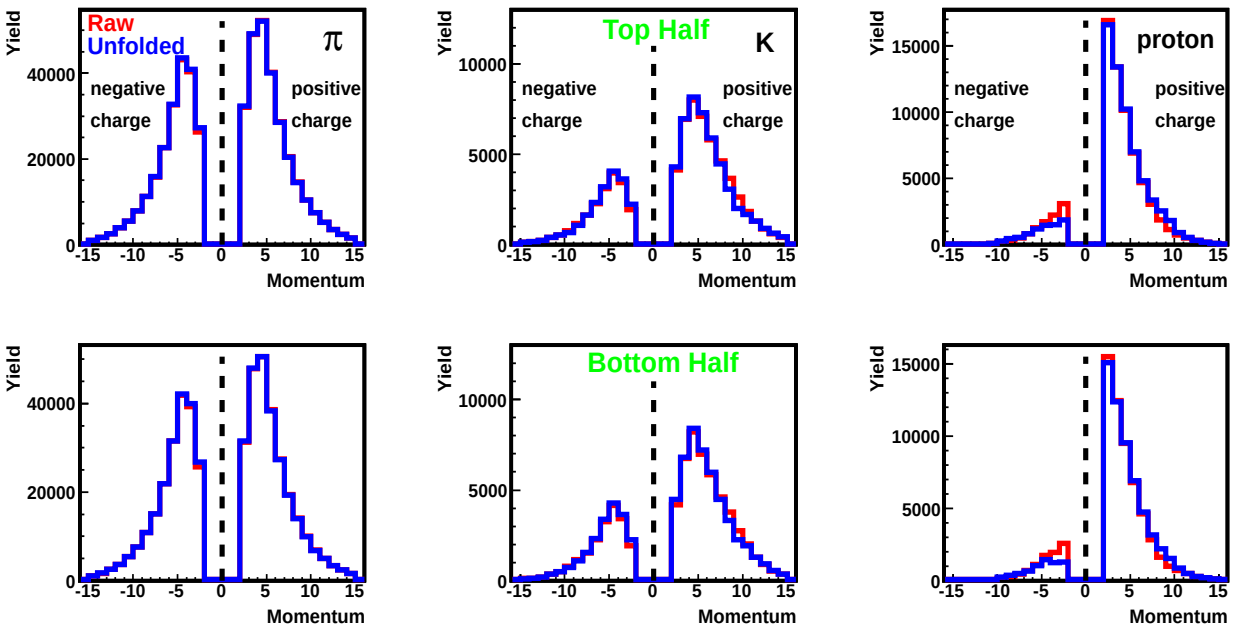

Figure 2.9: The influence of **RICH** unfolding on charged hadron yields. In red a raw data is shown without correction for **RICH** on misidentification effects. Blue points are already corrected for **RICH** misidentification effects. The comparison is done for both detector halves separately. There is a clear indication of the **RICH** radiator transition between **8 - 11 GeV** momentum range.

2.5 Charged Hadron Yields

The study of hadron yields plays an important role in hadron physics. It's because one can use the hadron yields to make the hadron multiplicity (i.e. the hadron yields normalized on **DIS** leptons) which carries an important information about the fragmentaion process. This quantity(2.12) depends on several kinematical variables such as the virtual photon energy $\boldsymbol{\nu}$, the hadron fractional energy **z**, the momentum component of hadron transverse to the virtual

photon direction $\mathbf{p_t}$ which are studed in this analysis. It depends also on the photon virtuality $\mathbf{Q^2}$ and the azimuthal angle $\boldsymbol{\varphi}$ which is an angle between lepton scattering and the hadron production planes. The last two dependencies are almost vanished in "super ratio" which is used to study the nuclear attenuation effect. Hence the main concentration was done on $\boldsymbol{\nu}, \mathbf{z}$ and $\mathbf{p_t}$ distributions.

$$\mathbf{M} = \frac{\mathbf{N^h}(\boldsymbol{\nu}, \mathbf{Q^2}, \mathbf{z}, \mathbf{p_t}, \boldsymbol{\varphi})}{\mathbf{N^e}(\boldsymbol{\nu}, \mathbf{Q^2})} \tag{2.12}$$

The $\mathbf{z}$ disribution of charged hadron yields is shown in Figure 2.10. Similarily to momentum distribution the identification problems reveals at very low $\mathbf{z}$ range, a part of which is cut-off using the data selection criterium to select the current fragmentation region : $\mathbf{z > 0.2}$. Apart

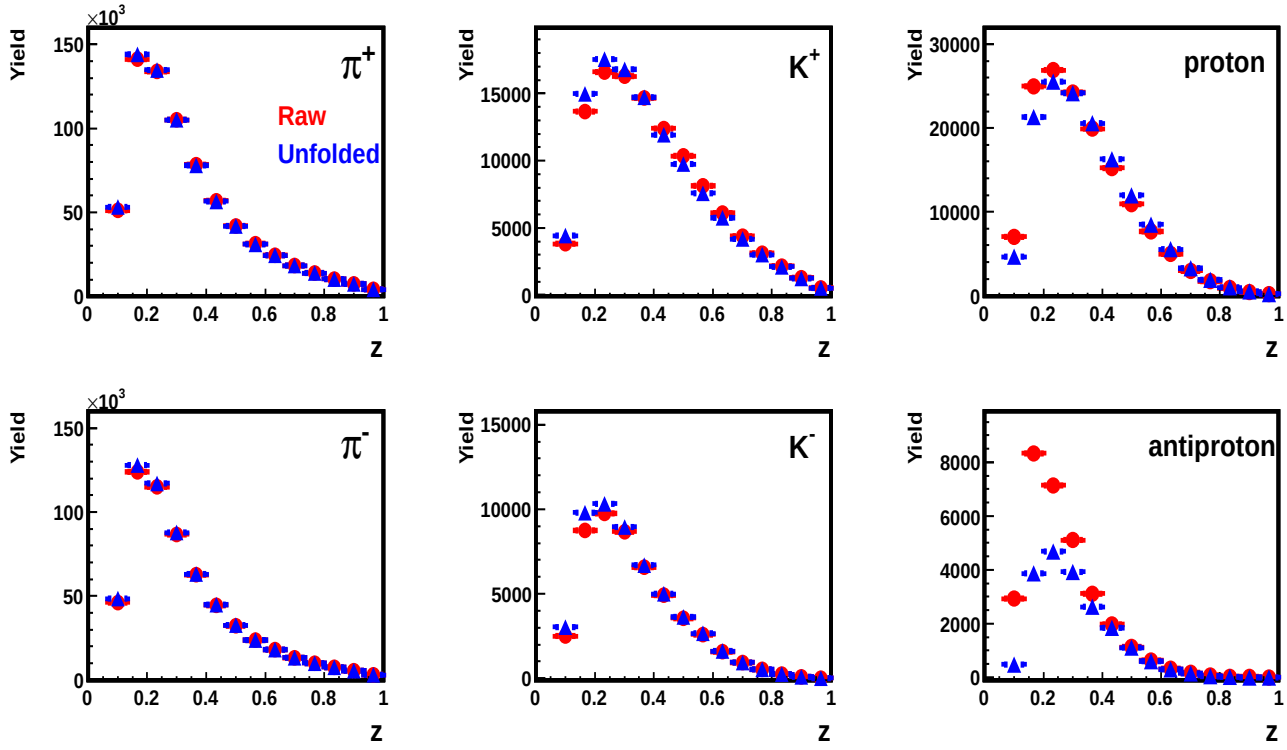

Figure 2.10: The $\mathbf{z}$ dependence of charged hadron multiplicities. The misidentification effect is larger at small $\mathbf{z}$ values, particularly for protons and antiprotons.

from cut on the $\mathbf{z}$ the $\mathbf{x_F > 0}$ cut is used to select hadrons from current fragmentation region. The corresponding hadron yields with cut on $\mathbf{x_F}$ are presented in Figure 2.11. Here one can see the huge flux change for protons and antiprotons at small $\mathbf{z}$ values while for kaons it is relatively small and there is practically no changes for pions. The impact of hadronic cuts on charged hadron yields is shown in Figure 2.12. One can see that the cut on $\mathbf{z}$ is already satisfied

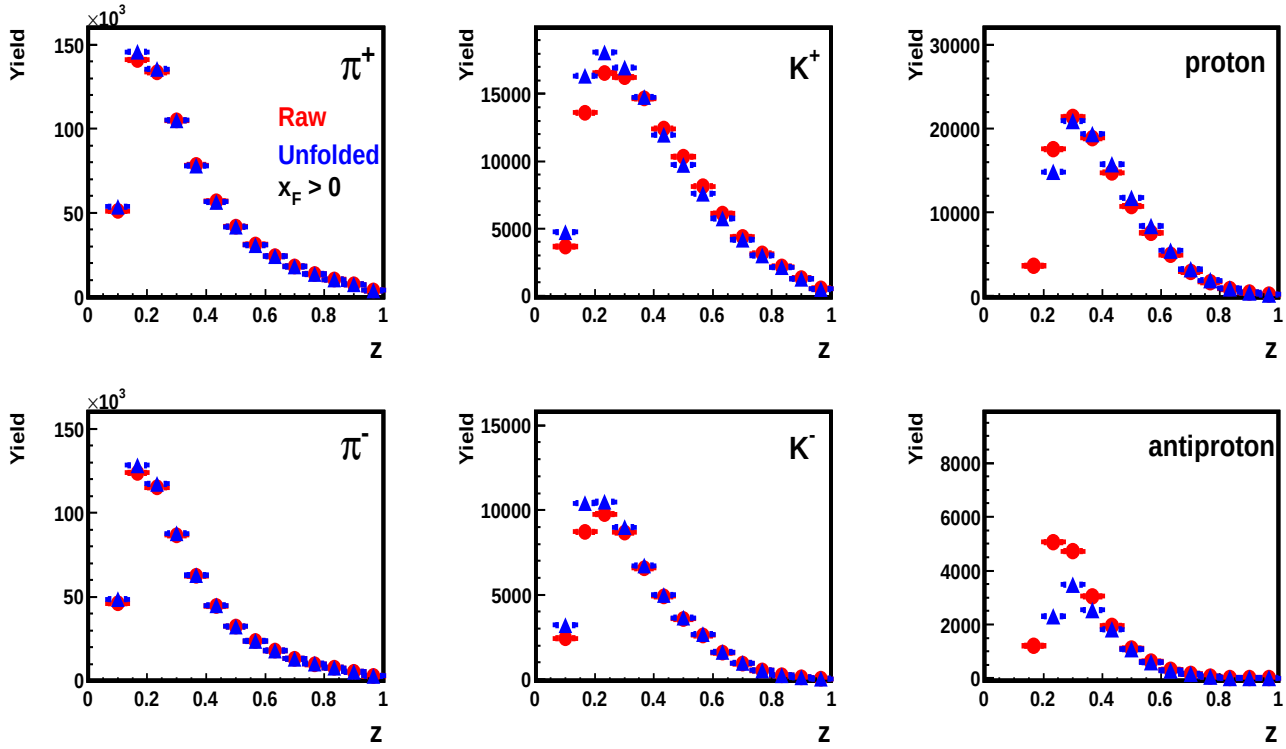

Figure 2.11: The **z** dependence of charged hadron multiplicities with cut on $\mathbf{x_F}$. The Feynman variable cuts more protons and antiprotons coming from the target fragmentation region.

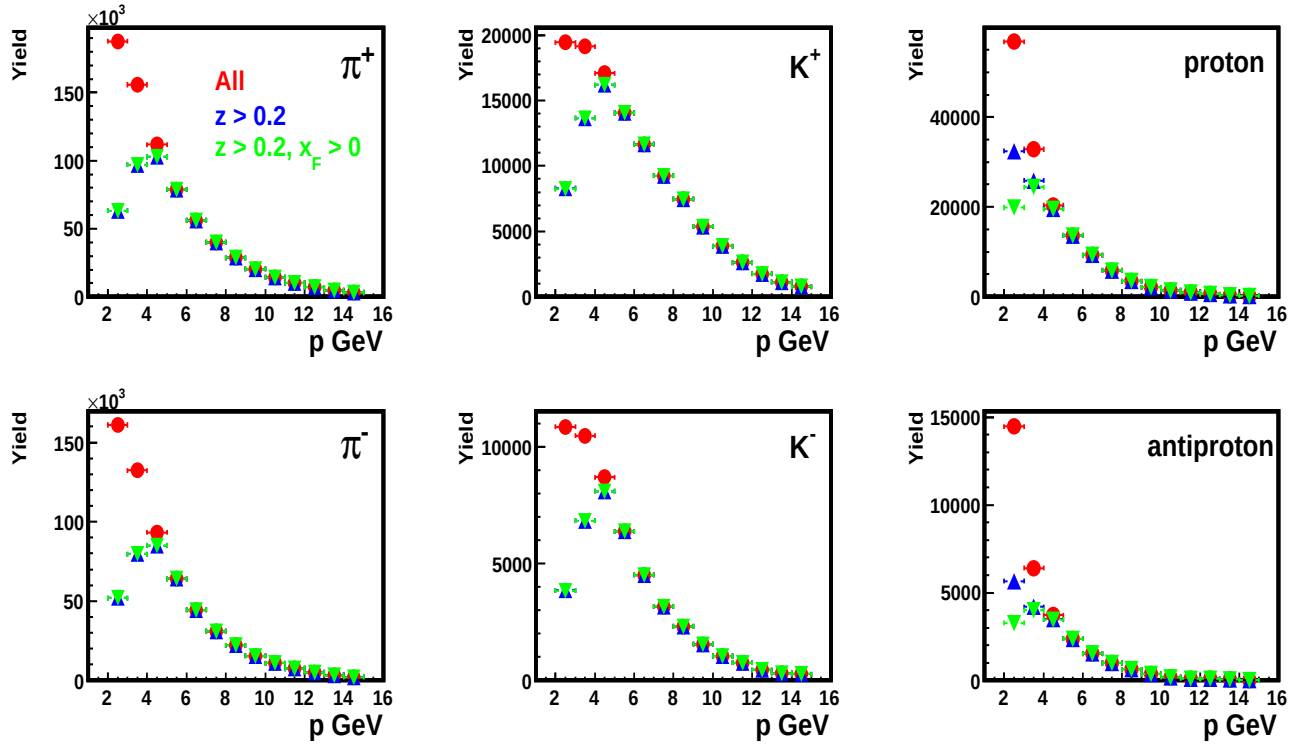

Figure 2.12: The impact of hadronic cuts on raw hadron momentum dependent yields.

to $\mathbf{x_F > 0}$ condition for pions and also for kaons while for protons and antiprotons there is a large contribution from target fragmentation region at small momentum range.

The $\boldsymbol{\nu}$ dependence of charged hadron multiplicities is shown in Figure 2.15. We can see that the main hadron statistics is populated in the $\boldsymbol{\nu}$ range **10 - 12 GeV**. The usage of standard **DIS** cuts $\mathbf{Q^2 > 1GeV^2}, \mathbf{W^2 > 4GeV^2}$ restrict the lower limit of $\boldsymbol{\nu}$ to be greater than $\sim$ **2.2 GeV**. The upper limit for $\boldsymbol{\nu}$ is given with a cut on $\mathbf{y = \frac{\nu}{E_{beam}} < 0.85}$ which leads to the restriction $\boldsymbol{\nu} <$ **23.5 GeV**. It is also seen that the huge amount of negatively charged kaons are misidentified as antiprotons.

In Figure 2.16 the transverse momentum dependence of charged hadrons multpliciteis is shown. The **HERMES** allowes to reach the transverse momentum range up to **1.5 - 1.7 GeV**. Beyond to the collinear case the $\mathbf{p_t}$ studies of the hadron multiplicities play an important role for nucleon three dimensional structue investigations. The point here to study, how the intrisic transverse momentum of parton generates the final hadron transverse momentum component which provide a much deeper understanding of **QCD** and hadron structure. In contrast to the collinear factorization, here the integration over the parton transverse momentum is left which leads to the more general transverse momentum dependent(**TMD**) factorization.

As it was already mentioned, using the hadron multiplicities one can access to the fragmentation functions which are assumed to be independent of $\mathbf{x_{Bj}}$ but only depend on $\mathbf{z}$. On the other hand these transverse momentum dependent fragmentation functions are not yet fully understood. This is a relatively new task to study and this subject called the transversity. There are several approaches to describe the transverse momentum dependent fragmentation functions[23][24]. The commonly known method is the Gaussian parametrization or the so-called Gaussian anzats[25]. The fragmentation functions in this approach have a form[26] :

$$\mathbf{D_{H/f}(z, K_T) = d_{H/f} \cdot \frac{exp[-K_T^2 / < K_T^2 >]}{\pi < K_T^2 >}} \tag{2.13}$$

where $\mathbf{K_T}$ is the hadron transverse momentum in the photon rest frame. Therefore the $\mathbf{p_t}$ distribution for charged hadron multiplicities is very importanat to test different hypothesis existing at the moment.

In Figure 2.17 one can see the correlation between different kinematical variables for

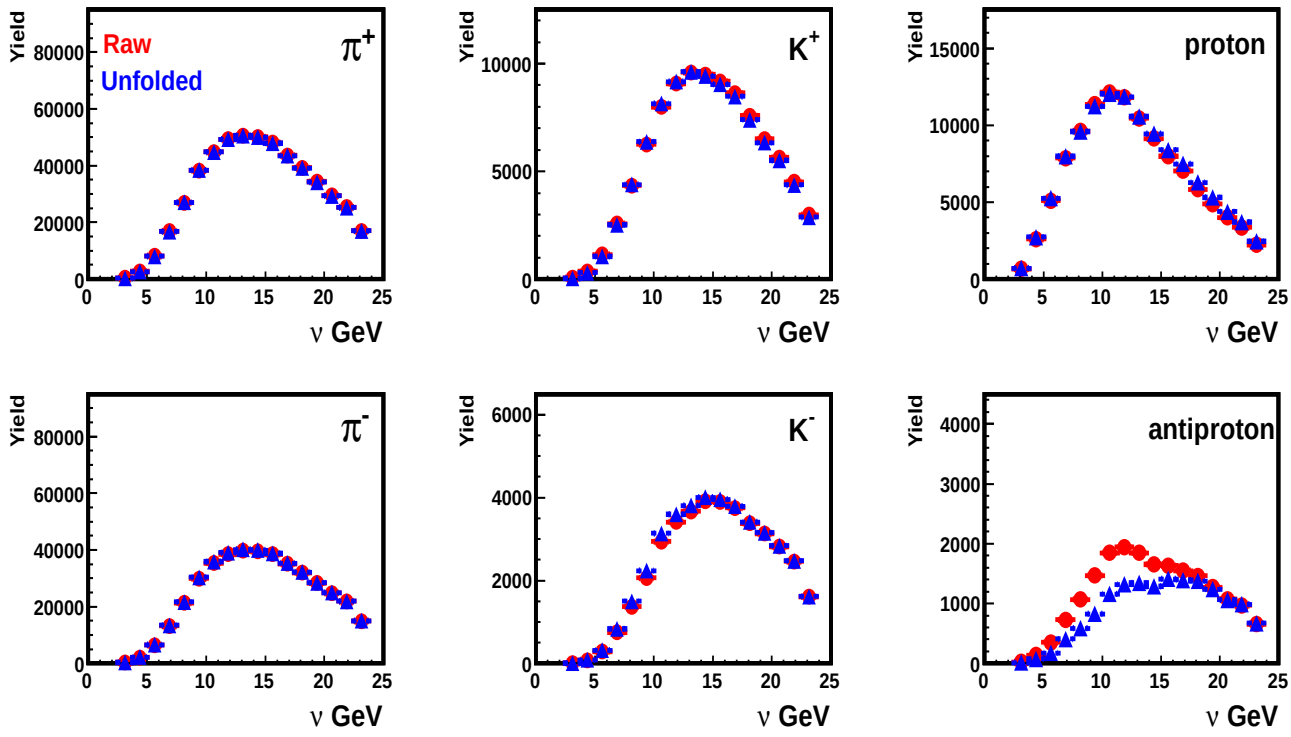

Figure 2.13: The ν dependence of charged hadron multiplicities. The **RICH** misidentification effect is spread over whole range of ν.

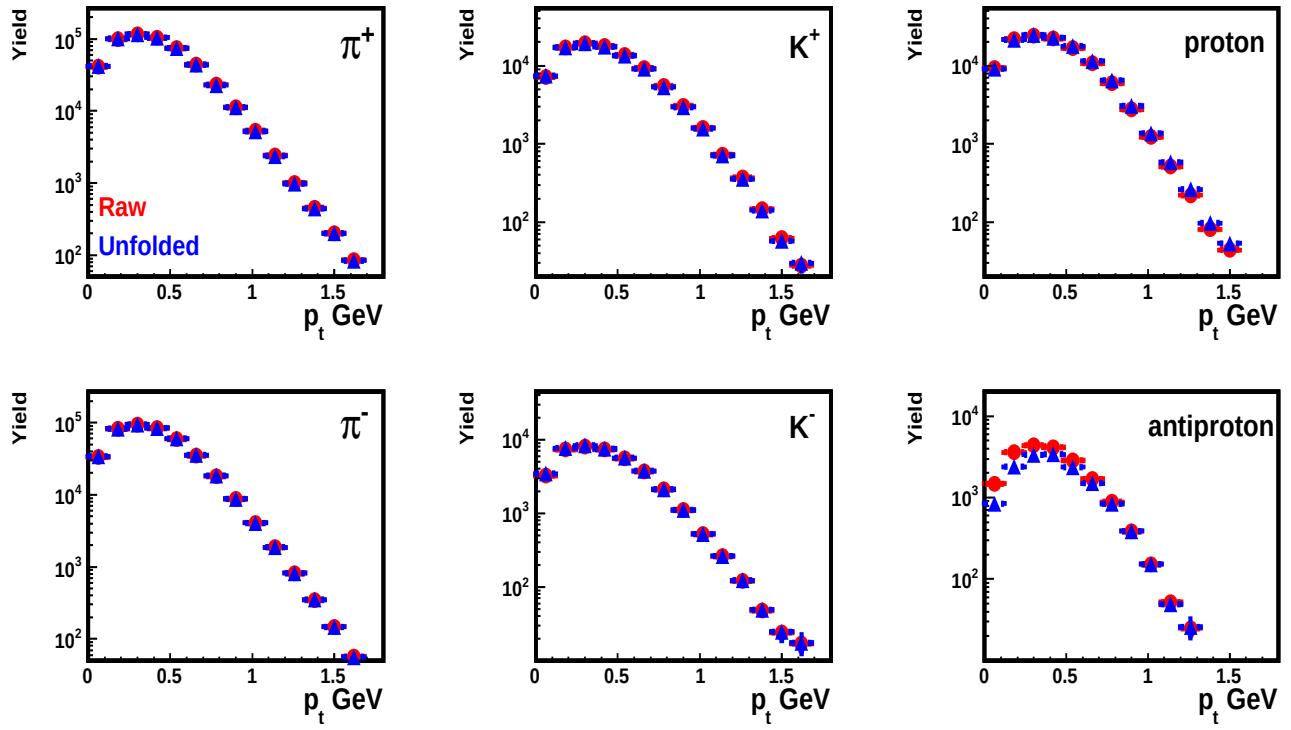

Figure 2.14: The $\mathbf{p_t}$ dependence of charged hadron multiplicities. The **RICH** misidentification effect is dominated at small $\mathbf{p_t}$ range.

charge separated pions,kaons and protons: $\mathbf{p_t^2}$ **vs.** $\boldsymbol{\nu}$ **vs.** $\boldsymbol{z}$.

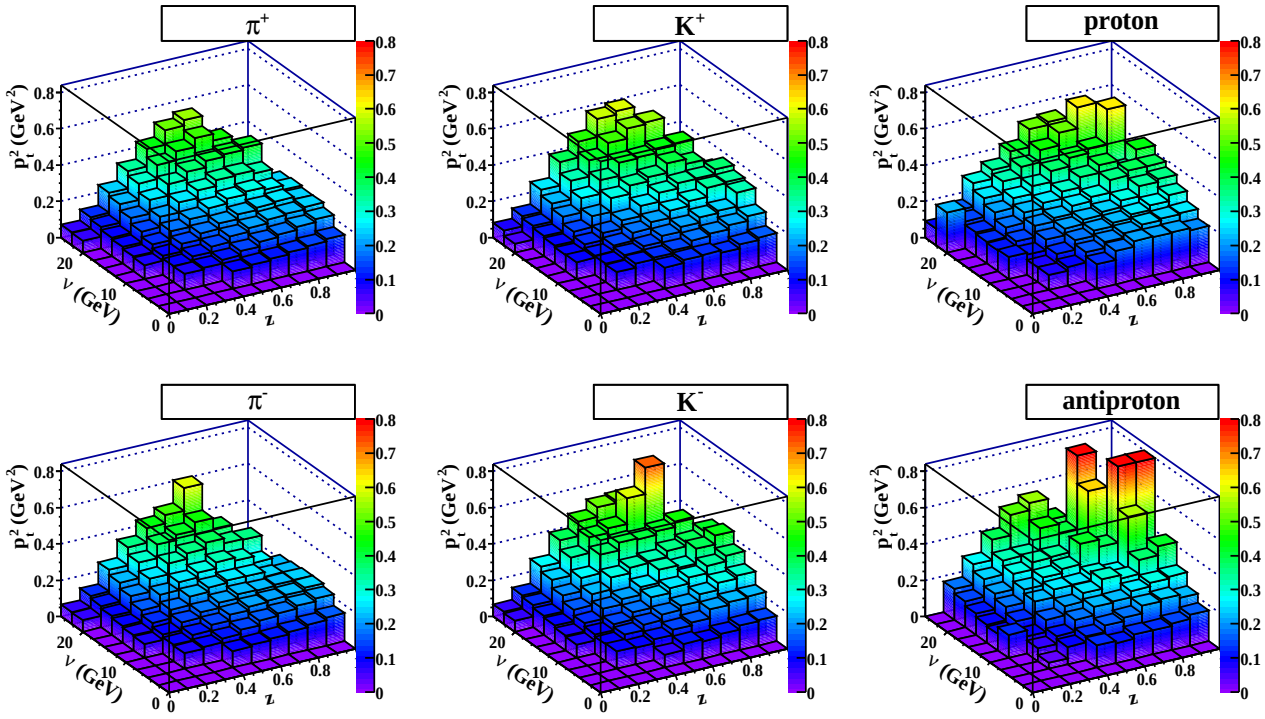

Figure 2.15: The correlation between $\mathbf{p_t^2}$, $\boldsymbol{\nu}$ and $\boldsymbol{z}$ for charged separated hadrons.

2.5.1 Charge Symmetric Background

Apart from the **RICH** misidentification the hadron yields are also affected by the so-called charge symmetric background contribution which can be taken into account in the following way. If the deep-inelastic scattered lepton has a charge which is opposite to the beam lepton charge than one can easily exclude them applying the charge identity criteria on the scattered lepton to be the same with the beam lepton. But due to the charge symmetric kind of the process such as the Dalitz decay of photon into electron-positron pair, there is also contribution of the same charged **DIS** leptons coming from such a secondary processes. To account them one should fix the scattered lepton charge to be the same as the beam charge is then subtract the leptons satisfying the standard **DIS** criteria but with the opposite charge than the beam lepton charge is.

Figure 2.16 showes the influence of charge symmetric background on the identified hadron yields. As it was expected the effect is dominant at small **z** range since the secondary leptons

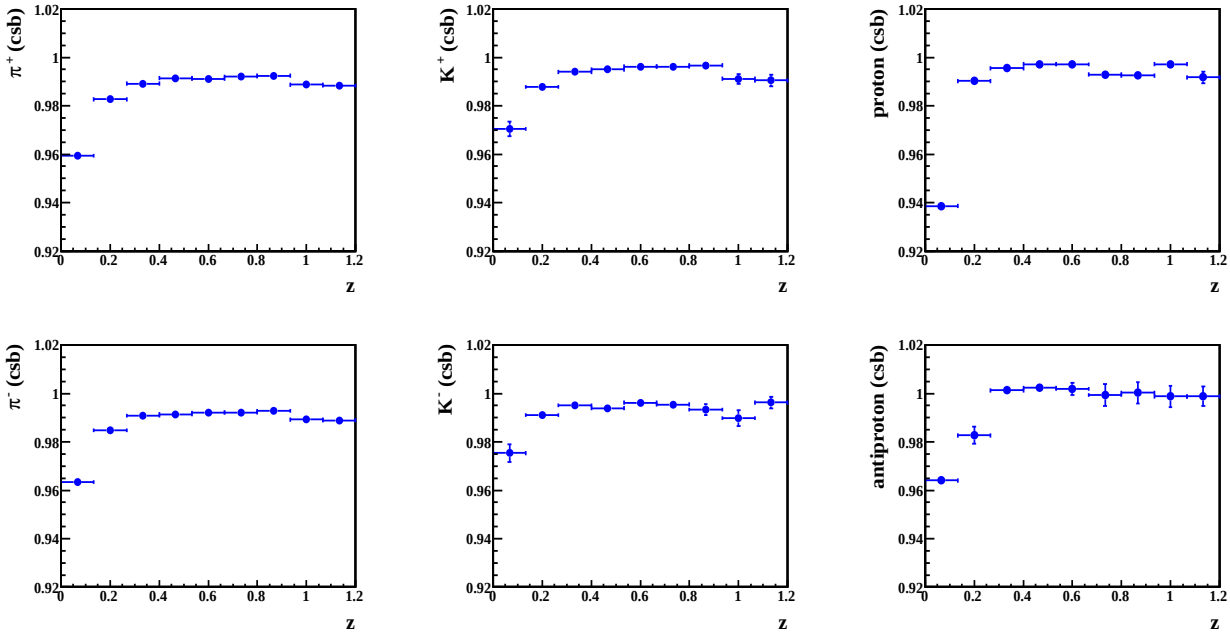

Figure 2.16: Charged symmetric background effect on charged hadron yields. The effect is essential at small **z** values. It is less than **2**% for the data of interest : $\mathbf{z > 0.2}$.

produced by the Dalitz decay supposed to have a low momenta. The maximum effect in the range of interest ($\mathbf{z > 0.2}$) is estimated less than **2%**.

2.6 The HERMES Monte Carlo Package

The aim of the **HERMES Monte Carlo** is to generate a **DIS** process and propagate a physical event through the simulated spectrometer. This is an important tool to understand the experimental data and to estimate the various effects coming from detector resolutions and the spectrometer acceptance. To do this a physical event is generated in kinematical bins of $\boldsymbol{\nu}$ and $\boldsymbol{Q^2}$ according to the corresponding cross section $\frac{\mathbf{d^2\sigma}}{\mathbf{d\nu Q^2}}$. The scattering process required the knowledge of the parton distribution functions (**PDFs**). There are several parametrizations based on the experimental data : **GRV**[27], **MRS**[28]. The commonly used one is provided by **CTEQ6**[29] collaboration. The next step is to introduce a hadronization which can be done only by phenomenological approach. The **HERMES Monte Carlo** uses the **JETSET** package which based on the **LUND**[8] model.

The **HERMES Monte Carlo** is a chain of different programs which together make

a simualtion and accumalate results in the form the experimental data have. It starts with **Generator Monte Carlo (GMC)** which is a physical generator like **DISNG, PHYTIA**[31] and generates a phyisical event.

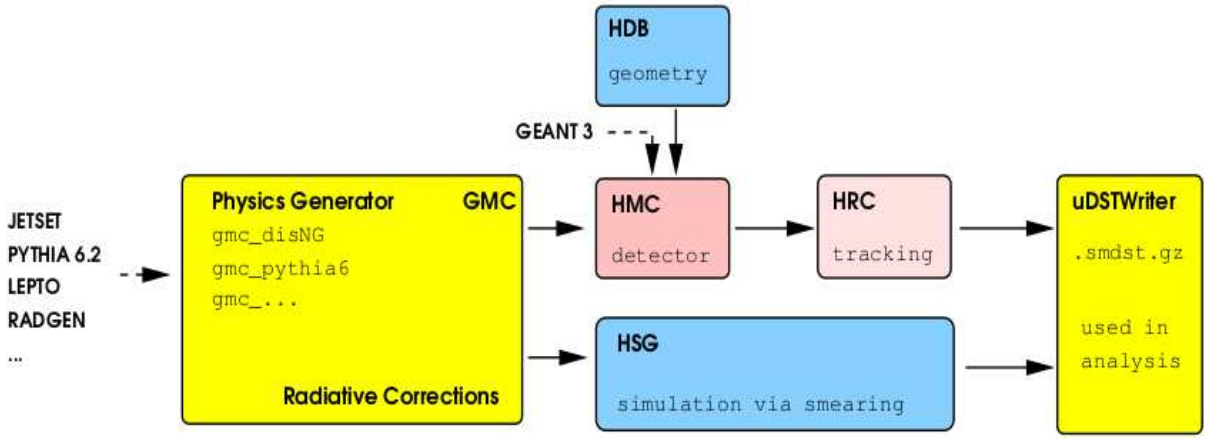

Figure 2.17: The **HERMES Monte Carlo** chain.

Then the generated particles are propogated through the **HERMES** detector setup(the spectrometer) and depending on the kinematics they have an interaction with detectors which is simulated by the **GEANT**[30] simulation package. On the other hand due to the **HERMES** acceptance effect (both geometrical and kinematical) not all generated particles can be registrated. All these effects are taken into account by the **HERMES Monte Carlo program (HMC)** which uses **GEANT** programing package to simulate the **HERMES** spectrometer and the target system. For each generated track which travers through the spectrometer the **GEANT** calculates the detector responses and at the end of the **HMC** package we know all detectors response and the particle track type as well from the generator level. Then the **HERMES Reconstruction Code** is used to transform detector responses into the particle tracks. This procedure is the same in both data and **Monte Carlo** schemes thus all possible biases introduced at this stage will be the same.

Finally the simulated data are accumulated in the same way as the experimental data, except the additional information the **Monte Carlo** has. For instance the **Monte Carlo** has an information about the particle true type and generated kinematics as well.

2.6.1 Event Generators

The **HERMES** generator **Monte Carlo** program(**GMC**) uses two steps for the event generation. In the first step a physics generator simulates the interaction of the initial state particles. Then in the next step the hadronisation take place evolving the initial system into the final state using **JETSET** program, based on the **LUND** string fragmentation model.

In **GMC** level the commonly used package is the **DISNG** package which generats a deep-inelastic scattering process. It uses two generators for poloraized and unpolorized cases : the **PEPSI**[32] and the **LEPTO**[33] respectively. Despite **LEPTO** and **PEPSI** are an excellent tool to study the **DIS** process, the number of physics processes which they consider is limited. In particular, they do not account for the exclusive production of vector mesons due to the complication of the particle production process at $\mathbf{z \to 1}$ in the **LUND** model. For this cases one can use the **PYTHIA** event generator which can generate a large variaty of the physical processes.

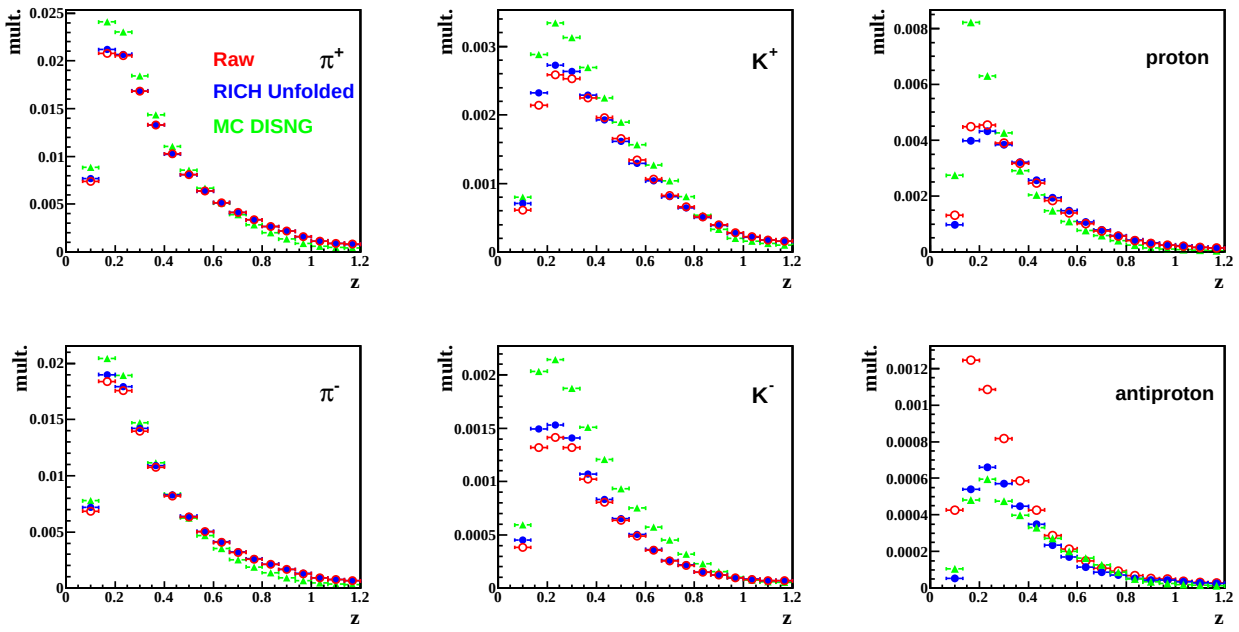

Figure 2.18: Data Monte Carlo comparision for charged hadron multiplicities. In green the multiplicity data from DISNG Monte Carlo is shown in comparison with experimental data with(blue) and without(red) correction for the **RICH** misidentification effect.

2.6.2 Unfolding for Radiative Effects and Detector Smearing

Due to the fact that the detectors have a certain resolution and the beam lepton can radiate a real photon(initial state radiation **ISR**) or the same can happen with the scattered lepton(final state radiation **FSR**) the true kinematics can be changed(see Fig. 2.19). In order to correct for such effects the **DISNG** Monte Carlo is used. The idea is to compare the re-

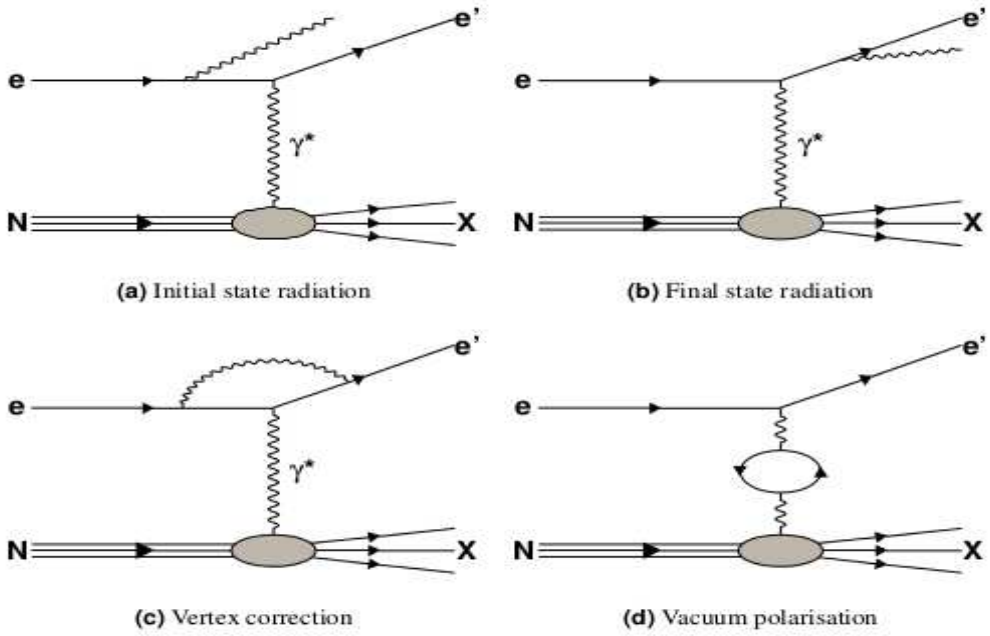

Figure 2.19: True kinematic change due to the radiative effects.

constructed kinematics which includes these effects with a generated ones making a correction matricies named as the smearing matricies. For this purpose, bin-by-bin migration of events due to the kinematic change is calculated in terms of migration matrix elements and the experimental data ara corrected using these elements. Technically it can be calculated in such a way[34]. We use two Monte Carlo samples. The first one includes the experimental setup and possible radiative effects. Here we have fully tracked Monte Carlo production which should be used for calculation of elements of the migrartion matricies. The idea is to fix kinematical bin in experimental level and look to which Born bin i.e. the bin with corresponding true kinematics it corresponds to. If one make a numeration than one should consider two indices **i** for experimental Monte Carlo sample and **j** for Born or generator level sample. In this way one get a matix, each element of which has an information about real event migration due to the true

kinematic change caused by either detector smearing or radiative effects. If the number of bins in experimental Monte Carlo sample is $\mathbf{N_{MC_{EXP}}}$ and the number of bins in Born level is $\mathbf{N_{Born}}$ than the migration matrix should have a size is $(\mathbf{N_{MC_{EXP}}})\mathbf{x}(\mathbf{N_{Born}+1})$. The additional bin in Born level contains events passing through the experimental Monte Carlo bin from outside of the standard **DIS** cuts applied for true kinematics. On the other hand using the Born $\mathbf{4\pi}$ Monte Carlo which has no radiative effects **ON** one can get a Born vector which is used for normalization of the migration matrix to get the correction coefficients which form the final smearing matrix. An important feature of this smearing matrix is a reduced model dependence, since in nominator and denominator the same Monte Carlo model is used.

$$\mathbf{S(i,j)} = \frac{\mathbf{n(i,j)}}{\mathbf{n^{Born}(j)}} \tag{2.14}$$

where an $\mathbf{n(i,j)}$ is the migration matrix and $\mathbf{n^{Born}(j)}$ is the Born vector. It is important to mention that a summation over Born bins gives :

$$\mathbf{n_{MC_{EXP}}(i)} = \sum_{\mathbf{j=0}}^{\mathbf{N_{Born}}} \mathbf{n(i,j)} \tag{2.15}$$

which is not true for Monte Carlo experimental bin summation :

$$\mathbf{n_{Born}(j)} \neq \sum_{\mathbf{i=1}}^{\mathbf{N_{MC_{EXP}}}} \mathbf{n(i,j)} \tag{2.16}$$

because the radiative effects might cause the migration of events outside of kinematic box generated initially. As a result a normalization is lost between Born and experimental level data samples. This is the reason for the usage of two Monte Carlo samples mentioned above. According to equation (2.14) and (2.15) one can write **:**

$$\mathbf{n_{MC_{EXP}}(i)} = \sum_{\mathbf{j=0}}^{\mathbf{N_{Born}}} \mathbf{S(i,j)n_{Born}(j)} \tag{2.17}$$

Coming to the real experimental sample one can write the experimental distribution following to the Monte Carlo simulation in such a way :

$$\mathbf{Exp(i)} = \mathbf{Lumi} \cdot \mathbf{Eff(i)} \cdot \sum_{\mathbf{j=0}}^{\mathbf{N_{Born}}} \mathbf{S(i,j)n_{Born}(j)} \tag{2.18}$$

where the **Lumi** is the overall luminosity of process and **Eff(i)** is a factor which includes the detector efficiencies. In case of multiplicity ratio this two factors are taking off and the final equation for smearing and radiative effects looks like :

$$\mathbf{Born(j)} = \frac{\mathbf{1}}{\boldsymbol{\sigma}_{\mathbf{Born}}} \cdot \sum_{\mathbf{i=1}}^{\mathbf{N_{MC_{EXP}}}} \mathbf{S_h^{-1}(j,i)} \Big(\mathbf{Exp(i)} \cdot \boldsymbol{\sigma}_{\mathbf{MC_{Trk}}} - \mathbf{Background(i,0)} \Big) \tag{2.19}$$

Here the $\mathbf{S_h^{-1}(j,i)}$ is a truncuated inversed smearing matrix, $\boldsymbol{\sigma}_{\mathbf{Born}}$ is the inclusive cross sections from Born Monte Carlo and $\boldsymbol{\sigma}_{\mathbf{MC_{Trk}}}$ is the inclusive cross sections from tracked Monte Carlo. It is important to mention that by **Born(j)** and **Exp(i)** one should assume the multiplicity ratio in $\mathbf{4}\pi$ and in acceptance respectively.

Due to the complications related to Monte Carlo simulations for heavy nuclear targets and taking into account the fact that we are interested in the nuclear attenuation effect which is multiplicity super ratio, we assume that these effects are mainly cancel out, that is why we don't use $\mathbf{4}\pi$ unfolding technik in this analysis.

Chapter 3

Results and Conclusions

The data from semi-inclusive deep-inelastic scattering process off different nuclear targets are analysed. The hadron **DIS** normalized yileds(the multiplicities) are extracted. They are corrected for the **RICH** detector possible misidentification effects. Using the hadron multiplicity ratios $\mathbf{R_A^h}$ the nuclear attenuation effect is studied in two dimensional[35] manner. For all data plots the scale uncertainties are estimated to be **3**%, **5**%, **4**%, and **10**% for **pions**, **kaons**, **protons** and **antiprotons**, respectively. The results of $\mathbf{R_A^h}$ are presented for **neon (Ne)**, **krypton (Kr)** and **xenon (Xe)** targets for charge separated **pions**, **kaons** and **protons** using a fine binning in one of the kinematical variables and three slices in a second variable. This allows to study the effect of interest in more detailes, suppressing the correlations between different kinematical variables. The large statistics and the accurate measurement provided by the **HERMES** spectrometer allowes us to have the first multidimensional data for the nuclear attenuation effect in a wide kinematic range.

3.1 ν dependence in three z slices

In Figure 3.1, the $\boldsymbol{\nu}$ dependence of $\mathbf{R_A^h}$ is shown in three **z** slices. The global feature for the multiplicity ratio is the decreasement with increasing of target atomic mass **A** which can be qualitatively understood in sense of the strengthening of energy loss proccesses due to the enhancment of the nuclear matter density.

With the increasing of $\boldsymbol{\nu}$ an enhancement of $\mathbf{R_A^h}$ was observed for pions($\boldsymbol{\pi^+}$, $\boldsymbol{\pi^-}$) and

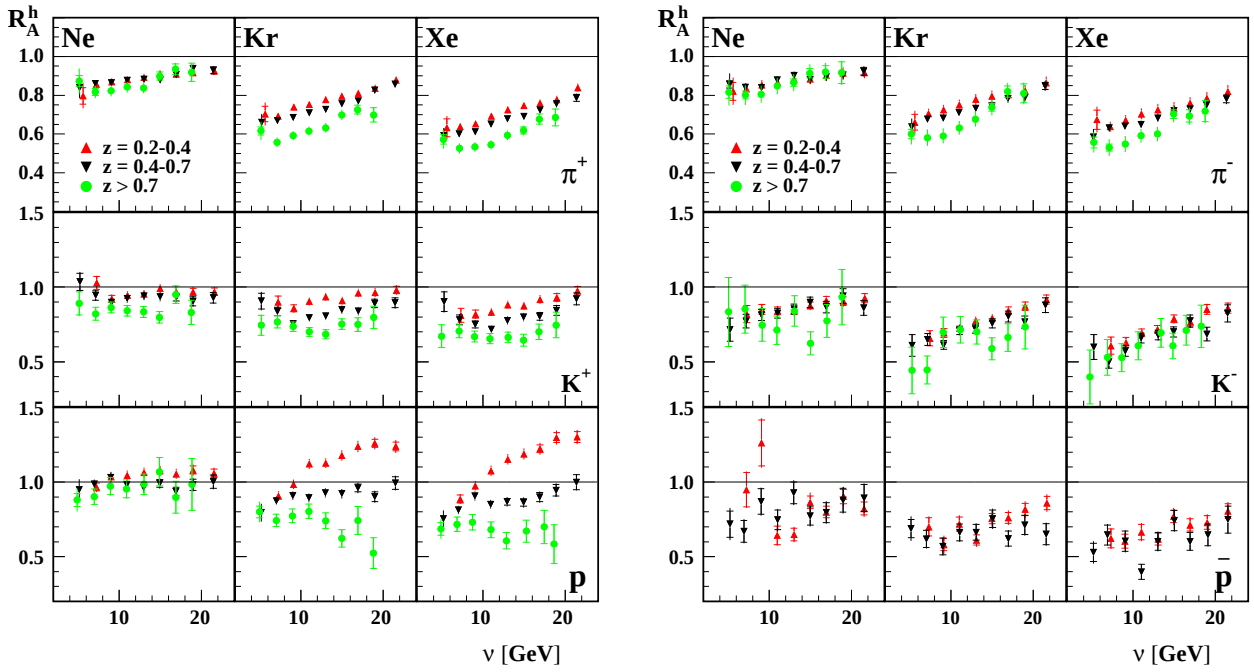

Figure 3.1: Dependence of $\mathbf{R_A^h}$ on $\boldsymbol{\nu}$ for three slices in $\mathbf{z}$. There is an enhancment of the nuclear attenuation effect with increasing of the nuclear target mass. For protons we see a different behaviour than for mesons and antiprotons.

negatively charged kaons($\mathbf{K^-}$) which is consistent with fragmentation models, explaining such a behaviour as a result of Lorentz dilation and/or a modification of the fragmentation function[36]. This kind of behaviour was observed in **EMC** collaboration[4] and later by the **HERMES** one dimensional data[5] but in contrast to the negatively charged kaons ($\mathbf{K^-}$), the $\boldsymbol{\nu}$ dependence of $\mathbf{R_A^h}$ for positively charged kaons($\mathbf{K^+}$) which is showing an enhancement at the lowest $\mathbf{z}$-slice, it seems flatter for the high $\mathbf{z}$ values.

For protons the behaviour of $\mathbf{R_A^h}$ is very different from those for the other hadrons. Particularly for the lowest $\mathbf{z}$ slice it exceeds the unity at large $\boldsymbol{\nu}$ values. This phenomena might be caused by the fact that protons apart from hadronization could be knocked out off the nucleus while other hadrons are the result of fragmentation only. This effect which caused by the final state interaction(**FSI**) will contribute into the low momentum proton spectra which was consistent with the experimental data showing a prominent enhancement at small $\mathbf{z}$ bin which mostly realted with low momentum protons. It is also stronger for heavy nuclei which is consistent with the assumption of large contribution from knock-out processes in this case.

Despite a lack of statistics, antiprotons, unlike protons, show a similar behaviour as mesons reflecting the fact that the antiprotons are the result of the fragmentation only.

Below the experimental data extracted for the $\boldsymbol{\nu}$ dependencies in three slices of $\mathbf{z}$ is tabulated in tables. Here the bin center values are shown the first column, the second column corresponds to the values of $\mathbf{R_A^h}$ and the third and fourth columns represent a statistical and total errors respectively.

$\boldsymbol{\nu}$ bin (GeV)	$\mathbf{R_{Ne}^{\pi^+}}$	statistical error(+/-)	total error(+/-)
5.6148	**0.7965**	**0.0425**	**0.0692**
7.2469	**0.8566**	**0.0134**	**0.0328**
9.1151	**0.8700**	**0.0085**	**0.0325**
11.0212	**0.8801**	**0.0071**	**0.0325**
13.0370	**0.8911**	**0.0069**	**0.0328**
14.9963	**0.9088**	**0.0071**	**0.0337**
16.9669	**0.9087**	**0.0076**	**0.0338**
18.9974	**0.9164**	**0.0089**	**0.0344**
21.5743	**0.9256**	**0.0093**	**0.0348**

Table 3.1: $\boldsymbol{\nu}$ dependence of multiplicity ratio $\mathbf{R_{Ne}^{\pi^+}}$ from **Ne** target for positively charged pions in $\mathbf{0.2 < z < 0.4}$ slice.

$\boldsymbol{\nu}$ bin (GeV)	$\mathbf{R_{Ne}^{\pi^+}}$	statistical error(+/-)	total error(+/-)
5.2214	**0.8384**	**0.0171**	**0.0593**
7.1137	**0.8601**	**0.0117**	**0.0307**
9.0647	**0.8634**	**0.0099**	**0.0302**
11.0016	**0.8763**	**0.0093**	**0.0304**
13.0159	**0.8824**	**0.0094**	**0.0306**
14.9746	**0.8778**	**0.0102**	**0.0307**
16.9376	**0.9058**	**0.0120**	**0.0322**
18.9744	**0.9373**	**0.0153**	**0.0345**
21.4661	**0.9285**	**0.0176**	**0.0353**

Table 3.2: $\boldsymbol{\nu}$ dependence of multiplicity ratio $\mathbf{R_{Ne}^{\pi^+}}$ from **Ne** target for positively charged pions in $\mathbf{0.4 < z < 0.7}$ slice.

$\boldsymbol{\nu}$ bin (GeV)	$\mathbf{R_{Ne}^{\pi^+}}$	statistical error(+/-)	total error(+/-)
5.1718	**0.8734**	**0.0281**	**0.0705**
7.1227	**0.8170**	**0.0179**	**0.0406**
9.0471	**0.8218**	**0.0148**	**0.0380**
10.9860	**0.8417**	**0.0149**	**0.0373**
12.9944	**0.8374**	**0.0161**	**0.0376**
14.9407	**0.8991**	**0.0201**	**0.0401**
16.8528	**0.9336**	**0.0283**	**0.0438**
18.8312	**0.9176**	**0.0471**	**0.0566**

Table 3.3: $\boldsymbol{\nu}$ dependence of multiplicity ratio $\mathbf{R_{Ne}^{\pi^+}}$ from **Ne** target for positively charged pions in $\mathbf{z > 0.7}$ slice.

ν bin (GeV)	$R_{Ne}^{\pi^-}$	statistical error(+/-)	total error(+/-)
5.6202	0.8204	0.0463	0.0749
7.2592	0.8335	0.0145	0.0373
9.1278	0.8525	0.0093	0.0369
11.0233	0.8655	0.0078	0.0374
13.0338	0.8845	0.0076	0.0381
14.9993	0.8841	0.0077	0.0387
16.9658	0.9018	0.0084	0.0396
18.9960	0.9139	0.0097	0.0403
21.5809	0.9168	0.0099	0.0405

Table 3.4: ν dependence of multiplicity ratio $R_{Ne}^{\pi^-}$ from **Ne** target for negatively charged pions in $0.2 < z < 0.4$ slice.

ν bin (GeV)	$R_{Ne}^{\pi^-}$	statistical error(+/-)	total error(+/-)
5.1918	0.8554	0.0193	0.0622
7.1114	0.8411	0.0129	0.0328
9.0609	0.8387	0.0110	0.0320
11.0007	0.8778	0.0107	0.0332
13.0232	0.9015	0.0111	0.0341
14.9817	0.8797	0.0118	0.0336
16.9425	0.8949	0.0136	0.0348
18.9706	0.9044	0.0169	0.0365
21.4879	0.9229	0.0198	0.0385

Table 3.5: ν dependence of multiplicity ratio $R_{Ne}^{\pi^-}$ from **Ne** target for negatively charged pions in $0.4 < z < 0.7$ slice.

ν bin (GeV)	$R_{Ne}^{\pi^-}$	statistical error(+/-)	total error(+/-)
5.1429	0.8158	0.0314	0.0727
7.1322	0.8011	0.0202	0.0561
9.0365	0.8050	0.0168	0.0507
10.9844	0.8472	0.0173	0.0492
12.9974	0.8650	0.0193	0.0509
14.9518	0.9134	0.0240	0.0532
16.8790	0.9201	0.0330	0.0547
18.8267	0.9159	0.0559	0.0678

Table 3.6: ν dependence of multiplicity ratio $R_{Ne}^{\pi^-}$ from **Ne** target for negatively charged pions in $z > 0.7$ slice.

ν bin (GeV)	$R_{Ne}^{K^+}$	statistical error(+/-)	total error(+/-)
7.2717	1.0283	0.0426	0.0703
9.1209	0.9219	0.0236	0.0504
11.0360	0.9444	0.0192	0.0548
13.0363	0.9535	0.0184	0.0550
14.9831	0.9909	0.0196	0.0573
16.9560	0.9685	0.0204	0.0564
19.0046	0.9690	0.0236	0.0577
21.5903	0.9684	0.0245	0.0580

Table 3.7: ν dependence of multiplicity ratio $R_{Ne}^{K^+}$ from **Ne** target for positively charged kaons in $0.2 < z < 0.4$ slice.

ν bin (GeV)	$R_{Ne}^{K^+}$	statistical error(+/-)	total error(+/-)
5.2537	1.0354	0.0571	0.0846
7.1442	0.9439	0.0309	0.0599
9.0767	0.8983	0.0225	0.0537
11.0031	0.9232	0.0203	0.0541
13.0294	0.9412	0.0203	0.0550
15.0043	0.9350	0.0216	0.0552
16.9527	0.9309	0.0244	0.0562
18.9741	0.9051	0.0295	0.0573
21.4442	0.9287	0.0346	0.0612

Table 3.8: ν dependence of multiplicity ratio $R_{Ne}^{K^+}$ from **Ne** target for positively charged kaons in $0.4 < z < 0.7$ slice.

ν bin (GeV)	$R_{Ne}^{K^+}$	statistical error(+/-)	total error(+/-)
5.1455	0.8906	0.0776	0.0943
7.1778	0.8216	0.0434	0.0622
9.0256	0.8638	0.0360	0.0591
10.9925	0.8417	0.0351	0.0576
12.9771	0.8338	0.0361	0.0579
14.9224	0.7975	0.0383	0.0578
16.9086	0.9505	0.0587	0.0782
18.7967	0.8305	0.0813	0.0930

Table 3.9: ν dependence of multiplicity ratio $R_{Ne}^{K^+}$ from **Ne** target for positively charged kaons in $z > 0.7$ slice.

ν bin (GeV)	$R_{Ne}^{K^-}$	statistical error(+/-)	total error(+/-)
7.2967	0.8187	0.0573	0.0725
9.1158	0.8502	0.0329	0.0567
11.0304	0.8422	0.0256	0.0524
13.0540	0.8419	0.0237	0.0515
15.0036	0.8769	0.0243	0.0535
16.9617	0.9102	0.0268	0.0562
19.0141	0.9059	0.0301	0.0577
21.6055	0.9256	0.0312	0.0592

Table 3.10: ν dependence of multiplicity ratio $R_{Ne}^{K^-}$ from **Ne** target for negatively charged kaons in $0.2 < z < 0.4$ slice.

ν bin (GeV)	$R_{Ne}^{K^-}$	statistical error(+/-)	total error(+/-)
5.2600	0.7151	0.0776	0.0888
7.2069	0.7723	0.0462	0.0624
9.0872	0.8139	0.0369	0.0576
11.0223	0.8257	0.0325	0.0554
13.0167	0.8534	0.0331	0.0570
14.9740	0.8977	0.0353	0.0602
16.9403	0.8670	0.0385	0.0608
18.9926	0.9405	0.0497	0.0713
21.5038	0.8602	0.0500	0.0684

Table 3.11: ν dependence of multiplicity ratio $R_{Ne}^{K^-}$ from **Ne** target for negatively charged kaons in $0.4 < z < 0.7$ slice.

ν bin (GeV)	$R_{Ne}^{K^-}$	statistical error(+/-)	total error(+/-)
5.0714	0.8338	0.2315	0.2369
7.0811	0.8526	0.1610	0.1675
9.1621	0.7466	0.1101	0.1173
10.9339	0.7117	0.0949	0.1025
13.0948	0.8394	0.1021	0.1118
15.0234	0.6239	0.0777	0.0848
17.0143	0.7737	0.1100	0.1178
18.8696	0.9333	0.1855	0.1923

Table 3.12: ν dependence of multiplicity ratio $R_{Ne}^{K^-}$ from **Ne** target for negatively charged kaons in $z > 0.7$ slice.

ν bin (GeV)	R^{p}_{Ne}	statistical error(+/-)	total error(+/-)
7.2397	0.9676	0.0256	0.0524
9.0543	1.0351	0.0203	0.0531
11.0059	1.0455	0.0191	0.0530
13.0147	1.0637	0.0191	0.0537
14.9901	1.0743	0.0200	0.0545
16.9403	1.0550	0.0220	0.0544
18.9810	1.0797	0.0270	0.0576
21.5415	1.0585	0.0281	0.0573

Table 3.13: ν dependence of multiplicity ratio R^{p}_{Ne} from **Ne** target for protons in $0.2 < z < 0.4$ slice.

ν bin (GeV)	R^{p}_{Ne}	statistical error(+/-)	total error(+/-)
5.1620	0.9482	0.0205	0.0804
7.0011	0.9850	0.0181	0.0499
8.9959	1.0296	0.0203	0.0526
10.9650	0.9812	0.0208	0.0507
12.9804	0.9625	0.0222	0.0505
14.9566	0.9905	0.0254	0.0532
16.9249	0.9358	0.0282	0.0524
18.9849	0.9810	0.0373	0.0594
21.4544	1.0014	0.0447	0.0651

Table 3.14: ν dependence of multiplicity ratio R^{p}_{Ne} from **Ne** target for protons in $0.4 < z < 0.7$ slice.

ν bin (GeV)	R^{p}_{Ne}	statistical error(+/-)	total error(+/-)
4.9147	0.8792	0.0432	0.0841
7.0119	0.9018	0.0514	0.0667
8.9671	0.9722	0.0577	0.0737
10.9142	0.9540	0.0589	0.0741
13.0369	0.9847	0.0694	0.0835
14.9194	1.0686	0.0947	0.1073
16.9011	0.8977	0.1061	0.1142
18.8700	0.9833	0.1731	0.1792

Table 3.15: ν dependence of multiplicity ratio R^{p}_{Ne} from **Ne** target for protons in $z > 0.7$ slice.

ν bin (GeV)	R^{p}_{Ne}	statistical error(+/-)	total error(+/-)
7.2645	0.9483	0.1143	0.1551
9.0883	1.2621	0.1539	0.2077
10.9866	0.6424	0.0620	0.0943
13.0139	0.6487	0.0417	0.0830
15.0005	0.8640	0.0430	0.1079
16.9612	0.7992	0.0396	0.0968
19.0233	0.9033	0.0481	0.1108
21.5458	0.8228	0.0438	0.1010

Table 3.16: ν dependence of multiplicity ratio $R^{\bar{p}}_{Ne}$ from **Ne** target for antiprotons in $0.2 < z < 0.4$ slice.

ν bin (GeV)	$R^{\bar{p}}_{Ne}$	statistical error(+/-)	total error(+/-)
5.2545	0.7177	0.0884	0.1298
6.9398	0.6703	0.0727	0.1049
9.0224	0.8694	0.0851	0.1277
11.0476	0.7463	0.0658	0.1049
12.9995	0.9281	0.0725	0.1249
15.0063	0.7724	0.0615	0.1046
16.9436	0.7952	0.0663	0.1095
18.9702	0.8776	0.0805	0.1254
21.5373	0.8930	0.0899	0.1329

Table 3.17: ν dependence of multiplicity ratio $R^{\bar{p}}_{Ne}$ from **Ne** target for antiprotons in $0.4 < z < 0.7$ slice.

ν bin (GeV)	$R^{\pi^+}_{Kr}$	statistical error(+/-)	total error(+/-)
5.6359	0.7036	0.0402	0.0631
7.2440	0.6932	0.0116	0.0277
9.1300	0.7396	0.0075	0.0284
11.0273	0.7516	0.0063	0.0285
13.0251	0.7770	0.0061	0.0294
14.9906	0.7962	0.0062	0.0299
16.9627	0.8092	0.0068	0.0305
19.0015	0.8349	0.0080	0.0317
21.5574	0.8785	0.0088	0.0334

Table 3.18: ν dependence of multiplicity ratio $R^{\pi^+}_{Kr}$ from **Kr** target for positively charged pions in $0.2 < z < 0.4$ slice.

ν bin (GeV)	$R_{Kr}^{\pi^+}$	statistical error(+/-)	total error(+/-)
5.2258	0.6610	0.0146	0.0473
7.1278	0.6693	0.0097	0.0245
9.0652	0.6858	0.0082	0.0244
11.0005	0.7080	0.0078	0.0250
13.0245	0.7273	0.0080	0.0257
14.9840	0.7567	0.0089	0.0269
16.9505	0.7701	0.0103	0.0278
18.9679	0.8266	0.0134	0.0308
21.4398	0.8572	0.0163	0.0331

Table 3.19: ν dependence of multiplicity ratio $R_{Kr}^{\pi^+}$ from **Kr** target for positively charged pions in $0.4 < z < 0.7$ slice.

ν bin (GeV)	$R_{Kr}^{\pi^+}$	statistical error(+/-)	total error(+/-)
5.1257	0.6161	0.0213	0.0519
7.1135	0.5577	0.0132	0.0303
9.0534	0.5917	0.0116	0.0300
10.9898	0.6159	0.0117	0.0294
13.0094	0.6318	0.0129	0.0306
14.9515	0.6986	0.0163	0.0333
16.8672	0.7256	0.0227	0.0359
18.8304	0.6985	0.0368	0.0445

Table 3.20: ν dependence of multiplicity ratio $R_{Kr}^{\pi^+}$ from **Kr** target for positively charged pions in $z > 0.7$ slice.

ν bin (GeV)	$R_{Kr}^{\pi^-}$	statistical error(+/-)	total error(+/-)
5.6012	0.6605	0.0407	0.0630
7.2839	0.7049	0.0126	0.0334
9.1169	0.7245	0.0080	0.0338
11.0217	0.7506	0.0068	0.0352
13.0316	0.7787	0.0066	0.0364
14.9833	0.7955	0.0068	0.0378
16.9623	0.8028	0.0075	0.0382
19.0021	0.8227	0.0086	0.0394
21.5657	0.8637	0.0094	0.0414

Table 3.21: ν dependence of multiplicity ratio $R_{Kr}^{\pi^-}$ from **Kr** target for negatively charged pions in $0.2 < z < 0.4$ slice.

ν bin (GeV)	$R^{\pi^-}_{Kr}$	statistical error(+/-)	total error(+/-)
5.2109	0.6374	0.0152	0.0469
7.1267	0.6765	0.0108	0.0271
9.0543	0.6813	0.0092	0.0267
10.9927	0.7102	0.0089	0.0276
13.0227	0.7316	0.0092	0.0284
14.9862	0.7446	0.0101	0.0292
16.9388	0.7823	0.0119	0.0311
18.9780	0.7866	0.0148	0.0325
21.4482	0.8483	0.0183	0.0361

Table 3.22: ν dependence of multiplicity ratio $R^{\pi^-}_{Kr}$ from **Kr** target for negatively charged pions in $0.4 < z < 0.7$ slice.

ν bin (GeV)	$R^{\pi^-}_{Kr}$	statistical error(+/-)	total error(+/-)
5.1822	0.6001	0.0243	0.0562
7.1362	0.5815	0.0158	0.0465
9.0490	0.5906	0.0133	0.0423
10.9987	0.6321	0.0138	0.0405
12.9916	0.6766	0.0157	0.0437
14.9694	0.7373	0.0200	0.0465
16.8700	0.8188	0.0294	0.0518
18.8349	0.8101	0.0491	0.0607

Table 3.23: ν dependence of multiplicity ratio $R^{\pi^-}_{Kr}$ from **Kr** target for negatively charged pions in $z > 0.7$ slice.

ν bin (GeV)	$R^{K^+}_{Kr}$	statistical error(+/-)	total error(+/-)
7.2355	0.9003	0.0402	0.0633
9.1284	0.8575	0.0230	0.0519
11.0110	0.9047	0.0186	0.0526
13.0335	0.9349	0.0179	0.0539
15.0093	0.9103	0.0176	0.0525
16.9537	0.9622	0.0194	0.0557
18.9992	0.9642	0.0222	0.0569
21.6195	0.9805	0.0242	0.0585

Table 3.24: ν dependence of multiplicity ratio $R^{K^+}_{Kr}$ from **Kr** target for positively charged kaons in $0.2 < z < 0.4$ slice.

ν bin (GeV)	$R_{Kr}^{K^+}$	statistical error(+/-)	total error(+/-)
5.2041	0.9065	0.0531	0.0763
7.1397	0.8368	0.0284	0.0563
9.0744	0.7539	0.0194	0.0453
11.0096	0.7936	0.0175	0.0465
13.0210	0.8073	0.0176	0.0472
14.9816	0.8497	0.0195	0.0501
16.9737	0.8394	0.0222	0.0507
18.9584	0.8911	0.0284	0.0561
21.4285	0.8948	0.0331	0.0588

Table 3.25: ν dependence of multiplicity ratio $R_{Kr}^{K^+}$ from **Kr** target for positively charged kaons in $0.4 < z < 0.7$ slice.

ν bin (GeV)	$R_{Kr}^{K^+}$	statistical error(+/-)	total error(+/-)
5.1716	0.7450	0.0669	0.0805
7.1397	0.7675	0.0408	0.0583
9.0541	0.7357	0.0319	0.0511
11.0317	0.7002	0.0295	0.0481
13.0304	0.6849	0.0306	0.0482
14.9763	0.7529	0.0358	0.0543
16.9284	0.7492	0.0457	0.0612
18.8397	0.7964	0.0747	0.0863

Table 3.26: ν dependence of multiplicity ratio $R_{Kr}^{K^+}$ from **Kr** target for positively charged kaons in $z > 0.7$ slice.

ν bin (GeV)	$R_{Kr}^{K^-}$	statistical error(+/-)	total error(+/-)
7.4250	0.6566	0.0503	0.0617
9.1531	0.6934	0.0290	0.0475
11.0468	0.7240	0.0227	0.0454
13.0198	0.7766	0.0221	0.0476
15.0068	0.7923	0.0224	0.0485
16.9798	0.8427	0.0242	0.0518
19.0035	0.8722	0.0281	0.0511
21.5910	0.9165	0.0297	0.0518

Table 3.27: ν dependence of multiplicity ratio $R_{Kr}^{K^-}$ from **Kr** target for negatively charged kaons in $0.2 < z < 0.4$ slice.

ν bin (GeV)	$R_{Kr}^{K^-}$	statistical error(+/-)	total error(+/-)
5.2834	0.6103	0.0725	0.0759
7.1634	0.6493	0.0406	0.0440
9.1178	0.6124	0.0295	0.0335
11.0337	0.7104	0.0286	0.0340
12.9731	0.7190	0.0281	0.0337
15.0066	0.7575	0.0303	0.0361
16.9519	0.8033	0.0360	0.0416
18.9638	0.7662	0.0412	0.0457
21.4876	0.8786	0.0496	0.0546

Table 3.28: ν dependence of multiplicity ratio $R_{Kr}^{K^-}$ from **Kr** target for negatively charged kaons in $0.4 < z < 0.7$ slice.

ν bin (GeV)	$R_{Kr}^{K^-}$	statistical error(+/-)	total error(+/-)
5.2556	0.4421	0.1567	0.1591
7.1119	0.4453	0.0939	0.0970
9.0790	0.6974	0.1014	0.1089
11.1358	0.7142	0.0894	0.0975
13.1244	0.6999	0.0819	0.0903
14.9903	0.5874	0.0733	0.0800
16.9105	0.6624	0.0928	0.0996
18.9913	0.7328	0.1474	0.1527

Table 3.29: ν dependence of multiplicity ratio $R_{Kr}^{K^-}$ from **Kr** target for negatively charged kaons in $z > 0.7$ slice.

ν bin (GeV)	R_{Kr}^{p}	statistical error(+/-)	total error(+/-)
7.2579	0.9065	0.0226	0.0485
9.0946	0.9845	0.0177	0.0499
11.0043	1.1217	0.0180	0.0562
13.0356	1.1268	0.0180	0.0562
14.9793	1.1792	0.0194	0.0589
16.9465	1.2389	0.0228	0.0627
18.9883	1.2593	0.0277	0.0655
21.5344	1.2380	0.0298	0.0656

Table 3.30: ν dependence of multiplicity ratio R_{Kr}^{p} from **Kr** target for protons in $0.2 < z < 0.4$ slice.

ν bin (GeV)	R^{p}_{Kr}	statistical error(+/-)	total error(+/-)
5.2030	0.7948	0.0169	0.0673
7.0134	0.8735	0.0156	0.0441
9.0200	0.9078	0.0174	0.0462
10.9823	0.8938	0.0184	0.0460
12.9931	0.9270	0.0202	0.0482
14.9600	0.9220	0.0221	0.0488
16.9347	0.9599	0.0266	0.0525
18.9820	0.9015	0.0324	0.0535
21.4726	0.9927	0.0424	0.0632

Table 3.31: ν dependence of multiplicity ratio R^{p}_{Kr} from **Kr** target for protons in $0.4 < z < 0.7$ slice.

ν bin (GeV)	R^{p}_{Kr}	statistical error(+/-)	total error(+/-)
4.9596	0.7995	0.0393	0.0764
7.0072	0.7425	0.0414	0.0542
8.9614	0.7733	0.0456	0.0584
10.9638	0.8037	0.0486	0.0616
13.0004	0.7406	0.0522	0.0628
14.9801	0.6231	0.0587	0.0656
16.9239	0.7412	0.0937	0.1001
18.8191	0.5236	0.1035	0.1066

Table 3.32: ν dependence of multiplicity ratio R^{p}_{Kr} from **Kr** target for protons in $z > 0.7$ slice.

ν bin (GeV)	R^{p}_{Kr}	statistical error(+/-)	total error(+/-)
7.3000	0.7001	0.0616	0.0984
9.1244	0.5809	0.0413	0.0844
11.0179	0.7183	0.0473	0.0922
13.1124	0.6113	0.0336	0.0766
14.9892	0.7553	0.0346	0.0925
16.9559	0.7599	0.0358	0.0906
19.0176	0.8160	0.0407	0.0982
21.6592	0.8594	0.0444	0.1041

Table 3.33: ν dependence of multiplicity ratio $R^{\bar{p}}_{Kr}$ from **Kr** target for antiprotons in $0.2 < z < 0.4$ slice.

ν bin (GeV)	R^{p}_{Kr}	statistical error(+/-)	total error(+/-)
5.1554	0.6879	0.0615	0.1077
7.0032	0.6186	0.0568	0.0884
9.0117	0.5683	0.0559	0.0837
11.0475	0.6618	0.0563	0.0918
13.0547	0.6626	0.0528	0.0898
15.0543	0.7541	0.0584	0.1012
16.9606	0.6210	0.0507	0.0848
18.9729	0.7123	0.0646	0.1013
21.5611	0.6503	0.0712	0.1007

Table 3.34: ν dependence of multiplicity ratio $R^{\bar{p}}_{Kr}$ from **Kr** target for antiprotons in $0.4 < z < 0.7$ slice.

ν bin (GeV)	$R^{\pi^+}_{Xe}$	statistical error(+/-)	total error(+/-)
5.6308	0.6328	0.0460	0.0636
7.2467	0.6377	0.0132	0.0272
9.1288	0.6538	0.0084	0.0264
11.0234	0.6928	0.0072	0.0275
13.0436	0.7244	0.0069	0.0286
14.9990	0.7468	0.0072	0.0291
16.9641	0.7601	0.0078	0.0297
18.9900	0.7768	0.0091	0.0307
21.5390	0.8380	0.0101	0.0332

Table 3.35: ν dependence of multiplicity ratio $R^{\pi^+}_{Xe}$ from **Xe** target for positively charged pions in $0.2 < z < 0.4$ slice.

ν bin (GeV)	$R^{\pi^+}_{Xe}$	statistical error(+/-)	total error(+/-)
5.2548	0.5913	0.0164	0.0434
7.1235	0.6011	0.0108	0.0229
9.0671	0.6112	0.0091	0.0224
11.0140	0.6505	0.0089	0.0236
13.0002	0.6781	0.0091	0.0245
14.9798	0.6913	0.0100	0.0253
16.9450	0.7232	0.0118	0.0270
18.9383	0.7551	0.0150	0.0294
21.3881	0.7865	0.0183	0.0321

Table 3.36: ν dependence of multiplicity ratio $R^{\pi^+}_{Xe}$ from **Xe** target for positively charged pions $0.4 < z < 0.7$ slice.

ν bin (GeV)	$R^{\pi^+}_{Xe}$	statistical error(+/-)	total error(+/-)
5.2297	0.5726	0.0243	0.0510
7.1501	0.5261	0.0153	0.0310
9.0573	0.5332	0.0130	0.0291
10.9828	0.5447	0.0130	0.0282
13.0034	0.5932	0.0148	0.0310
14.9347	0.6186	0.0181	0.0319
16.8801	0.6767	0.0259	0.0372
18.8148	0.6861	0.0434	0.0499

Table 3.37: ν dependence of multiplicity ratio $R^{\pi^+}_{Xe}$ from **Xe** target for positively charged pions $z > 0.7$ slice.

ν bin (GeV)	$R^{\pi^-}_{Xe}$	statistical error(+/-)	total error(+/-)
5.6299	0.6745	0.0496	0.0702
7.2676	0.6378	0.0141	0.0325
9.1417	0.6716	0.0092	0.0332
11.0208	0.7043	0.0079	0.0354
13.0282	0.7258	0.0076	0.0363
15.0101	0.7350	0.0078	0.0373
16.9691	0.7594	0.0085	0.0387
18.9790	0.7842	0.0099	0.0402
21.5287	0.8196	0.0108	0.0421

Table 3.38: ν dependence of multiplicity ratio $R^{\pi^-}_{Xe}$ from **Xe** target for negaitively charged pions in $0.2 < z < 0.4$ slice.

ν bin (GeV)	$R^{\pi^-}_{Xe}$	statistical error(+/-)	total error(+/-)
5.2051	0.5842	0.0172	0.0446
7.1152	0.6317	0.0123	0.0271
9.0490	0.6403	0.0106	0.0267
10.9844	0.6502	0.0101	0.0269
13.0210	0.6824	0.0106	0.0282
14.9856	0.7202	0.0118	0.0300
16.9331	0.7291	0.0135	0.0310
18.9506	0.7486	0.0171	0.0334
21.3593	0.7810	0.0204	0.0362

Table 3.39: ν dependence of multiplicity ratio $R^{\pi^-}_{Xe}$ from **Xe** target for negatively charged pions in $0.4 < z < 0.7$ slice.

ν bin (GeV)	$R^{\pi^-}_{Xe}$	statistical error(+/-)	total error(+/-)
5.2650	0.5567	0.0276	0.0551
7.1230	0.5301	0.0180	0.0468
9.0794	0.5477	0.0153	0.0448
10.9894	0.5908	0.0157	0.0398
12.9766	0.5999	0.0175	0.0411
14.9438	0.7026	0.0231	0.0472
16.8477	0.6928	0.0317	0.0492
18.7900	0.7178	0.0542	0.0643

Table 3.40: ν dependence of multiplicity ratio $R^{\pi^-}_{Xe}$ from **Xe** target for negatively charged pions in $z > 0.7$ slice.

ν bin (GeV)	$R^{K^+}_{Xe}$	statistical error(+/-)	total error(+/-)
7.3590	0.8114	0.0468	0.0643
9.1282	0.8191	0.0271	0.0521
11.0318	0.8331	0.0213	0.0500
13.0319	0.8818	0.0206	0.0521
14.9979	0.8734	0.0204	0.0516
16.9643	0.9175	0.0222	0.0545
19.0014	0.9305	0.0259	0.0568
21.5107	0.9750	0.0283	0.0601

Table 3.41: ν dependence of multiplicity ratio $R^{K^+}_{Xe}$ from **Xe** target for positively charged kaons in $0.2 < z < 0.4$ slice.

ν bin (GeV)	$R^{K^+}_{Xe}$	statistical error(+/-)	total error(+/-)
5.3125	0.9034	0.0656	0.0855
7.1648	0.7814	0.0327	0.0536
9.0798	0.7502	0.0231	0.0468
11.0198	0.7176	0.0196	0.0436
13.0073	0.7770	0.0204	0.0469
14.9690	0.7998	0.0224	0.0489
16.9267	0.8032	0.0257	0.0506
18.9699	0.8435	0.0327	0.0563
21.3959	0.9216	0.0400	0.0641

Table 3.42: ν dependence of multiplicity ratio $R^{K^+}_{Xe}$ from **Xe** target for positively charged kaons in $0.4 < z < 0.7$ slice.

ν bin (GeV)	$R_{Xe}^{K^+}$	statistical error(+/-)	total error(+/-)
4.9942	0.6713	0.0755	0.0856
7.1071	0.7059	0.0458	0.0597
9.0090	0.6691	0.0358	0.0510
10.8859	0.6548	0.0336	0.0489
13.0619	0.6634	0.0361	0.0510
14.9570	0.6445	0.0390	0.0524
16.8175	0.7016	0.0517	0.0642
18.9207	0.7464	0.0858	0.0949

Table 3.43: ν dependence of multiplicity ratio $R_{Xe}^{K^+}$ from **Xe** target for positively charged kaons in $z > 0.7$ slice.

ν bin (GeV)	$R_{Xe}^{K^-}$	statistical error(+/-)	total error(+/-)
7.3407	0.6079	0.0580	0.0667
9.1573	0.6292	0.0332	0.0476
11.0686	0.6937	0.0264	0.0460
13.0031	0.7171	0.0251	0.0463
14.9962	0.7878	0.0267	0.0504
16.9755	0.7665	0.0270	0.0496
19.0117	0.8501	0.0329	0.0567
21.5575	0.8593	0.0338	0.0576

Table 3.44: ν dependence of multiplicity ratio $R_{Xe}^{K^-}$ from **Xe** target for negatively charged kaons in $0.2 < z < 0.4$ slice.

ν bin (GeV)	$R_{Xe}^{K^-}$	statistical error(+/-)	total error(+/-)
5.2496	0.5979	0.0834	0.0908
7.0871	0.4981	0.0417	0.0497
9.1005	0.5718	0.0342	0.0462
11.0014	0.6581	0.0326	0.0484
13.0759	0.6783	0.0324	0.0491
14.9444	0.6998	0.0343	0.0512
16.9388	0.7727	0.0418	0.0593
18.9894	0.6847	0.0459	0.0591
21.5187	0.8244	0.0574	0.0728

Table 3.45: ν dependence of multiplicity ratio $R_{Xe}^{K^-}$ from **Xe** target for negatively charged kaons in $0.4 < z < 0.7$ slice.

ν bin (GeV)	$R_{Xe}^{K^-}$	statistical error(+/-)	total error(+/-)
4.8000	0.3977	0.1811	0.1827
6.9000	0.5300	0.1190	0.1224
8.6500	0.5282	0.0936	0.0979
10.6500	0.6069	0.0937	0.0993
13.4000	0.6939	0.0969	0.1040
14.8500	0.6061	0.0865	0.0926
16.5000	0.7106	0.1000	0.1072
18.3000	0.7375	0.1410	0.1466

Table 3.46: ν dependence of multiplicity ratio $R_{Xe}^{K^-}$ from **Xe** target for negatively charged kaons in $z > 0.7$ slice.

ν bin (GeV)	R_{Xe}^{p}	statistical error(+/-)	total error(+/-)
7.2556	0.8859	0.0262	0.0495
9.0956	0.9748	0.0205	0.0507
11.0030	1.0747	0.0205	0.0550
13.0184	1.1526	0.0214	0.0586
14.9774	1.1880	0.0228	0.0605
16.9513	1.2226	0.0264	0.0634
18.9702	1.2976	0.0330	0.0695
21.4798	1.3014	0.0359	0.0711

Table 3.47: ν dependence of multiplicity ratio R_{Xe}^{p} from **Xe** target for protons in $0.2 < z < 0.4$ slice.

ν bin (GeV)	R_{Xe}^{p}	statistical error(+/-)	total error(+/-)
5.1914	0.7535	0.0195	0.0648
7.0335	0.8131	0.0177	0.0422
9.0193	0.9063	0.0206	0.0475
10.9647	0.8505	0.0211	0.0453
12.9707	0.8675	0.0229	0.0469
14.9515	0.8628	0.0252	0.0479
16.9037	0.8989	0.0302	0.0521
18.8929	0.9446	0.0392	0.0594
21.3710	0.9986	0.0498	0.0686

Table 3.48: ν dependence of multiplicity ratio R_{Xe}^{p} from **Xe** target for protons in $0.4 < z < 0.7$ slice.

ν bin (GeV)	R^{p}_{Xe}	statistical error(+/-)	total error(+/-)
4.9050	0.6855	0.0422	0.0703
6.8813	0.7172	0.0480	0.0587
8.7429	0.7296	0.0515	0.0619
11.0000	0.6801	0.0522	0.0613
12.8750	0.6064	0.0549	0.0619
15.3000	0.6711	0.0737	0.0802
17.4600	0.6987	0.1112	0.1160
18.6667	0.5845	0.1301	0.1330

Table 3.49: ν dependence of multiplicity ratio R^{p}_{Xe} from **Xe** target for protons in $z > 0.7$ slice.

ν bin (GeV)	R^{p}_{Xe}	statistical error(+/-)	total error(+/-)
7.3432	0.6220	0.0638	0.0933
9.0407	0.6046	0.0470	0.0821
11.0204	0.6645	0.0509	0.0897
13.0783	0.6175	0.0392	0.0788
14.9398	0.7692	0.0410	0.0965
16.9587	0.7126	0.0407	0.0880
19.0214	0.7290	0.0449	0.0916
21.5629	0.8049	0.0496	0.1012

Table 3.50: ν dependence of multiplicity ratio $R^{\bar{p}}_{Xe}$ from **Xe** target for antiprotons in $0.2 < z < 0.4$ slice.

ν bin (GeV)	R^{p}_{Xe}	statistical error(+/-)	total error(+/-)
5.2183	0.5288	0.0613	0.0916
6.9205	0.6454	0.0670	0.0975
9.0711	0.6025	0.0681	0.0948
11.0510	0.3983	0.0500	0.0664
13.0575	0.6018	0.0598	0.0890
15.0186	0.7427	0.0677	0.1058
16.9382	0.6021	0.0592	0.0886
19.1057	0.6459	0.0721	0.1010
21.5546	0.7488	0.0902	0.1219

Table 3.51: ν dependence of multiplicity ratio $R^{\bar{p}}_{Xe}$ from **Xe** target for antiprotons in $0.4 < z < 0.7$ slice.

3.2 z dependence in three ν slices

In Figure 3.2, the dependence of R^{h}_{A} on **z** for three slices in ν is presented. The large attenuation at high **z** values explains differently in different phenomenology models. In parton energy loss modell this phenomena caused by the strong decrease of the fragmentation function at high **z** range while in absorbtion type models this is assumed to be a result of a decreasment of the formation length leading to the large energy losses in the nuclear medium.

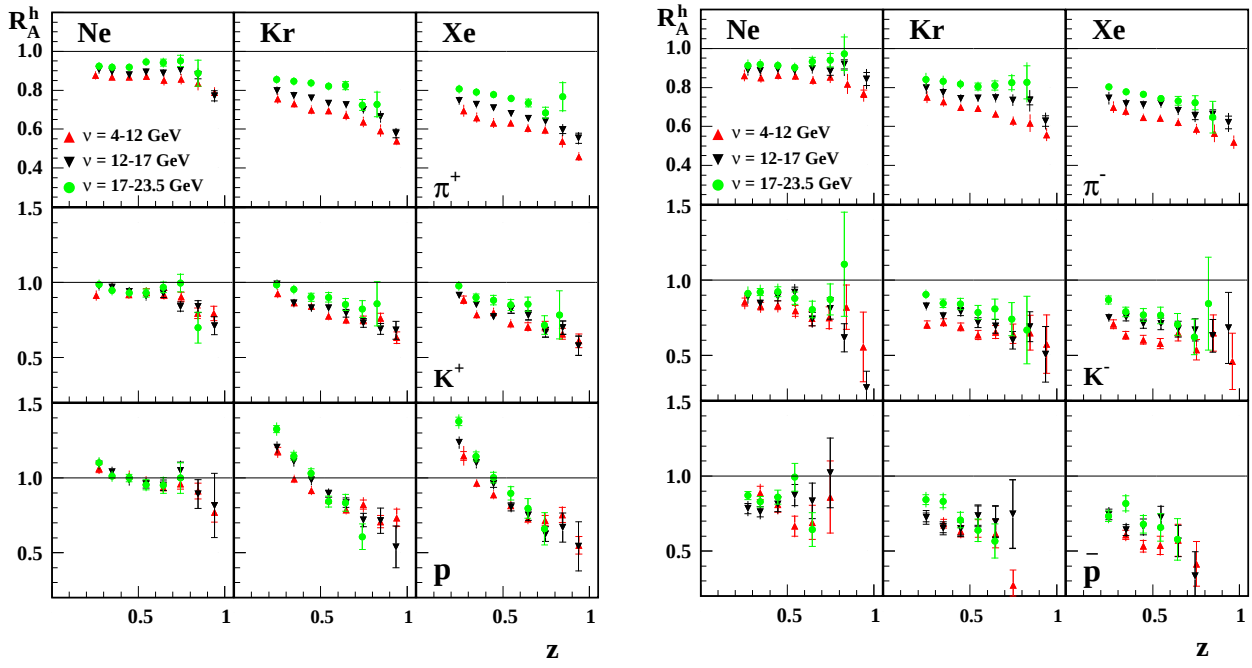

Figure 3.2: Dependence of R^{h}_{A} on **z** for three slices in ν.

Looking on experimental data one can see that the R^{h}_{A} shows a slight change in different

$\boldsymbol{\nu}$ slices for $\boldsymbol{\pi^+}$ and $\boldsymbol{\pi^-}$ and also a strong dependence is observed for $\mathbf{R_A^p}$ on **krypton** and **xenon** targets which might be understood as a result of low energy particle production due to high energy loss of an initial particle in final-state interaction at low **z** values.

It is also seen that the multiplicty ratio for the positively charged kaons is very close to the unity at small **z** while for the negatively charged kaons it is noticeably lower from unity. This phenomena might be caused by the transformation of the proton into $\mathbf{K^+\Lambda}$ pair whereas the similar transformation is suppressed for the negatively charged kaon due to it's quark content. For antiprotons the value of $\mathbf{R_A^{\bar{p}}}$ is clearly different that for protons. This is an indication that the final state interactions for antiprotons play a non-dominant role in contrast to protons.

The corresponding experimental data are shown in tables below **:**

z bin	$\mathbf{R_{Ne}^{\pi^+}}$	**statistical error(+/-)**	**total error(+/-)**
0.1879	**0.8839**	**0.0216**	**0.0405**
0.2530	**0.8768**	**0.0073**	**0.0345**
0.3475	**0.8673**	**0.0071**	**0.0317**
0.4468	**0.8674**	**0.0084**	**0.0308**
0.5471	**0.8717**	**0.0102**	**0.0314**
0.6474	**0.8518**	**0.0117**	**0.0370**
0.7478	**0.8567**	**0.0137**	**0.0373**
0.8462	**0.8345**	**0.0154**	**0.0439**
0.9411	**0.7880**	**0.0168**	**0.0355**

Table 3.52: **z** dependence of multiplicity ratio $\mathbf{R_{Ne}^{\pi^+}}$ from **Ne** target for positively charged pions in $\mathbf{4 < \nu < 12}$ **GeV** slice.

z bin	$\mathbf{R_{Ne}^{\pi^+}}$	**statistical error(+/-)**	**total error(+/-)**
0.1495	**0.9122**	**0.0047**	**0.0346**
0.2731	**0.9057**	**0.0054**	**0.0347**
0.3489	**0.8949**	**0.0067**	**0.0332**
0.4467	**0.8789**	**0.0084**	**0.0321**
0.5448	**0.8921**	**0.0107**	**0.0324**
0.6449	**0.8870**	**0.0130**	**0.0334**
0.7437	**0.9032**	**0.0159**	**0.0359**
0.8456	**0.8772**	**0.0191**	**0.0444**
0.9401	**0.7711**	**0.0253**	**0.0403**

Table 3.53: **z** dependence of multiplicity ratio $\mathbf{R_{Ne}^{\pi^+}}$ from **Ne** target for positively charged pions in $\mathbf{12 < \nu < 17}$ **GeV** slice.

z bin	$R_{Ne}^{\pi^+}$	statistical error(+/-)	total error(+/-)
0.0950	0.9376	0.0161	0.0380
0.1492	0.9290	0.0031	0.0350
0.2731	0.9233	0.0055	0.0353
0.3489	0.9177	0.0076	0.0342
0.4467	0.9179	0.0104	0.0340
0.5448	0.9456	0.0142	0.0354
0.6449	0.9419	0.0186	0.0376
0.7437	0.9501	0.0291	0.0446
0.8456	0.8874	0.0661	0.0775

Table 3.54: **z** dependence of multiplicity ratio $R_{Ne}^{\pi^+}$ from **Ne** target for positively charged pions in $17 < \nu < 23.5$ **GeV** slice.

z bin	$R_{Ne}^{\pi^-}$	statistical error(+/-)	total error(+/-)
0.1877	0.8777	0.0234	0.0452
0.2529	0.8612	0.0079	0.0390
0.3472	0.8501	0.0078	0.0362
0.4466	0.8616	0.0093	0.0337
0.5468	0.8593	0.0113	0.0335
0.6479	0.8362	0.0133	0.0341
0.7477	0.8532	0.0157	0.0400
0.8482	0.8180	0.0174	0.0568
0.9416	0.7680	0.0188	0.0465

Table 3.55: **z** dependence of multiplicity ratio $R_{Ne}^{\pi^-}$ from **Ne** target for negatively charged pions in $4 < \nu < 12$ **GeV** slice.

z bin	$R_{Ne}^{\pi^-}$	statistical error(+/-)	total error(+/-)
0.1495	0.9052	0.0051	0.0402
0.2729	0.8897	0.0058	0.0399
0.3440	0.8853	0.0075	0.0375
0.4451	0.8928	0.0097	0.0349
0.5438	0.8864	0.0124	0.0348
0.6440	0.8963	0.0154	0.0371
0.7482	0.8814	0.0185	0.0422
0.8288	0.9180	0.0234	0.0651
0.9579	0.8433	0.0326	0.0569

Table 3.56: **z** dependence of multiplicity ratio $R_{Ne}^{\pi^-}$ from **Ne** target for negatively charged pions in $12 < \nu < 17$ **GeV** slice.

z bin	$R_{Ne}^{\pi^-}$	statistical error(+/-)	total error(+/-)
0.0950	0.9192	0.0168	0.0432
0.1495	0.9109	0.0033	0.0402
0.2729	0.9128	0.0059	0.0409
0.3440	0.9178	0.0083	0.0390
0.4451	0.9133	0.0116	0.0362
0.5438	0.9024	0.0157	0.0366
0.6440	0.9323	0.0218	0.0413
0.7482	0.9404	0.0342	0.0530
0.8288	0.9724	0.0857	0.1071

Table 3.57: **z** dependence of multiplicity ratio $\mathbf{R_{Ne}^{\pi^-}}$ from **Ne** target for negatively charged pions in $\mathbf{17 < \nu < 23.5\ GeV}$ slice.

z bin	$R_{Ne}^{K^+}$	statistical error(+/-)	total error(+/-)
0.1902	1.1529	0.0980	0.1500
0.2567	0.9135	0.0202	0.0567
0.3479	0.9717	0.0196	0.0577
0.4453	0.9181	0.0202	0.0538
0.5473	0.9352	0.0231	0.0571
0.6482	0.9194	0.0269	0.0573
0.7480	0.9041	0.0315	0.0586
0.8427	0.7948	0.0350	0.0577
0.9467	0.7936	0.0480	0.0656

Table 3.58: **z** dependence of multiplicity ratio $\mathbf{R_{Ne}^{K^+}}$ from **Ne** target for positively charged kaons in $\mathbf{4 < \nu < 12\ GeV}$ slice.

z bin	$R_{Ne}^{K^+}$	statistical error(+/-)	total error(+/-)
0.1495	0.9696	0.0148	0.0560
0.2731	0.9751	0.0154	0.0565
0.3489	0.9689	0.0164	0.0564
0.4467	0.9401	0.0181	0.0554
0.5448	0.9097	0.0212	0.0550
0.6449	0.9282	0.0271	0.0584
0.7437	0.8392	0.0309	0.0561
0.8456	0.8399	0.0401	0.0616
0.9401	0.7114	0.0600	0.0719

Table 3.59: **z** dependence of multiplicity ratio $\mathbf{R_{Ne}^{K^+}}$ from **Ne** target for positively charged kaons in $\mathbf{12 < \nu < 17\ GeV}$ slice.

z bin	$R_{Ne}^{K^+}$	statistical error(+/-)	total error(+/-)
0.0950	0.9403	0.0759	0.0930
0.1495	0.9795	0.0105	0.0571
0.2731	0.9879	0.0157	0.0587
0.3489	0.9462	0.0172	0.0568
0.4467	0.9307	0.0215	0.0575
0.5448	0.9298	0.0268	0.0596
0.6449	0.9684	0.0355	0.0658
0.7437	0.9965	0.0590	0.0821
0.8456	0.6996	0.1032	0.1107

Table 3.60: **z** dependence of multiplicity ratio $\mathbf{R_{Ne}^{K^+}}$ from **Ne** target for positively charged kaons in $\mathbf{17 < \nu < 23.5\ GeV}$ slice.

z bin	$R_{Ne}^{K^-}$	statistical error(+/-)	total error(+/-)
0.1909	0.7802	0.1061	0.1187
0.2551	0.8546	0.0279	0.0646
0.3467	0.8284	0.0256	0.0621
0.4446	0.8333	0.0299	0.0642
0.5462	0.7968	0.0364	0.0654
0.6413	0.7449	0.0476	0.0696
0.7412	0.7498	0.0728	0.0890
0.8416	0.8210	0.1480	0.1582
0.9383	0.5553	0.2324	0.2355

Table 3.61: **z** dependence of multiplicity ratio $\mathbf{R_{Ne}^{K^-}}$ from **Ne** target for negatively charged kaons in $\mathbf{4 < \nu < 12\ GeV}$ slice.

z bin	$R_{Ne}^{K^-}$	statistical error(+/-)	total error(+/-)
0.1495	0.8822	0.0181	0.0629
0.2729	0.8893	0.0191	0.0636
0.3440	0.8470	0.0215	0.0617
0.4451	0.8912	0.0283	0.0671
0.5438	0.9184	0.0366	0.0726
0.6440	0.7410	0.0451	0.0678
0.7482	0.8119	0.0709	0.0900
0.8288	0.6173	0.0935	0.1026

Table 3.62: **z** dependence of multiplicity ratio $\mathbf{R_{Ne}^{K^-}}$ from **Ne** target for negatively charged kaons in $\mathbf{12 < \nu < 17\ GeV}$ slice.

z bin	$R_{Ne}^{K^-}$	statistical error(+/-)	total error(+/-)
0.1495	0.9303	0.0125	0.0647
0.2729	0.9129	0.0186	0.0650
0.3440	0.9213	0.0239	0.0673
0.4451	0.9245	0.0326	0.0710
0.5438	0.8796	0.0410	0.0727
0.6440	0.8046	0.0547	0.0775
0.7482	0.8718	0.1034	0.1193
0.8288	1.1076	0.3473	0.3555

Table 3.63: **z** dependence of multiplicity ratio $\mathbf{R_{Ne}^{K^-}}$ from **Ne** target for negatively charged kaons in $\mathbf{17 < \nu < 23.5}$ **GeV** slice.

z bin	R_{Ne}^{p}	statistical error(+/-)	total error(+/-)
0.2731	1.0638	0.0276	0.0577
0.3489	1.0178	0.0137	0.0505
0.4467	1.0138	0.0147	0.0534
0.5448	0.9793	0.0177	0.0507
0.6449	0.9358	0.0233	0.0503
0.7437	0.9606	0.0351	0.0584
0.8456	0.9124	0.0529	0.0693
0.9401	0.7690	0.0652	0.0750

Table 3.64: **z** dependence of multiplicity ratio $\mathbf{R_{Ne}^{p}}$ from **Ne** target for protons in $\mathbf{4 < \nu < 12}$ **GeV** slice.

z bin	R_{Ne}^{p}	statistical error(+/-)	total error(+/-)
0.2731	1.0922	0.0165	0.0565
0.3489	1.0407	0.0165	0.0541
0.4467	0.9836	0.0196	0.0525
0.5448	0.9571	0.0250	0.0536
0.6449	0.9504	0.0346	0.0584
0.7437	1.0489	0.0577	0.0776
0.8456	0.8918	0.0953	0.1050
0.9401	0.8156	0.2144	0.2182

Table 3.65: **z** dependence of multiplicity ratio $\mathbf{R_{Ne}^{p}}$ from **Ne** target for protons in $\mathbf{12 < \nu < 17}$ **GeV** slice.

z bin	R_{Ne}^{p}	statistical error(+/-)	total error(+/-)
0.2731	1.1017	0.0173	0.0572
0.3489	1.0106	0.0200	0.0538
0.4467	0.9992	0.0248	0.0553
0.5448	0.9539	0.0332	0.0577
0.6449	0.9499	0.0521	0.0702
0.7437	0.9990	0.1023	0.1136

Table 3.66: **z** dependence of multiplicity ratio $\mathbf{R_{Ne}^{p}}$ from **Ne** target for protons in $\mathbf{17 < \nu < 23.5}$ **GeV** slice.

z bin	R^{p}_{Ne}	statistical error(+/-)	total error(+/-)
0.3440	0.8875	0.0451	0.1080
0.4451	0.8103	0.0524	0.1038
0.5438	0.6664	0.0667	0.0994
0.6440	0.6910	0.1131	0.1365
0.7482	0.8602	0.2414	0.2595

Table 3.67: **z** dependence of multiplicity ratio $\mathbf{R^{\bar{p}}_{Ne}}$ from **Ne** target for antiprotons in $\mathbf{4 < \nu < 12}$ **GeV** slice.

z bin	R^{p}_{Ne}	statistical error(+/-)	total error(+/-)
0.2729	0.7831	0.0347	0.0933
0.3440	0.7618	0.0339	0.0908
0.4451	0.8121	0.0491	0.1023
0.5438	0.8727	0.0709	0.1197
0.6440	0.8344	0.1177	0.1495
0.7482	1.0213	0.2321	0.2581

Table 3.68: **z** dependence of multiplicity ratio $\mathbf{R^{\bar{p}}_{Ne}}$ from **Ne** target for antiprotons in $\mathbf{12 < \nu < 17}$ **GeV** slice.

z bin	R^{p}_{Ne}	statistical error(+/-)	total error(+/-)
0.2729	0.8698	0.0280	0.1001
0.3440	0.8284	0.0349	0.0980
0.4451	0.8584	0.0471	0.1059
0.5438	0.9918	0.0917	0.1429
0.6440	0.6432	0.1126	0.1332

Table 3.69: **z** dependence of multiplicity ratio $\mathbf{R^{\bar{p}}_{Ne}}$ from **Ne** target for antiprotons in $\mathbf{17 < \nu < 23.5}$ **GeV** slice.

z bin	$R^{\pi^+}_{Kr}$	statistical error(+/-)	total error(+/-)
0.1879	0.8213	0.0207	0.0399
0.2526	0.7563	0.0065	0.0346
0.3473	0.7310	0.0063	0.0305
0.4469	0.6988	0.0070	0.0303
0.5469	0.6949	0.0084	0.0273
0.6474	0.6705	0.0098	0.0313
0.7469	0.6366	0.0109	0.0326
0.8468	0.5925	0.0118	0.0360
0.9406	0.5390	0.0125	0.0269

Table 3.70: **z** dependence of multiplicity ratio $\mathbf{R^{\pi^+}_{Kr}}$ from **Kr** target for positively charged pions in $\mathbf{4 < \nu < 12}$ **GeV** slice.

z bin	$R^{\pi^+}_{Kr}$	statistical error(+/-)	total error(+/-)
0.1668	0.8341	0.0062	0.0327
0.2466	0.7979	0.0051	0.0314
0.3460	0.7726	0.0064	0.0297
0.4459	0.7603	0.0081	0.0288
0.5464	0.7328	0.0098	0.0273
0.6468	0.7257	0.0118	0.0282
0.7477	0.7007	0.0139	0.0295
0.8461	0.6641	0.0165	0.0370
0.9361	0.5775	0.0220	0.0338

Table 3.71: **z** dependence of multiplicity ratio $\mathbf{R^{\pi^+}_{Kr}}$ from **Kr** target for positively charged pions in $\mathbf{12 < \nu < 17}$ **GeV** slice.

z bin	$R^{\pi^+}_{Kr}$	statistical error(+/-)	total error(+/-)
0.0940	0.9506	0.0329	0.0403
0.1493	0.8885	0.0052	0.0237
0.2447	0.8552	0.0064	0.0235
0.3445	0.8456	0.0088	0.0227
0.4453	0.8363	0.0120	0.0225
0.5463	0.8211	0.0156	0.0227
0.6442	0.8236	0.0206	0.0269
0.7416	0.7242	0.0276	0.0326
0.8266	0.7269	0.0633	0.0700

Table 3.72: **z** dependence of multiplicity ratio $\mathbf{R^{\pi^+}_{Kr}}$ from **Kr** target for positively charged pions in $\mathbf{17 < \nu < 23.5}$ **GeV** slice.

z bin	$R^{\pi^-}_{Kr}$	statistical error(+/-)	total error(+/-)
0.1880	0.7994	0.0214	0.0438
0.2524	0.7507	0.0070	0.0376
0.3476	0.7264	0.0068	0.0325
0.4461	0.6987	0.0078	0.0284
0.5467	0.6934	0.0095	0.0275
0.6478	0.6637	0.0110	0.0282
0.7481	0.6271	0.0124	0.0310
0.8474	0.6174	0.0141	0.0489
0.9420	0.5578	0.0149	0.0376

Table 3.73: **z** dependence of multiplicity ratio $\mathbf{R^{\pi^-}_{Kr}}$ from **Kr** target for negatively charged pions in $\mathbf{4 < \nu < 12}$ **GeV** slice.

z bin	$R^{\pi^-}_{Kr}$	statistical error(+/-)	total error(+/-)
0.1665	0.8199	0.0065	0.0397
0.2468	0.7978	0.0056	0.0397
0.3454	0.7744	0.0071	0.0346
0.4459	0.7438	0.0090	0.0304
0.5458	0.7458	0.0114	0.0300
0.6469	0.7464	0.0141	0.0324
0.7465	0.7350	0.0169	0.0374
0.8450	0.7321	0.0207	0.0592
0.9357	0.6282	0.0270	0.0473

Table 3.74: **z** dependence of multiplicity ratio $\mathbf{R^{\pi^-}_{Kr}}$ from **Kr** target for negatively charged pions in $\mathbf{12 < \nu < 17}$ **GeV** slice.

z bin	$R^{\pi^-}_{Kr}$	statistical error(+/-)	total error(+/-)
0.0942	0.9156	0.0330	0.0527
0.1490	0.8771	0.0055	0.0422
0.2446	0.8411	0.0068	0.0419
0.3441	0.8315	0.0097	0.0375
0.4442	0.8167	0.0134	0.0345
0.5458	0.8046	0.0178	0.0347
0.6438	0.8098	0.0235	0.0394
0.7401	0.8241	0.0363	0.0520
0.8281	0.8256	0.0850	0.1056

Table 3.75: **z** dependence of multiplicity ratio $\mathbf{R^{\pi^-}_{Kr}}$ from **Kr** target for negatively charged pions in $\mathbf{17 < \nu < 23.5}$ **GeV** slice.

z bin	$R_{Kr}^{K^+}$	statistical error(+/-)	total error(+/-)
0.1879	1.0689	0.0901	0.1083
0.2526	0.9263	0.0209	0.0559
0.3473	0.8656	0.0180	0.0507
0.4469	0.8405	0.0187	0.0505
0.5469	0.7750	0.0198	0.0473
0.6474	0.7507	0.0226	0.0472
0.7469	0.7501	0.0267	0.0487
0.8268	0.7611	0.0342	0.0537
0.9406	0.6321	0.0392	0.0533

Table 3.76: **z** dependence of multiplicity ratio $\mathbf{R_{Kr}^{K^+}}$ from **Kr** target for positively charged kaons in $\mathbf{4 < \nu < 12}$ **GeV** slice.

z bin	$R_{Kr}^{K^+}$	statistical error(+/-)	total error(+/-)
0.1668	0.9860	0.0212	0.0589
0.2466	0.9900	0.0163	0.0575
0.3460	0.8621	0.0157	0.0505
0.4459	0.8310	0.0175	0.0495
0.5464	0.8301	0.0212	0.0509
0.6468	0.7953	0.0257	0.0512
0.7477	0.7298	0.0294	0.0502
0.8461	0.6897	0.0368	0.0532
0.9361	0.6815	0.0601	0.0711

Table 3.77: **z** dependence of multiplicity ratio $\mathbf{R_{Kr}^{K^+}}$ from **Kr** target for positively charged kaons in $\mathbf{12 < \nu < 17}$ **GeV** slice.

z bin	$R_{Kr}^{K^+}$	statistical error(+/-)	total error(+/-)
0.0940	1.1955	0.2046	0.2151
0.1493	1.0967	0.0196	0.0641
0.2447	0.9847	0.0186	0.0579
0.3445	0.9536	0.0216	0.0573
0.4453	0.9018	0.0264	0.0567
0.5463	0.9011	0.0322	0.0596
0.6442	0.8528	0.0394	0.0617
0.7416	0.8229	0.0563	0.0726
0.8266	0.8575	0.1476	0.1551

Table 3.78: **z** dependence of multiplicity ratio $\mathbf{R_{Kr}^{K^+}}$ from **Kr** target for positively charged kaons in $\mathbf{17 < \nu < 23.5}$ **GeV** slice.

z bin	$R_{Kr}^{K^-}$	statistical error(+/-)	total error(+/-)
0.1880	0.8101	0.1073	0.1164
0.2524	0.7039	0.0243	0.0461
0.3476	0.7193	0.0236	0.0465
0.4461	0.6897	0.0261	0.0465
0.5467	0.6346	0.0301	0.0464
0.6478	0.6550	0.0440	0.0572
0.7481	0.6434	0.0637	0.0731
0.8474	0.6498	0.1165	0.1220
0.9420	0.5748	0.1952	0.1978

Table 3.79: **z** dependence of multiplicity ratio $\mathbf{R_{Kr}^{K^-}}$ from **Kr** target for negatively charged kaons in $\mathbf{4 < \nu < 12}$ **GeV** slice.

z bin	$R_{Kr}^{K^-}$	statistical error(+/-)	total error(+/-)
0.1665	0.8299	0.0246	0.0524
0.2468	0.8271	0.0192	0.0499
0.3454	0.7621	0.0213	0.0475
0.4459	0.7911	0.0274	0.0519
0.5458	0.7183	0.0328	0.0518
0.6469	0.6927	0.0448	0.0591
0.7465	0.6010	0.0585	0.0674
0.8450	0.6903	0.0986	0.1058
0.9357	0.5063	0.1854	0.1875

Table 3.80: **z** dependence of multiplicity ratio $\mathbf{R_{Kr}^{K^-}}$ from **Kr** target for negatively charged kaons in $\mathbf{12 < \nu < 17}$ **GeV** slice.

z bin	$R_{Kr}^{K^-}$	statistical error(+/-)	total error(+/-)
0.1490	0.9384	0.0211	0.0563
0.2446	0.9058	0.0225	0.0552
0.3441	0.8458	0.0275	0.0545
0.4442	0.8409	0.0378	0.0602
0.5458	0.7849	0.0469	0.0641
0.6438	0.8080	0.0667	0.0804
0.7401	0.7413	0.1098	0.1173
0.8281	0.6688	0.2251	0.2282

Table 3.81: **z** dependence of multiplicity ratio $\mathbf{R_{Kr}^{K^-}}$ from **Kr** target for negatively charged kaons in $\mathbf{17 < \nu < 23.5}$ **GeV** slice.

z bin	R^{p}_{Kr}	statistical error(+/-)	total error(+/-)
0.2526	1.1789	0.0256	0.0646
0.3473	0.9928	0.0124	0.0486
0.4469	0.9151	0.0128	0.0478
0.5469	0.8513	0.0152	0.0492
0.6474	0.7868	0.0200	0.0445
0.7469	0.8215	0.0300	0.0601
0.8468	0.7077	0.0415	0.0545
0.9406	0.7332	0.0579	0.0766

Table 3.82: **z** dependence of multiplicity ratio $\mathbf{R^{p}_{Kr}}$ from **Kr** target for protons in $\mathbf{4 < \nu < 12}$ **GeV** slice.

z bin	R^{p}_{Kr}	statistical error(+/-)	total error(+/-)
0.2466	1.2042	0.0169	0.0620
0.3460	1.1111	0.0175	0.0577
0.4459	0.9865	0.0201	0.0528
0.5464	0.8945	0.0238	0.0503
0.6468	0.8336	0.0317	0.0520
0.7477	0.7183	0.0442	0.0567
0.8461	0.7136	0.0846	0.0917
0.9361	0.5388	0.1403	0.1428

Table 3.83: **z** dependence of multiplicity ratio $\mathbf{R^{p}_{Kr}}$ from **Kr** target for protons in $\mathbf{12 < \nu < 17}$ **GeV** slice.

z bin	R^{p}_{Kr}	statistical error(+/-)	total error(+/-)
0.2447	1.3258	0.0232	0.0695
0.3445	1.1448	0.0263	0.0623
0.4453	1.0302	0.0301	0.0591
0.5463	0.8420	0.0366	0.0554
0.6442	0.8331	0.0564	0.0698
0.7416	0.6062	0.0858	0.0909

Table 3.84: **z** dependence of multiplicity ratio $\mathbf{R^{p}_{Kr}}$ from **Kr** target for protons in $\mathbf{17 < \nu < 23.5}$ **GeV** slice.

z bin	R^{p}_{Kr}	statistical error(+/-)	total error(+/-)
0.3476	0.6822	0.0289	0.0808
0.4461	0.6316	0.0370	0.0790
0.5467	0.6500	0.0583	0.0925
0.6478	0.6158	0.0933	0.1155
0.7481	0.2719	0.1021	0.1064

Table 3.85: **z** dependence of multiplicity ratio $\mathbf{R^{\bar{p}}_{Kr}}$ from **Kr** target for antiprotons in $\mathbf{4 < \nu < 12}$ **GeV** slice.

z bin	R^{p}_{Kr}	statistical error(+/-)	total error(+/-)
0.2468	**0.7242**	**0.0297**	**0.0854**
0.3454	**0.6522**	**0.0308**	**0.0784**
0.4459	**0.6490**	**0.0433**	**0.0838**
0.5458	**0.7357**	**0.0639**	**0.1034**
0.6469	**0.6959**	**0.1019**	**0.1277**
0.7465	**0.7466**	**0.2266**	**0.2412**

Table 3.86: **z** dependence of multiplicity ratio $\mathbf{R^{\bar{p}}_{Kr}}$ from **Kr** target for antiprotons in $\mathbf{12 < \nu < 17}$ **GeV** slice.

z bin	R^{p}_{Kr}	statistical error(+/-)	total error(+/-)
0.2446	**0.8421**	**0.0325**	**0.0986**
0.3441	**0.8318**	**0.0436**	**0.1018**
0.4442	**0.7071**	**0.0509**	**0.0933**
0.5458	**0.6394**	**0.0754**	**0.1033**
0.6438	**0.5671**	**0.1141**	**0.1302**

Table 3.87: **z** dependence of multiplicity ratio $\mathbf{R^{\bar{p}}_{Kr}}$ from **Kr** target for antiprotons in $\mathbf{17 < \nu < 23.5}$ **GeV** slice.

z bin	$R^{\pi^+}_{Xe}$	statistical error(+/-)	total error(+/-)
0.1900	**0.7511**	**0.0177**	**0.0479**
0.2724	**0.6938**	**0.0075**	**0.0371**
0.3486	**0.6591**	**0.0070**	**0.0328**
0.4464	**0.6313**	**0.0078**	**0.0310**
0.5456	**0.6314**	**0.0095**	**0.0267**
0.6442	**0.6040**	**0.0110**	**0.0283**
0.7437	**0.5951**	**0.0124**	**0.0283**
0.8437	**0.5375**	**0.0133**	**0.0359**
0.9385	**0.4590**	**0.0136**	**0.0264**

Table 3.88: **z** dependence of multiplicity ratio $\mathbf{R^{\pi^+}_{Xe}}$ from **Xe** target for positively charged pions in $\mathbf{4 < \nu < 12}$ **GeV** slice.

z bin	$R_{Xe}^{\pi^+}$	statistical error(+/-)	total error(+/-)
0.1666	0.8001	0.0073	0.0321
0.2467	0.7462	0.0059	0.0309
0.3463	0.7265	0.0073	0.0289
0.4459	0.7080	0.0092	0.0273
0.5468	0.6795	0.0112	0.0261
0.6473	0.6540	0.0132	0.0266
0.7464	0.6397	0.0157	0.0285
0.8453	0.5953	0.0185	0.0362
0.9374	0.5530	0.0257	0.0363

Table 3.89: **z** dependence of multiplicity ratio $\mathbf{R_{Xe}^{\pi^+}}$ from **Xe** target for positively charged pions in $\mathbf{12 < \nu < 17}$ **GeV** slice.

z bin	$R_{Xe}^{\pi^+}$	statistical error(+/-)	total error(+/-)
0.0950	0.8960	0.0190	0.0393
0.1666	0.8512	0.0050	0.0335
0.2467	0.8058	0.0062	0.0333
0.3463	0.7892	0.0085	0.0315
0.4459	0.7775	0.0116	0.0305
0.5468	0.7572	0.0151	0.0303
0.6473	0.7349	0.0197	0.0325
0.7464	0.6843	0.0284	0.0381
0.8453	0.7668	0.0725	0.0828

Table 3.90: **z** dependence of multiplicity ratio $\mathbf{R_{Xe}^{\pi^+}}$ from **Xe** target for positively charged pions in $\mathbf{17 < \nu < 23.5}$ **GeV** slice.

z bin	$R_{Xe}^{\pi^-}$	statistical error(+/-)	total error(+/-)
0.1900	0.7481	0.0183	0.0411
0.2733	0.6986	0.0081	0.0368
0.3441	0.6783	0.0078	0.0315
0.4450	0.6460	0.0088	0.0270
0.5430	0.6427	0.0108	0.0273
0.6460	0.6208	0.0128	0.0280
0.7524	0.5868	0.0143	0.0322
0.8550	0.5641	0.0146	0.0486
0.9675	0.5200	0.0154	0.0377

Table 3.91: **z** dependence of multiplicity ratio $\mathbf{R_{Xe}^{\pi^-}}$ from **Xe** target for negatively charged pions in $\mathbf{4 < \nu < 12}$ **GeV** slice.

z bin	$R^{\pi^-}_{Xe}$	statistical error(+/-)	total error(+/-)
0.1665	0.7963	0.0077	0.0399
0.2469	0.7448	0.0064	0.0388
0.3454	0.7154	0.0080	0.0332
0.4459	0.7105	0.0104	0.0300
0.5461	0.7179	0.0133	0.0310
0.6467	0.6823	0.0159	0.0317
0.7450	0.6542	0.0187	0.0372
0.8464	0.6617	0.0233	0.0591
0.9365	0.6203	0.0322	0.0522

Table 3.92: **z** dependence of multiplicity ratio $\mathbf{R^{\pi^-}_{Xe}}$ from **Xe** target for negatively charged pions in $\mathbf{12 < \nu < 17}$ **GeV** slice.

z bin	$R^{\pi^-}_{Xe}$	statistical error(+/-)	total error(+/-)
0.0950	0.8862	0.0193	0.0458
0.1665	0.8521	0.0053	0.0422
0.2469	0.8034	0.0066	0.0418
0.3454	0.7783	0.0092	0.0362
0.4459	0.7654	0.0129	0.0329
0.5461	0.7439	0.0172	0.0337
0.6467	0.7308	0.0226	0.0370
0.7450	0.7213	0.0359	0.0504
0.8464	0.6479	0.0809	0.0968

Table 3.93: **z** dependence of multiplicity ratio $\mathbf{R^{\pi^-}_{Xe}}$ from **Xe** target for negatively charged pions in $\mathbf{17 < \nu < 23.5}$ **GeV** slice.

z bin	$R^{K^+}_{Xe}$	statistical error(+/-)	total error(+/-)
0.1850	1.0556	0.0802	0.1002
0.2724	0.8860	0.0247	0.0545
0.3486	0.7851	0.0204	0.0480
0.4464	0.7989	0.0215	0.0524
0.5456	0.7245	0.0225	0.0476
0.6442	0.7059	0.0260	0.0491
0.7437	0.7092	0.0306	0.0492
0.8437	0.6570	0.0370	0.0517
0.9385	0.6107	0.0452	0.0564

Table 3.94: **z** dependence of multiplicity ratio $\mathbf{R^{K^+}_{Xe}}$ from **Xe** target for positively charged kaons in $\mathbf{4 < \nu < 12}$ **GeV** slice.

z bin	$R_{Xe}^{K^+}$	statistical error(+/-)	total error(+/-)
0.1666	0.9657	0.0252	0.0594
0.2467	0.9140	0.0185	0.0542
0.3463	0.8531	0.0186	0.0511
0.4459	0.7701	0.0198	0.0473
0.5468	0.8195	0.0251	0.0521
0.6473	0.7809	0.0305	0.0531
0.7464	0.6679	0.0333	0.0499
0.8453	0.6977	0.0444	0.0590
0.9374	0.5775	0.0649	0.0724

Table 3.95: **z** dependence of multiplicity ratio $\mathbf{R_{Xe}^{K^+}}$ from **Xe** target for positively charged kaons in $\mathbf{12 < \nu < 17}$ **GeV** slice.

z bin	$R_{Xe}^{K^+}$	statistical error(+/-)	total error(+/-)
0.0940	1.0574	0.2281	0.2356
0.1492	1.0734	0.0231	0.0640
0.2449	0.9777	0.0220	0.0587
0.3448	0.8993	0.0246	0.0558
0.4446	0.8823	0.0309	0.0580
0.5460	0.8504	0.0369	0.0600
0.6436	0.8558	0.0467	0.0667
0.7406	0.7157	0.0615	0.0733
0.8264	0.7836	0.1602	0.1660

Table 3.96: **z** dependence of multiplicity ratio $\mathbf{R_{Xe}^{K^+}}$ from **Xe** target for positively charged kaons in $\mathbf{17 < \nu < 23.5}$ **GeV** slice.

z bin	$R_{Xe}^{K^-}$	statistical error(+/-)	total error(+/-)
0.1800	0.6555	0.0861	0.0935
0.2733	0.7076	0.0295	0.0492
0.3441	0.6328	0.0261	0.0439
0.4450	0.6030	0.0287	0.0442
0.5430	0.5780	0.0341	0.0469
0.6460	0.6491	0.0531	0.0643
0.7524	0.5378	0.0680	0.0743
0.8500	0.6482	0.1213	0.1266
0.9600	0.4591	0.1882	0.1899

Table 3.97: **z** dependence of multiplicity ratio $\mathbf{R_{Xe}^{K^-}}$ from **Xe** target for negatively charged kaons in $\mathbf{4 < \nu < 12}$ **GeV** slice.

z bin	$R_{Xe}^{K^-}$	statistical error(+/-)	total error(+/-)
0.1665	0.8565	0.0300	0.0564
0.2469	0.7503	0.0216	0.0471
0.3454	0.7553	0.0253	0.0491
0.4459	0.7113	0.0305	0.0500
0.5461	0.7097	0.0390	0.0555
0.6467	0.6750	0.0527	0.0648
0.7450	0.6690	0.0741	0.0830
0.8464	0.6296	0.1087	0.1142
0.9365	0.6817	0.2375	0.2405

Table 3.98: **z** dependence of multiplicity ratio $\mathbf{R_{Xe}^{K^-}}$ from **Xe** target for negatively charged kaons in $\mathbf{12 < \nu < 17}$ **GeV** slice.

z bin	$R_{Xe}^{K^-}$	statistical error(+/-)	total error(+/-)
0.1489	0.9067	0.0246	0.0561
0.2441	0.8687	0.0261	0.0549
0.3440	0.7889	0.0312	0.0539
0.4455	0.7687	0.0426	0.0604
0.5442	0.7659	0.0556	0.0700
0.6427	0.7058	0.0731	0.0830
0.7393	0.6219	0.1182	0.1231
0.8207	0.8448	0.3095	0.3131

Table 3.99: **z** dependence of multiplicity ratio $\mathbf{R_{Xe}^{K^-}}$ from **Xe** target for negatively charged kaons in $\mathbf{17 < \nu < 23.5}$ **GeV** slice.

z bin	R_{Xe}^{p}	statistical error(+/-)	total error(+/-)
0.2724	1.1469	0.0292	0.0676
0.3486	0.9654	0.0142	0.0320
0.4464	0.8875	0.0148	0.0337
0.5456	0.8142	0.0175	0.0364
0.6442	0.7244	0.0226	0.0357
0.7437	0.7160	0.0323	0.0505
0.8437	0.7528	0.0506	0.0583
0.9385	0.5498	0.0579	0.0638

Table 3.100: **z** dependence of multiplicity ratio $\mathbf{R_{Xe}^{p}}$ from **Xe** target for protons in $\mathbf{4 < \nu < 12}$ **GeV** slice.

z bin	R^{p}_{Xe}	statistical error(+/-)	total error(+/-)
0.2467	1.2364	0.0200	0.0644
0.3463	1.1004	0.0205	0.0582
0.4459	0.9592	0.0234	0.0529
0.5468	0.8062	0.0265	0.0479
0.6473	0.7511	0.0347	0.0509
0.7464	0.6250	0.0485	0.0575
0.8453	0.6689	0.0972	0.1027
0.9374	0.5420	0.1647	0.1669

Table 3.101: **z** dependence of multiplicity ratio $\mathbf{R^{p}_{Xe}}$ from **Xe** target for protons in $\mathbf{12 < \nu < 17}$ **GeV** slice.

z bin	R^{p}_{Xe}	statistical error(+/-)	total error(+/-)
0.2449	1.3770	0.0278	0.0735
0.3448	1.1427	0.0308	0.0643
0.4446	1.0017	0.0347	0.0604
0.5460	0.8968	0.0452	0.0633
0.6436	0.7954	0.0653	0.0762
0.7406	0.6603	0.1076	0.1125

Table 3.102: **z** dependence of multiplicity ratio $\mathbf{R^{p}_{Xe}}$ from **Xe** target for protons in $\mathbf{17 < \nu < 23.5}$ **GeV** slice.

z bin	R^{p}_{Xe}	statistical error(+/-)	total error(+/-)
0.3441	0.6079	0.0309	0.0740
0.4450	0.5323	0.0389	0.0705
0.5430	0.5370	0.0609	0.0851
0.6460	0.5720	0.1066	0.1239
0.7524	0.4146	0.1490	0.1559

Table 3.103: **z** dependence of multiplicity ratio $\mathbf{R^{\bar{p}}_{Xe}}$ from **Xe** target for antiprotons in $\mathbf{4 < \nu < 12}$ **GeV** slice.

z bin	$R^{\bar{p}}_{Xe}$	statistical error(+/-)	total error(+/-)
0.2469	**0.7447**	**0.0350**	**0.0895**
0.3454	**0.6402**	**0.0362**	**0.0795**
0.4459	**0.6617**	**0.0525**	**0.0900**
0.5461	**0.7246**	**0.0746**	**0.1095**
0.6467	**0.5668**	**0.1044**	**0.1218**
0.7450	**0.3331**	**0.1614**	**0.1655**

Table 3.104: **z** dependence of multiplicity ratio $\mathbf{R^{\bar{p}}_{Xe}}$ from **Xe** target for antiprotons in $\mathbf{12 < \nu < 17}$ **GeV** slice.

z bin	$R^{\bar{p}}_{Xe}$	statistical error(+/-)	total error(+/-)
0.2441	**0.7334**	**0.0351**	**0.0881**
0.3440	**0.8179**	**0.0508**	**0.1035**
0.4455	**0.6796**	**0.0587**	**0.0952**
0.5442	**0.6573**	**0.0905**	**0.1159**
0.6427	**0.5777**	**0.1394**	**0.1532**

Table 3.105: **z** dependence of multiplicity ratio $\mathbf{R^{\bar{p}}_{Xe}}$ from **Xe** target for antiprotons in $\mathbf{17 < \nu < 23.5}$ **GeV** slice.

3.3 p_t^2 dependence in three z slices

The dependence of R_A^h on p_t^2 is shown in Figure 3.3 for three slices in **z**. An increasing behaviour of R_A^h was observed at high p_t^2 (the **Cronin effect**[37]) which is larger for protons compared with mesons. This effect depends also on target mass which was observed by the **HERMES** collaboration before[38].

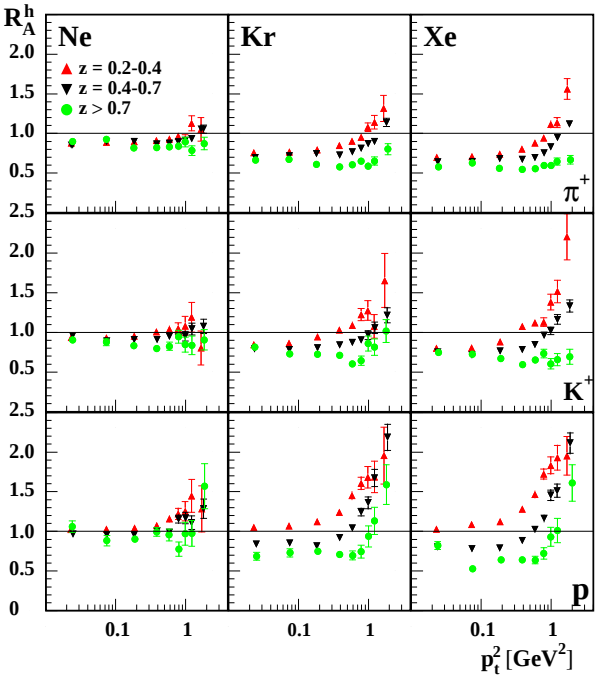

Figure 3.3: Dependence of R_A^h on p_t^2 for three slices in **z**.

In contrast to heavy ion collision experiments[37] the lepton-nucleon interaction is not contributed by the initial state interaction. The observed enhancment of R_A^h assumed the p_t broadening due to the multiple scattering of the struck quark and also the interaction of produced hadron with nuclear enviorement. There are different phenomenological models[39],[40] trying to explain the **Cronin effect**.

What we see in our data, for the highest **z** slice the **Cronin effect** is suppressed for mesons while the protons show a significant rise with p_t^2. Such a suppression reveals a partonic origin of the trasnverse momentum broadening. The point is that at high **z** the partonic energy loss is highly suppressed[11]. Due to the limited statistics only the data for positively charged hadrons are presented. The related tables for Figure 3.3 are presented below **:**

$\mathbf{p_t^2}$ $\mathbf{(GeV^2)}$	$\mathbf{R_{Ne}^{\pi^+}}$	statistical error(+/-)	total error(+/-)
0.0232	**0.8786**	**0.0053**	**0.0321**
0.0737	**0.8899**	**0.0067**	**0.0327**
0.1840	**0.8965**	**0.0048**	**0.0326**
0.3826	**0.9134**	**0.0088**	**0.0341**
0.5836	**0.9303**	**0.0167**	**0.0374**
0.7845	**0.9645**	**0.0311**	**0.0466**
0.9841	**0.9304**	**0.0524**	**0.0622**
1.2206	**1.1266**	**0.0946**	**0.1029**
1.6532	**1.0512**	**0.1484**	**0.1532**

Table 3.106: $\mathbf{p_t^2}$ dependence of multiplicity ratio $\mathbf{R_{Ne}^{\pi^+}}$ from **Ne** target for positively charged pions in $\mathbf{0.2 < z < 0.4}$ slice.

$\mathbf{p_t^2}$ $\mathbf{(GeV^2)}$	$\mathbf{R_{Ne}^{\pi^+}}$	statistical error(+/-)	total error(+/-)
0.0243	**0.8516**	**0.0082**	**0.0293**
0.0745	**0.8992**	**0.0096**	**0.0312**
0.1830	**0.8984**	**0.0065**	**0.0304**
0.3889	**0.8667**	**0.0103**	**0.0304**
0.5890	**0.8752**	**0.0151**	**0.0326**
0.7887	**0.8929**	**0.0224**	**0.0370**
0.9913	**0.9117**	**0.0316**	**0.0436**
1.2278	**0.9326**	**0.0397**	**0.0502**
1.8093	**1.0538**	**0.0533**	**0.0636**

Table 3.107: $\mathbf{p_t^2}$ dependence of multiplicity ratio $\mathbf{R_{Ne}^{\pi^+}}$ from **Ne** target for positively charged pions in $\mathbf{0.4 < z < 0.7}$ slice.

$\mathbf{p_t^2}$ $\mathbf{(GeV^2)}$	$\mathbf{R_{Ne}^{\pi^+}}$	statistical error(+/-)	total error(+/-)
0.0242	**0.8966**	**0.0150**	**0.0377**
0.0734	**0.9262**	**0.0178**	**0.0399**
0.1823	**0.8178**	**0.0112**	**0.0335**
0.3872	**0.8198**	**0.0184**	**0.0366**
0.5883	**0.8297**	**0.0281**	**0.0426**
0.7904	**0.8375**	**0.0413**	**0.0524**
0.9872	**0.8920**	**0.0601**	**0.0692**
1.2293	**0.7837**	**0.0601**	**0.0673**
1.8417	**0.8714**	**0.0787**	**0.0856**

Table 3.108: $\mathbf{p_t^2}$ dependence of multiplicity ratio $\mathbf{R_{Ne}^{\pi^+}}$ from **Ne** target for positively charged pions in $\mathbf{z > 0.7}$ slice.

p_t^2 (GeV^2)	$R_{Ne}^{K^+}$	statistical error(+/-)	total error(+/-)
0.0230	0.9360	0.0137	0.0526
0.0735	0.9310	0.0180	0.0536
0.1848	0.9537	0.0130	0.0534
0.3846	1.0062	0.0229	0.0593
0.5845	1.0386	0.0411	0.0697
0.7869	1.0498	0.0706	0.0903
0.9816	1.0823	0.1180	0.1317
1.2093	1.1914	0.1870	0.1964
1.6596	0.8037	0.2149	0.2174

Table 3.109: p_t^2 dependence of multiplicity ratio $R_{Ne}^{K^+}$ from **Ne** target for positively charged kaons in $0.2 < z < 0.4$ slice.

p_t^2 (GeV^2)	$R_{Ne}^{K^+}$	statistical error(+/-)	total error(+/-)
0.0236	0.9585	0.0191	0.0554
0.0740	0.8905	0.0208	0.0526
0.1860	0.9074	0.0142	0.0513
0.3888	0.9108	0.0215	0.0539
0.5919	0.9501	0.0310	0.0601
0.7902	0.9416	0.0429	0.0608
0.9882	0.9522	0.0605	0.0797
1.2241	1.0426	0.0768	0.0946
1.8255	1.0760	0.0916	0.1086

Table 3.110: p_t^2 dependence of multiplicity ratio $R_{Ne}^{K^+}$ from **Ne** target for positively charged kaons in $0.4 < z < 0.7$ slice.

p_t^2 (GeV^2)	$R_{Ne}^{K^+}$	statistical error(+/-)	total error(+/-)
0.0241	0.9056	0.0413	0.0642
0.0737	0.8758	0.0441	0.0647
0.1859	0.8304	0.0259	0.0520
0.3873	0.7966	0.0353	0.0558
0.5882	0.8256	0.0512	0.0675
0.7972	0.9455	0.0800	0.0946
0.9910	0.8477	0.0957	0.1060
1.2284	0.8375	0.1164	0.1244
1.8673	0.9063	0.1316	0.1386

Table 3.111: p_t^2 dependence of multiplicity ratio $R_{Ne}^{K^+}$ from **Ne** target for positively charged kaons in $z > 0.7$ slice.

p_t^2 (GeV^2)	R_{Ne}^p	statistical error(+/-)	total error(+/-)
0.0228	1.0235	0.0137	0.0502
0.0735	1.0268	0.0179	0.0507
0.1851	1.0406	0.0131	0.0508
0.3854	1.0732	0.0221	0.0552
0.5839	1.1576	0.0394	0.0673
0.7856	1.2210	0.0707	0.0912
0.9829	1.2549	0.1226	0.1361
1.2198	1.4466	0.2079	0.2188
1.7009	1.2838	0.2927	0.2989

Table 3.112: p_t^2 dependence of multiplicity ratio R_{Ne}^p from **Ne** target for protons in $0.2 < z < 0.4$ slice.

p_t^2 (GeV^2)	R_{Ne}^p	statistical error(+/-)	total error(+/-)
0.0246	0.9651	0.0173	0.0487
0.0745	0.9569	0.0188	0.0489
0.1844	0.9566	0.0127	0.0469
0.3898	1.0062	0.0214	0.0521
0.5885	0.9872	0.0307	0.0558
0.7875	1.1538	0.0506	0.0743
0.9925	1.1681	0.0733	0.0917
1.2219	1.1082	0.0857	0.1004
1.8106	1.2865	0.1231	0.1373

Table 3.113: p_t^2 dependence of multiplicity ratio R_{Ne}^p from **Ne** target for protons in $0.4 < z < 0.7$ slice.

p_t^2 (GeV^2)	R_{Ne}^p	statistical error(+/-)	total error(+/-)
0.0240	1.0605	0.0737	0.0891
0.0749	0.8824	0.0637	0.0761
0.1888	0.9004	0.0369	0.0563
0.3868	0.9932	0.0545	0.0719
0.5823	0.9546	0.0762	0.0885
0.8002	0.7749	0.0897	0.0969
0.9825	0.9698	0.1460	0.0153
1.2258	0.9749	0.1624	0.1688
1.8652	1.5688	0.2837	0.2932

Table 3.114: p_t^2 dependence of multiplicity ratio R_{Ne}^p from **Ne** target for protons in $z > 0.7$ slice.

p_t^2 (GeV^2)	$R_{Kr}^{\pi^+}$	statistical error(+/-)	total error(+/-)
0.0231	0.7581	0.0046	0.0284
0.0739	0.7652	0.0058	0.0289
0.1844	0.7926	0.0042	0.0296
0.3833	0.8504	0.0080	0.0324
0.5841	0.9040	0.0156	0.0369
0.7848	0.9500	0.0289	0.0455
0.9852	1.0776	0.0548	0.0678
1.2196	1.1418	0.0845	0.0945
1.6453	1.3170	0.1643	0.1714

Table 3.115: p_t^2 dependence of multiplicity ratio $R_{Kr}^{\pi^+}$ from **Kr** target for positively charged pions in $0.2 < z < 0.4$ slice.

p_t^2 (GeV^2)	$R_{Kr}^{\pi^+}$	statistical error(+/-)	total error(+/-)
0.0241	0.6943	0.0071	0.0243
0.0745	0.7158	0.0079	0.0253
0.1816	0.7462	0.0055	0.0256
0.3885	0.7256	0.0088	0.0259
0.5895	0.7649	0.0133	0.0289
0.7889	0.8126	0.0199	0.0337
0.9902	0.8704	0.0296	0.0416
1.2287	0.8971	0.0372	0.0478
1.8148	1.1383	0.0522	0.0647

Table 3.116: p_t^2 dependence of multiplicity ratio $R_{Kr}^{\pi^+}$ from **Kr** target for positively charged pions in $0.4 < z < 0.7$ slice.

p_t^2 (GeV^2)	$R_{Kr}^{\pi^+}$	statistical error(+/-)	total error(+/-)
0.0244	0.6648	0.0118	0.0302
0.0736	0.6711	0.0138	0.0313
0.1808	0.6106	0.0089	0.0271
0.3868	0.5797	0.0142	0.0281
0.5870	0.6052	0.0220	0.0336
0.7901	0.6483	0.0322	0.0421
0.9924	0.5853	0.0418	0.0485
1.2226	0.6511	0.0531	0.0597
1.9074	0.8015	0.0690	0.0767

Table 3.117: p_t^2 dependence of multiplicity ratio $R_{Kr}^{\pi^+}$ from **Kr** target for positively charged pions in $z > 0.7$ slice.

p_t^2 (GeV^2)	$R_{Kr}^{K^+}$	statistical error(+/-)	total error(+/-)
0.0230	0.8459	0.0125	0.0476
0.0735	0.8651	0.0166	0.0498
0.1866	0.9466	0.0126	0.0529
0.3832	1.0321	0.0224	0.0604
0.5867	1.0910	0.0401	0.0716
0.7884	1.2239	0.0767	0.1015
0.9798	1.2764	0.1239	0.1420
1.2088	1.0759	0.1505	0.1615
1.7124	1.6546	0.3399	0.3516

Table 3.118: p_t^2 dependence of multiplicity ratio $R_{Kr}^{K^+}$ from **Kr** target for positively charged kaons in $0.2 < z < 0.4$ slice.

p_t^2 (GeV^2)	$R_{Kr}^{K^+}$	statistical error(+/-)	total error(+/-)
0.0236	0.7897	0.0162	0.0458
0.0743	0.7808	0.0185	0.0463
0.1867	0.8053	0.0128	0.0456
0.3897	0.8402	0.0197	0.0497
0.5896	0.8747	0.0280	0.0551
0.7906	0.9029	0.0406	0.0637
0.9900	0.9667	0.0569	0.0774
1.2313	1.0558	0.0722	0.0922
1.8626	1.2160	0.0947	0.1155

Table 3.119: p_t^2 dependence of multiplicity ratio $R_{Kr}^{K^+}$ from **Kr** target for positively charged kaons in $0.4 < z < 0.7$ slice.

p_t^2 (GeV^2)	$R_{Kr}^{K^+}$	statistical error(+/-)	total error(+/-)
0.0239	0.8122	0.0373	0.0578
0.0753	0.7271	0.0376	0.0545
0.1875	0.7263	0.0227	0.0455
0.3891	0.7120	0.0318	0.0501
0.5885	0.6031	0.0398	0.0515
0.7908	0.6438	0.0592	0.0688
0.9979	0.8581	0.0943	0.1052
1.2207	0.8150	0.1036	0.1127
1.7916	1.0173	0.1426	0.1529

Table 3.120: p_t^2 dependence of multiplicity ratio $R_{Kr}^{K^+}$ from **Kr** target for positively charged kaons in $z > 0.7$ slice.

p_t^2 (GeV^2)	R_{Kr}^p	statistical error(+/-)	total error(+/-)
0.0230	1.0529	0.0129	0.0515
0.0733	1.0673	0.0169	0.0532
0.1857	1.1224	0.0126	0.0545
0.3863	1.2401	0.0223	0.0626
0.5843	1.4514	0.0427	0.0807
0.7857	1.6064	0.0779	0.1087
0.9826	1.6831	0.1350	0.1566
1.2239	1.6862	0.1987	0.2140
1.6638	1.9557	0.3579	0.3696

Table 3.121: p_t^2 dependence of multiplicity ratio R_{Kr}^p from **Kr** target for protons in $0.2 < z < 0.4$ slice.

p_t^2 (GeV^2)	R_{Kr}^p	statistical error(+/-)	total error(+/-)
0.0250	0.8405	0.0149	0.0424
0.0746	0.8514	0.0163	0.0433
0.1835	0.8147	0.0106	0.0399
0.3903	0.9210	0.0186	0.0473
0.5910	1.0408	0.0294	0.0572
0.7879	1.2434	0.0479	0.0757
0.9926	1.3612	0.0754	0.0990
1.2289	1.6749	0.1085	0.1342
1.8849	2.1867	0.1653	0.1949

Table 3.122: p_t^2 dependence of multiplicity ratio R_{Kr}^p from **Kr** target for protons in $0.4 < z < 0.7$ slice.

p_t^2 (GeV^2)	R_{Kr}^p	statistical error(+/-)	total error(+/-)
0.0253	0.6855	0.0497	0.0593
0.0756	0.7289	0.0531	0.0633
0.1893	0.7469	0.0304	0.0465
0.3904	0.7081	0.0397	0.0519
0.5933	0.6960	0.0557	0.0647
0.7865	0.7431	0.0815	0.0887
1.0052	0.9366	0.1327	0.1399
1.2259	1.1314	0.1724	0.1805
1.8090	1.5900	0.2520	0.2629

Table 3.123: p_t^2 dependence of multiplicity ratio R_{Kr}^p from **Kr** target for protons in $z > 0.7$ slice.

p_t^2 (GeV^2)	$R_{Xe}^{\pi^+}$	statistical error(+/-)	total error(+/-)
0.0232	0.6979	0.0038	0.0270
0.0736	0.7101	0.0048	0.0276
0.1849	0.7402	0.0034	0.0285
0.3834	0.8049	0.0063	0.0315
0.5833	0.8784	0.0121	0.0357
0.7836	0.9450	0.0222	0.0425
0.9867	1.1131	0.0426	0.0603
1.2179	1.1361	0.0631	0.0766
1.6966	1.5603	0.1302	0.1433

Table 3.124: p_t^2 dependence of multiplicity ratio $R_{Xe}^{\pi^+}$ from **Xe** target for positively charged pions in $0.2 < z < 0.4$ slice.

p_t^2 (GeV^2)	$R_{Xe}^{\pi^+}$	statistical error(+/-)	total error(+/-)
0.0241	0.6394	0.0059	0.0222
0.0744	0.6462	0.0066	0.0227
0.1843	0.6796	0.0045	0.0232
0.3888	0.6711	0.0071	0.0236
0.5892	0.6928	0.0104	0.0255
0.7906	0.7520	0.0156	0.0297
0.9895	0.8285	0.0232	0.0362
1.2313	0.9456	0.0304	0.0439
1.8261	1.1169	0.0404	0.0551

Table 3.125: p_t^2 dependence of multiplicity ratio $R_{Xe}^{\pi^+}$ from **Xe** target for positively charged pions in $0.4 < z < 0.7$ slice.

p_t^2 (GeV^2)	$R_{Xe}^{\pi^+}$	statistical error(+/-)	total error(+/-)
0.0245	0.5793	0.0097	0.0268
0.0744	0.6253	0.0118	0.0295
0.1819	0.5590	0.0076	0.0253
0.3867	0.5464	0.0122	0.0266
0.5920	0.5572	0.0184	0.0303
0.7887	0.5976	0.0268	0.0372
0.9953	0.5960	0.0374	0.0454
1.2186	0.6457	0.0455	0.0534
1.8794	0.6673	0.0526	0.0600

Table 3.126: p_t^2 dependence of multiplicity ratio $R_{Xe}^{\pi^+}$ from **Xe** target for positively charged pions in $z > 0.7$ slice.

p_t^2 (GeV^2)	$R_{Xe}^{K^+}$	statistical error(+/-)	total error(+/-)
0.0230	0.8011	0.0105	0.0428
0.0733	0.8059	0.0133	0.0458
0.1857	0.8799	0.0099	0.0488
0.3847	1.0743	0.0187	0.0613
0.5837	1.1214	0.0323	0.0689
0.7830	1.1292	0.0545	0.0820
0.9898	1.3820	0.0996	0.1247
1.2299	1.5173	0.1419	0.1641
1.6920	2.2071	0.2902	0.3140

Table 3.127: p_t^2 dependence of multiplicity ratio $R_{Xe}^{K^+}$ from **Xe** target for positively charged kaons in $0.2 < z < 0.4$ slice.

p_t^2 (GeV^2)	$R_{Xe}^{K^+}$	statistical error(+/-)	total error(+/-)
0.0241	0.7505	0.0138	0.0430
0.0736	0.7133	0.0153	0.0417
0.1872	0.7667	0.0106	0.0430
0.3886	0.7848	0.0158	0.0455
0.5887	0.8452	0.0229	0.0513
0.7886	0.9617	0.0351	0.0629
0.9872	1.0200	0.0479	0.0732
1.2296	1.1638	0.0622	0.0887
1.8430	1.3336	0.0771	0.1058

Table 3.128: p_t^2 dependence of multiplicity ratio $R_{Xe}^{K^+}$ from **Xe** target for positively charged kaons in $0.4 < z < 0.7$ slice.

p_t^2 (GeV^2)	$R_{Xe}^{K^+}$	statistical error(+/-)	total error(+/-)
0.0246	0.7471	0.0318	0.0516
0.0748	0.7240	0.0331	0.0514
0.1913	0.6716	0.0192	0.0412
0.3921	0.5923	0.0250	0.0407
0.5940	0.6505	0.0369	0.0511
0.7867	0.7328	0.0551	0.0680
0.9908	0.6034	0.0654	0.0732
1.2278	0.6563	0.0784	0.0861
1.8511	0.6937	0.0948	0.1020

Table 3.129: p_t^2 dependence of multiplicity ratio $R_{Xe}^{K^+}$ from **Xe** target for positively charged kaons in $z > 0.7$ slice.

$\mathbf{p_t^2}$ $\mathbf{(GeV^2)}$	$\mathbf{R_{Xe}^p}$	statistical error(+/-)	total error(+/-)
0.0229	**1.0277**	**0.0110**	**0.0499**
0.0733	**1.0891**	**0.0145**	**0.0535**
0.1869	**1.1223**	**0.0104**	**0.0540**
0.3868	**1.2834**	**0.0185**	**0.0633**
0.5852	**1.4665**	**0.0341**	**0.0771**
0.7818	**1.7241**	**0.0632**	**0.1030**
0.9880	**1.8321**	**0.1064**	**0.1371**
1.2243	**1.9304**	**0.1556**	**0.1803**
1.6849	**1.9529**	**0.2451**	**0.2618**

Table 3.130: $\mathbf{p_t^2}$ dependence of multiplicity ratio $\mathbf{R_{Xe}^p}$ from **Xe** target for protons in $\mathbf{0.2 < z < 0.4}$ slice.

$\mathbf{p_t^2}$ $\mathbf{(GeV^2)}$	$\mathbf{R_{Xe}^p}$	statistical error(+/-)	total error(+/-)
0.0237	**0.8030**	**0.0129**	**0.0400**
0.0741	**0.7821**	**0.0139**	**0.0394**
0.1852	**0.7912**	**0.0093**	**0.0385**
0.3873	**0.8859**	**0.0159**	**0.0447**
0.5875	**1.0222**	**0.0253**	**0.0545**
0.7953	**1.1658**	**0.0397**	**0.0678**
0.9886	**1.4557**	**0.0668**	**0.0958**
1.2212	**1.5131**	**0.0836**	**0.1099**
1.8790	**2.1137**	**0.01303**	**0.1641**

Table 3.131: $\mathbf{p_t^2}$ dependence of multiplicity ratio $\mathbf{R_{Xe}^p}$ from **Xe** target for protons in $\mathbf{0.4 < z < 0.7}$ slice.

$\mathbf{p_t^2}$ $\mathbf{(GeV^2)}$	$\mathbf{R_{Xe}^p}$	statistical error(+/-)	total error(+/-)
0.0239	**0.8227**	**0.0497**	**0.0631**
0.0755	**0.5273**	**0.0404**	**0.0474**
0.1927	**0.6385**	**0.0252**	**0.0393**
0.3852	**0.6421**	**0.0344**	**0.0458**
0.5910	**0.6375**	**0.0483**	**0.0569**
0.7872	**0.7213**	**0.0731**	**0.0806**
0.9877	**0.9305**	**0.1204**	**0.1282**
1.2329	**1.0112**	**0.1530**	**0.1603**
2.0002	**1.6100**	**0.2291**	**0.2414**

Table 3.132: $\mathbf{p_t^2}$ dependence of multiplicity ratio $\mathbf{R_{Xe}^p}$ from **Xe** target for protons in $\mathbf{z > 0.7}$ slice.

3.4 z dependence in three p_t^2 slices

The **z** dependence of R_A^h for three slices in p_t^2 is presented in Figure 3.4. The overall reduction of R_A^h with **z** was observed. At high p_t^2 range the **z** dependence is stronger which is more prominent for havier targets. At small values of **z** a strong dependence of R_A^h on p_t^2

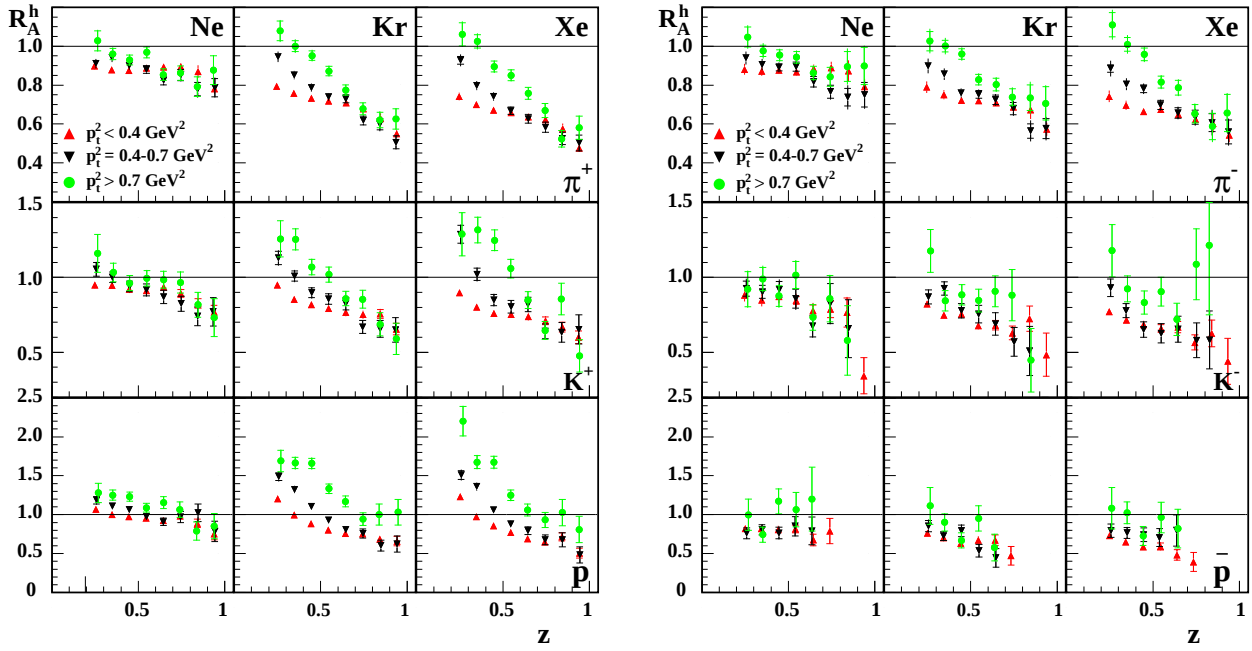

Figure 3.4: Dependence of R_A^h on **z** for three slices in p_t^2.

was found while for high **z** values there is almost no p_t^2 dependence for π^+, π^- and K^+. This consistency between different p_t values at high **z** range can be caused by the instantaneous hadronization since the main contribution into hadron transverse momentum assumed to be from quark rescatering process which is proportional to the production time and according to the **LUND** model it behaves as $\sim (1 - z)$. Thus with increasing of **z** this time goes down reducing the contribution from partonic effects into the hadronization process. That is why the p_t dependence disappears at high values of **z**. The corresponding data points shown in Figure 3.4 are tabulated in tables together with statistical and total errors.

z bin	$R_{Ne}^{\pi^+}$	statistical error(+/-)	total error(+/-)
0.0940	0.9236	0.0317	0.0456
0.1560	0.9089	0.0041	0.0332
0.2467	0.8978	0.0039	0.0330
0.3457	0.8793	0.0047	0.0311
0.4461	0.8748	0.0061	0.0302
0.5464	0.8879	0.0077	0.0301
0.6470	0.8933	0.0095	0.0312
0.7468	0.8939	0.0115	0.0327
0.8461	0.8695	0.0136	0.0411
0.9400	0.7813	0.0152	0.0343

Table 3.133: **z** dependence of multiplicity ratio $R_{Ne}^{\pi^+}$ from **Ne** target for positively charged pions in $0.0 < p_t^2 < 0.4$ **GeV²** slice.

z bin	$R_{Ne}^{\pi^+}$	statistical error(+/-)	total error(+/-)
0.1813	0.9924	0.0503	0.0619
0.2552	0.9101	0.0166	0.0371
0.3481	0.9412	0.0152	0.0371
0.4465	0.9009	0.0167	0.0362
0.5466	0.8800	0.0201	0.0348
0.6457	0.8237	0.0224	0.0352
0.7449	0.8508	0.0287	0.0354
0.8426	0.7789	0.0346	0.0409
0.9418	0.7868	0.0474	0.0566

Table 3.134: **z** dependence of multiplicity ratio $R_{Ne}^{\pi^+}$ from **Ne** target for positively charged pions in $0.4 < p_t^2 < 0.7$ **GeV²** slice.

z bin	$R_{Ne}^{\pi^+}$	statistical error(+/-)	total error(+/-)
0.2647	1.0281	0.0513	0.0635
0.3529	0.9585	0.0294	0.0446
0.4496	0.9287	0.0256	0.0405
0.5480	0.9682	0.0280	0.0423
0.6448	0.8541	0.0292	0.0407
0.7443	0.8616	0.0375	0.0477
0.8413	0.7920	0.0498	0.0610
0.9348	0.8769	0.0737	0.0814

Table 3.135: **z** dependence of multiplicity ratio $R_{Ne}^{\pi^+}$ from **Ne** target for positively charged pions in $p_t^2 > 0.7$ **GeV²** slice.

z bin	$R^{\pi^-}_{Ne}$	statistical error(+/-)	total error(+/-)
0.0941	0.9082	0.0301	0.0487
0.1555	0.8954	0.0042	0.0386
0.2459	0.8809	0.0041	0.0383
0.3453	0.8717	0.0052	0.0355
0.4459	0.8760	0.0068	0.0325
0.5465	0.8669	0.0085	0.0318
0.6470	0.8846	0.0107	0.0338
0.7469	0.8901	0.0129	0.0394
0.8470	0.8739	0.0152	0.0591
0.9410	0.7912	0.0174	0.0464

Table 3.136: **z** dependence of multiplicity ratio $\mathbf{R^{\pi^-}_{Ne}}$ from **Ne** target for negatively charged pions in $\mathbf{0.0 < p_t^2 < 0.4\ GeV^2}$ slice.

z bin	$R^{\pi^-}_{Ne}$	statistical error(+/-)	total error(+/-)
0.1820	0.9010	0.0463	0.0603
0.2543	0.9393	0.0172	0.0441
0.3481	0.9063	0.0154	0.0396
0.4460	0.8908	0.0180	0.0370
0.5450	0.8945	0.0234	0.0393
0.6458	0.8176	0.0271	0.0402
0.7435	0.7659	0.0338	0.0466
0.8428	0.7373	0.0454	0.0662
0.9399	0.7504	0.0630	0.0751

Table 3.137: **z** dependence of multiplicity ratio $\mathbf{R^{\pi^-}_{Ne}}$ from **Ne** target for negatively charged pions in $\mathbf{0.4 < p_t^2 < 0.7\ GeV^2}$ slice.

z bin	$R^{\pi^-}_{Ne}$	statistical error(+/-)	total error(+/-)
0.2648	1.0469	0.0511	0.0682
0.3532	0.9759	0.0297	0.0493
0.4485	0.9534	0.0273	0.0440
0.5475	0.9428	0.0304	0.0451
0.6453	0.8615	0.0344	0.0465
0.7422	0.8419	0.0484	0.0599
0.8415	0.8951	0.0768	0.0966
0.9386	0.8979	0.0960	0.1077

Table 3.138: **z** dependence of multiplicity ratio $\mathbf{R^{\pi^-}_{Ne}}$ from **Ne** target for negatively charged pions in $\mathbf{p_t^2 > 0.7\ GeV^2}$ slice.

z bin	$R_{Ne}^{K^+}$	statistical error(+/-)	total error(+/-)
0.0949	0.9308	0.1533	0.1614
0.1589	0.9643	0.0133	0.0540
0.2494	0.9501	0.0109	0.0527
0.3479	0.9460	0.0119	0.0527
0.4469	0.9204	0.0138	0.0519
0.5465	0.9110	0.0164	0.0521
0.6462	0.9359	0.0210	0.0550
0.7457	0.8934	0.0257	0.0549
0.8350	0.8256	0.0313	0.0547
0.9377	0.7698	0.0445	0.0611

Table 3.139: **z** dependence of multiplicity ratio $\mathbf{R_{Ne}^{K^+}}$ from **Ne** target for positively charged kaons in $\mathbf{0.0 < p_t^2 < 0.4\ GeV^2}$ slice.

z bin	$R_{Ne}^{K^+}$	statistical error(+/-)	total error(+/-)
0.1815	1.0619	0.1392	0.1507
0.2571	1.0542	0.0456	0.0732
0.3505	1.0009	0.0350	0.0647
0.4488	0.9402	0.0351	0.0620
0.5470	0.9165	0.0391	0.0633
0.6467	0.8694	0.0438	0.0644
0.7477	0.8244	0.0503	0.0673
0.8425	0.7398	0.0630	0.0747
0.9334	0.7703	0.0958	0.1045

Table 3.140: **z** dependence of multiplicity ratio $\mathbf{R_{Ne}^{K^+}}$ from **Ne** target for positively charged kaons in $\mathbf{0.4 < p_t^2 < 0.7\ GeV^2}$ slice.

z bin	$R_{Ne}^{K^+}$	statistical error(+/-)	total error(+/-)
0.2640	1.1601	0.1267	0.1415
0.3553	1.0333	0.0623	0.0838
0.4501	0.9621	0.0497	0.0721
0.5498	0.9947	0.0515	0.0746
0.6457	0.9853	0.0567	0.0780
0.7440	0.9668	0.0705	0.0879
0.8446	0.8174	0.0834	0.0945
0.9383	0.7317	0.1269	0.1330

Table 3.141: **z** dependence of multiplicity ratio $\mathbf{R_{Ne}^{K^+}}$ from **Ne** target for positively charged kaons in $\mathbf{p_t^2 > 0.7\ GeV^2}$ slice.

z bin	$R_{Ne}^{K^-}$	statistical error(+/-)	total error(+/-)
0.0949	0.7797	0.1571	0.1656
0.1588	0.8994	0.0154	0.0623
0.2472	0.8818	0.0136	0.0607
0.3460	0.8483	0.0159	0.0591
0.4457	0.8718	0.0209	0.0621
0.5455	0.8459	0.0260	0.0624
0.6426	0.7791	0.0356	0.0632
0.7440	0.7872	0.0547	0.0760
0.8392	0.7656	0.0981	0.1108
0.9364	0.3432	0.1204	0.1245

Table 3.142: **z** dependence of multiplicity ratio $\mathbf{R_{Ne}^{K^-}}$ from **Ne** target for negatively charged kaons in $\mathbf{0.0 < p_t^2 < 0.4\ GeV^2}$ slice.

z bin	$R_{Ne}^{K^-}$	statistical error(+/-)	total error(+/-)
0.1828	0.9470	0.1470	0.1601
0.2563	0.9256	0.0501	0.0798
0.3494	0.9032	0.0439	0.0748
0.4465	0.9194	0.0545	0.0823
0.5422	0.8577	0.0638	0.0859
0.6412	0.6751	0.0716	0.0847
0.7427	0.8258	0.1335	0.1445
0.8471	0.6577	0.1937	0.1987

Table 3.143: **z** dependence of multiplicity ratio $\mathbf{R_{Ne}^{K^-}}$ from **Ne** target for negatively charged kaons in $\mathbf{0.4 < p_t^2 < 0.7\ GeV^2}$ slice.

z bin	$R_{Ne}^{K^-}$	statistical error(+/-)	total error(+/-)
0.2656	0.9214	0.1165	0.1319
0.3520	0.9894	0.0769	0.1016
0.4459	0.8762	0.0696	0.0911
0.5430	1.0163	0.0895	0.1125
0.6418	0.7329	0.0854	0.0985
0.7403	0.8582	0.1548	0.1652
0.8419	0.5789	0.2319	0.2351

Table 3.144: **z** dependence of multiplicity ratio $\mathbf{R_{Ne}^{K^-}}$ from **Ne** target for negatively charged kaons in $\mathbf{p_t^2 > 0.7\ GeV^2}$ slice.

z bin	R^{p}_{Ne}	statistical error(+/-)	total error(+/-)
0.2536	1.0704	0.0124	0.0521
0.3476	1.0011	0.0104	0.0484
0.4459	0.9766	0.0119	0.0476
0.5446	0.9567	0.0151	0.0476
0.6438	0.9245	0.0209	0.0484
0.7419	0.9829	0.0340	0.0575
0.8412	0.8872	0.0546	0.0688
0.9394	0.7544	0.0764	0.0843

Table 3.145: **z** dependence of multiplicity ratio $\mathbf{R^{p}_{Ne}}$ from **Ne** target for protons in $\mathbf{0.0 < p_t^2 < 0.4\ GeV^2}$ slice.

z bin	R^{p}_{Ne}	statistical error(+/-)	total error(+/-)
0.2581	1.1845	0.0459	0.0723
0.3496	1.1093	0.0338	0.0623
0.4474	1.0657	0.0343	0.0609
0.5461	0.9744	0.0387	0.0601
0.6449	0.9079	0.0478	0.0642
0.7448	0.9714	0.0729	0.0861
0.8454	1.0231	0.1121	0.1220
0.9422	0.7851	0.1301	0.1353

Table 3.146: **z** dependence of multiplicity ratio $\mathbf{R^{p}_{Ne}}$ from **Ne** target for protons in $\mathbf{0.4 < p_t^2 < 0.7\ GeV^2}$ slice.

z bin	R^{p}_{Ne}	statistical error(+/-)	total error(+/-)
0.2687	1.2790	0.1238	0.1378
0.3517	1.2509	0.0657	0.0883
0.4502	1.2301	0.0580	0.0820
0.5470	1.0884	0.0568	0.0766
0.6459	1.1562	0.0761	0.0936
0.7404	1.0645	0.0990	0.1110
0.8373	0.7891	0.1190	0.1247
0.9396	0.8521	0.1622	0.1671

Table 3.147: **z** dependence of multiplicity ratio $\mathbf{R^{p}_{Ne}}$ from **Ne** target for protons in $\mathbf{p_t^2 > 0.7\ GeV^2}$ slice.

z bin	R^{p}_{Ne}	statistical error(+/-)	total error(+/-)
0.2512	0.8217	0.0263	0.0940
0.3438	0.8192	0.0251	0.0932
0.4417	0.8063	0.0333	0.0944
0.5412	0.8155	0.0505	0.1026
0.6434	0.6751	0.0753	0.1055
0.7395	0.7903	0.1620	0.1837

Table 3.148: **z** dependence of multiplicity ratio $\mathbf{R^{\bar{p}}_{Ne}}$ from **Ne** target for antiprotons in $\mathbf{0.0 < p_t^2 < 0.4\ GeV^2}$ slice.

z bin	R^{p}_{Ne}	statistical error(+/-)	total error(+/-)
0.2582	0.7611	0.0695	0.1086
0.3473	0.8070	0.0653	0.1099
0.4452	0.7635	0.0753	0.1125
0.5395	0.8506	0.1231	0.1544
0.6362	0.7918	0.1773	0.1974

Table 3.149: **z** dependence of multiplicity ratio $\mathbf{R^{\bar{p}}_{Ne}}$ from **Ne** target for antiprotons in $\mathbf{0.4 < p_t^2 < 0.7\ GeV^2}$ slice.

z bin	$R^{\bar{p}}_{Ne}$	statistical error(+/-)	total error(+/-)
0.2685	0.9993	0.1991	0.2272
0.3515	0.7429	0.0976	0.1271
0.4440	1.1716	0.1600	0.2051
0.5442	1.0635	0.2203	0.2492
0.6370	1.1993	0.4091	0.4299

Table 3.150: **z** dependence of multiplicity ratio $\mathbf{R^{\bar{p}}_{Ne}}$ from **Ne** target for antiprotons $\mathbf{p_t^2 > 0.7\ GeV^2}$ slice.

z bin	$R^{\pi^+}_{Kr}$	statistical error(+/-)	total error(+/-)
0.0940	0.9538	0.0330	0.0478
0.1558	0.8569	0.0039	0.0321
0.2462	0.7939	0.0034	0.0300
0.3454	0.7583	0.0042	0.0278
0.4459	0.7319	0.0052	0.0261
0.5465	0.7184	0.0065	0.0248
0.6467	0.7087	0.0079	0.0253
0.7465	0.6776	0.0092	0.0259
0.8462	0.6279	0.0105	0.0325
0.9394	0.5494	0.0117	0.0265

Table 3.151: **z** dependence of multiplicity ratio $\mathbf{R^{\pi^+}_{Kr}}$ from **Kr** target for positively charged pions in $\mathbf{0.0 < p_t^2 < 0.4\ GeV^2}$ slice.

z bin	$R_{Kr}^{\pi^+}$	statistical error(+/-)	total error(+/-)
0.1805	0.9929	0.0491	0.0614
0.2542	0.9459	0.0166	0.0392
0.3479	0.8517	0.0135	0.0337
0.4459	0.7872	0.0147	0.0312
0.5456	0.7401	0.0170	0.0299
0.6461	0.7296	0.0202	0.0319
0.7460	0.6181	0.0225	0.0316
0.8429	0.5993	0.0287	0.0410
0.9364	0.5057	0.0338	0.0402

Table 3.152: **z** dependence of multiplicity ratio $R_{Kr}^{\pi^+}$ from **Kr** target for positively charged pions in $0.4 < p_t^2 < 0.7$ **GeV²** slice.

z bin	$R_{Kr}^{\pi^+}$	statistical error(+/-)	total error(+/-)
0.2652	1.0787	0.0513	0.0654
0.3531	1.0001	0.0285	0.0461
0.4501	0.9514	0.0248	0.0415
0.5480	0.8719	0.0247	0.0381
0.6446	0.7742	0.0263	0.0371
0.7440	0.6778	0.0303	0.0388
0.8433	0.6200	0.0394	0.0497
0.9351	0.6258	0.0525	0.0591

Table 3.153: **z** dependence of multiplicity ratio $R_{Kr}^{\pi^+}$ from **Kr** target for positively charged pions in $p_t^2 > 0.7$ **GeV²** slice.

z bin	$R_{Kr}^{\pi^-}$	statistical error(+/-)	total error(+/-)
0.0941	0.9187	0.0332	0.0522
0.1552	0.8448	0.0041	0.0397
0.2458	0.7892	0.0037	0.0382
0.3452	0.7501	0.0046	0.0322
0.4456	0.7207	0.0058	0.0278
0.5459	0.7205	0.0073	0.0268
0.6472	0.7091	0.0089	0.0282
0.7468	0.6867	0.0106	0.0322
0.8457	0.6734	0.0124	0.0521
0.9401	0.5730	0.0137	0.0376

Table 3.154: **z** dependence of multiplicity ratio $R_{Kr}^{\pi^-}$ from **Kr** target for negatively charged pions in $0.0 < p_t^2 < 0.4$ **GeV²** slice.

z bin	$R^{\pi^-}_{Kr}$	statistical error(+/-)	total error(+/-)
0.1817	0.9463	0.0492	0.0661
0.2541	0.8986	0.0165	0.0463
0.3473	0.8564	0.0145	0.0392
0.4454	0.7594	0.0160	0.0328
0.5469	0.7518	0.0203	0.0337
0.6442	0.7245	0.0248	0.0369
0.7460	0.6792	0.0308	0.0430
0.8456	0.5641	0.0372	0.0564
0.9360	0.5764	0.0520	0.0628

Table 3.155: **z** dependence of multiplicity ratio $\mathbf{R^{\pi^-}_{Kr}}$ from **Kr** target for negatively charged pions in $\mathbf{0.4 < p_t^2 < 0.7\ GeV^2}$ slice.

z bin	$R^{\pi^-}_{Kr}$	statistical error(+/-)	total error(+/-)
0.2641	1.0261	0.0495	0.0700
0.3522	1.0009	0.0299	0.0520
0.4480	0.9596	0.0272	0.0453
0.5455	0.8284	0.0269	0.0400
0.6465	0.8025	0.0323	0.0443
0.7416	0.7383	0.0428	0.0538
0.8439	0.7350	0.0656	0.0858
0.9347	0.7057	0.0853	0.0956

Table 3.156: **z** dependence of multiplicity ratio $\mathbf{R^{\pi^-}_{Kr}}$ from **Kr** target for negatively charged pions in $\mathbf{p_t^2 > 0.7\ GeV^2}$ slice.

z bin	$R^{K^+}_{Kr}$	statistical error(+/-)	total error(+/-)
0.0948	1.2040	0.2152	0.2249
0.1590	1.0445	0.0145	0.0585
0.2490	0.9503	0.0106	0.0527
0.3474	0.8533	0.0108	0.0476
0.4473	0.8192	0.0124	0.0462
0.5467	0.7922	0.0146	0.0454
0.6451	0.7656	0.0177	0.0452
0.7453	0.7521	0.0218	0.0463
0.8450	0.7567	0.0293	0.0505
0.9370	0.6549	0.0381	0.0521

Table 3.157: **z** dependence of multiplicity ratio $\mathbf{R^{K^+}_{Kr}}$ from **Kr** target for positively charged kaons in $\mathbf{0.0 < p_t^2 < 0.4\ GeV^2}$ slice.

z bin	$R_{Kr}^{K^+}$	statistical error(+/-)	total error(+/-)
0.1828	1.1262	0.1369	0.1500
0.2558	1.1302	0.0456	0.0765
0.3497	1.0088	0.0344	0.0647
0.4480	0.8969	0.0330	0.0588
0.5456	0.8560	0.0360	0.0588
0.6460	0.8246	0.0411	0.0608
0.7431	0.6691	0.0426	0.0560
0.8445	0.6566	0.0559	0.0663
0.9332	0.6498	0.0826	0.0898

Table 3.158: **z** dependence of multiplicity ratio $\mathbf{R_{Kr}^{K^+}}$ from **Kr** target for positively charged kaons in $\mathbf{0.4 < p_t^2 < 0.7\ GeV^2}$ slice.

z bin	$R_{Kr}^{K^+}$	statistical error(+/-)	total error(+/-)
0.2672	1.2579	0.1207	0.1387
0.3542	1.2545	0.0701	0.0978
0.4493	1.0687	0.0521	0.0780
0.5474	1.0190	0.0505	0.0749
0.6453	0.8587	0.0478	0.0668
0.7436	0.8545	0.0599	0.0758
0.8436	0.6871	0.0770	0.0856
0.9372	0.5899	0.1048	0.1096

Table 3.159: **z** dependence of multiplicity ratio $\mathbf{R_{Kr}^{K^+}}$ from **Kr** target for positively charged kaons in $\mathbf{p_t^2 > 0.7\ GeV^2}$ slice.

z bin	$R_{Kr}^{K^-}$	statistical error(+/-)	total error(+/-)
0.0950	0.7225	0.1796	0.1838
0.1586	0.8900	0.0158	0.0509
0.2471	0.8240	0.0130	0.0466
0.3453	0.7478	0.0145	0.0431
0.4458	0.7555	0.0187	0.0451
0.5443	0.6775	0.0220	0.0429
0.6433	0.6807	0.0319	0.0488
0.7409	0.6288	0.0452	0.0567
0.8410	0.7239	0.0840	0.0928
0.9373	0.4830	0.1441	0.1466

Table 3.160: **z** dependence of multiplicity ratio $\mathbf{R_{Kr}^{K^-}}$ from **Kr** target for negatively charged kaons in $\mathbf{0.0 < p_t^2 < 0.4\ GeV^2}$ slice.

z bin	$R^{K^-}_{Kr}$	statistical error(+/-)	total error(+/-)
0.1822	1.0073	0.1685	0.1772
0.2555	0.8687	0.0469	0.0665
0.3478	0.9263	0.0444	0.0671
0.4460	0.7776	0.0484	0.0642
0.5459	0.7547	0.0592	0.0720
0.6425	0.6897	0.0753	0.0841
0.7506	0.5701	0.0964	0.1013
0.8412	0.5085	0.1632	0.1655
0.9300	0.0815	0.1183	0.1184

Table 3.161: **z** dependence of multiplicity ratio $\mathbf{R^{K^-}_{Kr}}$ from **Kr** target for negatively charged kaons in $\mathbf{0.4 < p_t^2 < 0.7\ GeV^2}$ slice.

z bin	$R^{K^-}_{Kr}$	statistical error(+/-)	total error(+/-)
0.2673	1.1766	0.1434	0.1570
0.3526	0.8437	0.0681	0.0821
0.4493	0.8831	0.0679	0.0831
0.5459	0.8454	0.0766	0.0893
0.6424	0.9070	0.1025	0.1137
0.7394	0.8824	0.1711	0.1777
0.8492	0.4470	0.2123	0.2137

Table 3.162: **z** dependence of multiplicity ratio $\mathbf{R^{K^-}_{Kr}}$ from **Kr** target for negatively charged kaons in $\mathbf{p_t^2 > 0.7\ GeV^2}$ slice.

z bin	R^{p}_{Kr}	statistical error(+/-)	total error(+/-)
0.2523	1.2067	0.0121	0.0586
0.3467	0.9977	0.0096	0.0480
0.4448	0.8821	0.0104	0.0429
0.5444	0.8032	0.0126	0.0399
0.6431	0.7589	0.0174	0.0398
0.7430	0.7520	0.0265	0.0443
0.8418	0.6852	0.0431	0.0539
0.9413	0.6601	0.0622	0.0696

Table 3.163: **z** dependence of multiplicity ratio $\mathbf{R^{p}_{Kr}}$ from **Kr** target for protons in $\mathbf{0.0 < p_t^2 < 0.4\ GeV^2}$ slice.

z bin	R^{p}_{Kr}	statistical error(+/-)	total error(+/-)
0.2581	1.4881	0.0495	0.0859
0.3489	1.3229	0.0349	0.0715
0.4461	1.1054	0.0323	0.0613
0.5457	0.9272	0.0348	0.0559
0.6462	0.8082	0.0415	0.0564
0.7441	0.7580	0.0569	0.0672
0.8482	0.6030	0.0713	0.0768
0.9427	0.6234	0.1043	0.1084

Table 3.164: **z** dependence of multiplicity ratio $\mathbf{R^{p}_{Kr}}$ from **Kr** target for protons in $\mathbf{0.4 < p_t^2 < 0.7\ GeV^2}$ slice.

z bin	R^{p}_{Kr}	statistical error(+/-)	total error(+/-)
0.2692	1.6904	0.1382	0.1595
0.3524	1.6629	0.0719	0.1064
0.4489	1.6580	0.0655	0.1020
0.5478	1.3331	0.0600	0.0869
0.6444	1.1698	0.0694	0.0887
0.7451	0.9432	0.0825	0.0937
0.8380	1.0016	0.1367	0.1446
0.9479	1.0315	0.1659	0.1729

Table 3.165: **z** dependence of multiplicity ratio $\mathbf{R^{p}_{Kr}}$ from **Kr** target for protons in $\mathbf{p_t^2 > 0.7\ GeV^2}$ slice.

z bin	R^{p}_{Kr}	statistical error(+/-)	total error(+/-)
0.2493	0.7647	0.0214	0.0865
0.3430	0.7019	0.0200	0.0794
0.4418	0.6336	0.0258	0.0740
0.5430	0.6706	0.0406	0.0839
0.6416	0.6712	0.0685	0.1005
0.7335	0.4720	0.1197	0.1305

Table 3.166: **z** dependence of multiplicity ratio $\mathbf{R^{\bar{p}}_{Kr}}$ from **Kr** target for antiprotons in $\mathbf{0.0 < p_t^2 < 0.4\ GeV^2}$ slice.

z bin	R^{p}_{Kr}	statistical error(+/-)	total error(+/-)
0.2557	0.8528	0.0743	0.1194
0.3434	0.7243	0.0575	0.0980
0.4459	0.7927	0.0744	0.1144
0.5479	0.5367	0.0810	0.1001
0.6460	0.4450	0.1211	0.1306

Table 3.167: **z** dependence of multiplicity ratio $\mathbf{R^{\bar{p}}_{Kr}}$ from **Kr** target for antiprotons in $\mathbf{0.4 < p_t^2 < 0.7\ GeV^2}$ slice.

z bin	R^{p}_{Kr}	statistical error(+/-)	total error(+/-)
0.2649	1.1137	0.2364	0.2661
0.3499	0.9020	0.1106	0.1483
0.4455	0.6695	0.0956	0.1205
0.5455	0.9534	0.1621	0.1929
0.6382	0.5777	0.1725	0.1837

Table 3.168: **z** dependence of multiplicity ratio $\mathbf{R^{\bar{p}}_{Kr}}$ from **Kr** target for antiprotons in $\mathbf{p_t^2 > 0.7\ GeV^2}$ slice.

z bin	$R^{\pi^+}_{Xe}$	statistical error(+/-)	total error(+/-)
0.0940	0.9073	0.0386	0.0513
0.1558	0.8245	0.0045	0.0315
0.2461	0.7417	0.0040	0.0295
0.3456	0.7002	0.0047	0.0265
0.4455	0.6719	0.0059	0.0242
0.5465	0.6583	0.0073	0.0231
0.6465	0.6362	0.0088	0.0233
0.7460	0.6229	0.0104	0.0246
0.8457	0.5751	0.0119	0.0318
0.9403	0.4765	0.0129	0.0251

Table 3.169: **z** dependence of multiplicity ratio $\mathbf{R^{\pi^+}_{Xe}}$ from **Xe** target for positively charged pions in $\mathbf{0.0 < p_t^2 < 0.4\ GeV^2}$ slice.

z bin	$R^{\pi^+}_{Xe}$	statistical error(+/-)	total error(+/-)
0.1804	1.0593	0.0610	0.0729
0.2546	0.9270	0.0195	0.0414
0.3486	0.7967	0.0153	0.0334
0.4457	0.7408	0.0169	0.0309
0.5459	0.6681	0.0191	0.0293
0.6468	0.6266	0.0219	0.0305
0.7460	0.5832	0.0258	0.0332
0.8442	0.5250	0.0315	0.0414
0.9404	0.5027	0.0403	0.0463

Table 3.170: **z** dependence of multiplicity ratio $\mathbf{R^{\pi^+}_{Xe}}$ from **Xe** target for positively charged pions in $\mathbf{0.4 < p_t^2 < 0.7\ GeV^2}$ slice.

z bin	$R^{\pi^+}_{Xe}$	statistical error(+/-)	total error(+/-)
0.2652	1.0614	0.0596	0.0728
0.3522	1.0244	0.0344	0.0514
0.4490	0.8953	0.0283	0.0422
0.5472	0.8505	0.0288	0.0404
0.6456	0.7573	0.0311	0.0403
0.7431	0.6693	0.0356	0.0429
0.8390	0.5238	0.0426	0.0503
0.9408	0.5810	0.0599	0.0654

Table 3.171: **z** dependence of multiplicity ratio $\mathbf{R^{\pi^+}_{Xe}}$ from **Xe** target for positively charged pions in $\mathbf{p_t^2 > 0.7\ GeV^2}$ slice.

z bin	$R^{\pi^-}_{Xe}$	statistical error(+/-)	total error(+/-)
0.0941	0.8972	0.0391	0.0568
0.1551	0.8246	0.0048	0.0400
0.2457	0.7421	0.0043	0.0377
0.3449	0.6961	0.0052	0.0310
0.4457	0.6639	0.0066	0.0263
0.5460	0.6755	0.0084	0.0268
0.6458	0.6499	0.0101	0.0272
0.7459	0.6232	0.0119	0.0323
0.8472	0.6029	0.0139	0.0511
0.9400	0.5421	0.0159	0.0388

Table 3.172: **z** dependence of multiplicity ratio $\mathbf{R^{\pi^-}_{Xe}}$ from **Xe** target for negatively charged pions in $\mathbf{0.0 < p_t^2 < 0.4\ GeV^2}$ slice.

z bin	$R^{\pi^-}_{Xe}$	statistical error(+/-)	total error(+/-)
0.1803	0.9904	0.0596	0.0764
0.2538	0.8849	0.0193	0.0486
0.3468	0.8037	0.0166	0.0390
0.4460	0.7809	0.0195	0.0357
0.5436	0.6975	0.0232	0.0351
0.6449	0.6567	0.0278	0.0377
0.7440	0.6350	0.0353	0.0467
0.8418	0.6067	0.0466	0.0680
0.9372	0.5585	0.0612	0.0713

Table 3.173: **z** dependence of multiplicity ratio $\mathbf{R^{\pi^-}_{Xe}}$ from **Xe** target for negatively charged pions in $\mathbf{0.4 < p_t^2 < 0.7\ GeV^2}$ slice.

z bin	$R^{\pi^-}_{Xe}$	statistical error(+/-)	total error(+/-)
0.2640	1.1100	0.0624	0.0839
0.3515	1.0089	0.0352	0.0566
0.4495	0.9583	0.0322	0.0488
0.5463	0.8154	0.0315	0.0440
0.6460	0.7867	0.0382	0.0489
0.7425	0.6525	0.0473	0.0568
0.8433	0.5874	0.0679	0.0831
0.9295	0.6569	0.0956	0.1048

Table 3.174: **z** dependence of multiplicity ratio $\mathbf{R^{\pi^-}_{Xe}}$ from **Xe** target for negatively charged pions in $\mathbf{p_t^2 > 0.7\ GeV^2}$ slice.

z bin	$R^{K^+}_{Xe}$	statistical error(+/-)	total error(+/-)
0.0946	1.0747	0.2391	0.2461
0.1592	1.0267	0.0167	0.0582
0.2489	0.8978	0.0123	0.0503
0.3474	0.8018	0.0124	0.0453
0.4467	0.7590	0.0141	0.0436
0.5465	0.7527	0.0169	0.0442
0.6458	0.7391	0.0209	0.0453
0.7452	0.7108	0.0252	0.0461
0.8426	0.6680	0.0323	0.0486
0.9372	0.5996	0.0427	0.0537

Table 3.175: **z** dependence of multiplicity ratio $\mathbf{R^{K^+}_{Xe}}$ from **Xe** target for positively charged kaons in $\mathbf{0.0 < p_t^2 < 0.4\ GeV^2}$ slice.

z bin	$R^{K^+}_{Xe}$	statistical error(+/-)	total error(+/-)
0.1822	1.3107	0.1855	1.1987
0.2556	1.2877	0.0597	0.0919
0.3502	1.0205	0.0412	0.0691
0.4470	0.8484	0.0382	0.0599
0.5466	0.8041	0.0411	0.0600
0.6452	0.8200	0.0483	0.0657
0.7448	0.6402	0.0498	0.0607
0.8399	0.6321	0.0660	0.0744
0.9385	0.6524	0.0971	0.1034

Table 3.176: **z** dependence of multiplicity ratio $\mathbf{R^{K^+}_{Xe}}$ from **Xe** target for positively charged kaons in $\mathbf{0.4 < p_t^2 < 0.7\ GeV^2}$ slice.

z bin	$R_{Xe}^{K^+}$	statistical error(+/-)	total error(+/-)
0.2635	**0.7939**	**0.1443**	**0.1604**
0.3545	**1.2886**	**0.0858**	**0.1117**
0.4518	**1.3170**	**0.0689**	**0.0967**
0.5451	**1.2483**	**0.0620**	**0.0848**
0.6452	**0.8479**	**0.0565**	**0.0729**
0.7431	**0.6455**	**0.0594**	**0.0690**
0.8381	**0.8559**	**0.1061**	**0.1158**
0.9437	**0.4763**	**0.1082**	**0.1112**

Table 3.177: **z** dependence of multiplicity ratio $\mathbf{R_{Xe}^{K^+}}$ from **Xe** target for positively charged kaons in $\mathbf{p_t^2 > 0.7\ GeV^2}$ slice.

z bin	$R_{Xe}^{K^-}$	statistical error(+/-)	total error(+/-)
0.0950	**1.1124**	**0.2738**	**0.2804**
0.1582	**0.9034**	**0.0192**	**0.0527**
0.2474	**0.7719**	**0.0149**	**0.0445**
0.3456	**0.7139**	**0.0169**	**0.0423**
0.4455	**0.6839**	**0.0211**	**0.0427**
0.5461	**0.6586**	**0.0261**	**0.0443**
0.6437	**0.6687**	**0.0376**	**0.0523**
0.7417	**0.5657**	**0.0504**	**0.0590**
0.8494	**0.6258**	**0.0900**	**0.0962**
0.9319	**0.4394**	**0.1543**	**0.1563**

Table 3.178: **z** dependence of multiplicity ratio $\mathbf{R_{Xe}^{K^-}}$ from **Xe** target for negatively charged kaons in $\mathbf{0.0 < p_t^2 < 0.4\ GeV^2}$ slice.

z bin	$R_{Xe}^{K^-}$	statistical error(+/-)	total error(+/-)
0.1866	**1.0084**	**0.1936**	**0.2012**
0.2543	**0.9303**	**0.0584**	**0.0773**
0.3442	**0.7785**	**0.0471**	**0.0633**
0.4456	**0.6518**	**0.0512**	**0.0622**
0.5468	**0.6263**	**0.0641**	**0.0726**
0.6455	**0.6533**	**0.0868**	**0.0938**
0.7451	**0.5799**	**0.1158**	**0.1200**
0.8263	**0.5824**	**0.1941**	**0.1967**

Table 3.179: **z** dependence of multiplicity ratio $\mathbf{R_{Xe}^{K^-}}$ from **Xe** target for negatively charged kaons in $\mathbf{0.4 < p_t^2 < 0.7\ GeV^2}$ slice.

z bin	$R_{Xe}^{K^-}$	statistical error(+/-)	total error(+/-)
0.2637	1.1789	0.1743	0.1857
0.3525	0.9233	0.0867	0.1002
0.4497	0.8328	0.0779	0.0901
0.5461	0.9047	0.0957	0.1076
0.6375	0.7190	0.1078	0.1147
0.7507	1.0880	0.2379	0.2451
0.8256	1.2152	0.4661	0.4708

Table 3.180: **z** dependence of multiplicity ratio $\mathbf{R_{Xe}^{K^-}}$ from **Xe** target for negatively charged kaons in $\mathbf{p_t^2 > 0.7\ GeV^2}$ slice.

z bin	R_{Xe}^{p}	statistical error(+/-)	total error(+/-)
0.2525	1.2323	0.0144	0.0605
0.3466	0.9735	0.0112	0.0473
0.4451	0.8533	0.0121	0.0421
0.5441	0.7718	0.0146	0.0392
0.6431	0.6889	0.0195	0.0379
0.7421	0.6505	0.0288	0.0421
0.8407	0.7152	0.0523	0.0622
0.9421	0.5071	0.0637	0.0680

Table 3.181: **z** dependence of multiplicity ratio $\mathbf{R_{Xe}^{p}}$ from **Xe** target for protons in $\mathbf{0.0 < p_t^2 < 0.4\ GeV^2}$ slice.

z bin	R_{Xe}^{p}	statistical error(+/-)	total error(+/-)
0.2579	1.5092	0.0580	0.0918
0.3484	1.3602	0.0419	0.0766
0.4449	1.0603	0.0372	0.0623
0.5456	0.8780	0.0393	0.0571
0.6442	0.7943	0.0487	0.0614
0.7446	0.6761	0.0634	0.0710
0.8437	0.6765	0.0902	0.0957
0.9443	0.4832	0.1044	0.1069

Table 3.182: **z** dependence of multiplicity ratio $\mathbf{R_{Xe}^{p}}$ from **Xe** target for protons in $\mathbf{0.4 < p_t^2 < 0.7\ GeV^2}$ slice.

z bin	R^{p}_{Xe}	statistical error(+/-)	total error(+/-)
0.2689	2.2011	0.1902	0.2167
0.3511	1.6757	0.0834	0.1149
0.4477	1.6727	0.0773	0.1105
0.5453	1.2491	0.0681	0.0901
0.6420	1.0608	0.0763	0.0913
0.7436	0.9320	0.0986	0.1080
0.8431	1.0264	0.1694	0.1762
0.9408	0.8090	0.1700	0.1742

Table 3.183: **z** dependence of multiplicity ratio $\mathbf{R^{p}_{Xe}}$ from **Xe** target for protons in $\mathbf{p_t^2 > 0.7\ GeV^2}$ slice.

z bin	R^{p}_{Xe}	statistical error(+/-)	total error(+/-)
0.2497	0.7303	0.0239	0.0835
0.3428	0.6485	0.0224	0.0745
0.4437	0.5886	0.0290	0.0707
0.5430	0.5920	0.0445	0.0787
0.6393	0.4834	0.0671	0.0855
0.7344	0.3929	0.1224	0.1298

Table 3.184: **z** dependence of multiplicity ratio $\mathbf{R^{\bar{p}}_{Xe}}$ from **Xe** target for antiprotons in $\mathbf{0.0 < p_t^2 < 0.4\ GeV^2}$ slice.

z bin	R^{p}_{Xe}	statistical error(+/-)	total error(+/-)
0.2565	0.7949	0.0863	0.1226
0.3497	0.7657	0.0694	0.1089
0.4463	0.7416	0.0880	0.1198
0.5378	0.7059	0.1136	0.1374
0.6358	0.7970	0.2011	0.2193

Table 3.185: **z** dependence of multiplicity ratio $\mathbf{R^{\bar{p}}_{Xe}}$ from **Xe** target for antiprotons in $\mathbf{0.4 < p_t^2 < 0.7\ GeV^2}$ slice.

z bin	$R^{\bar{p}}_{Xe}$	statistical error(+/-)	total error(+/-)
0.2614	1.0839	0.2661	0.2914
0.3493	1.0229	0.1395	0.1790
0.4429	0.7270	0.1227	0.1463
0.5468	0.9633	0.1974	0.2239
0.6437	0.8221	0.2474	0.2633

Table 3.186: **z** dependence of multiplicity ratio $\mathbf{R^{\bar{p}}_{Xe}}$ from **Xe** target for antiprotons in $\mathbf{p_t^2 > 0.7\ GeV^2}$ slice.

3.5 Conclusion

The first multidimensional kinematic dependencies of hadron multiplicity ratio $\mathbf{R^h_A}$ have been extracted for pions($\boldsymbol{\pi}^+$, $\boldsymbol{\pi}^-$), kaons($\mathbf{K}^+$, $\mathbf{K}^-$) and protons($\mathbf{p}$, $\bar{\mathbf{p}}$) on neon, krypton and xenon targets relative to deuterium. The raw hadron yields are corrected from **RICH** misidentification effects which are found to be essential for protons and kaons and practically not relevant for pions. Using the corrected hadron yields the multidimensional nuclear attenuation effect is considered. For $\boldsymbol{\pi}^+$ and $\boldsymbol{\pi}^-$ the behaviour of $\mathbf{R^h_A}$ was about the same within the experimental uncertainties. The dependence of $\mathbf{R^{K^+}_A}$ on $\boldsymbol{\nu}$ for positevely charged kaons was found to be different from $\mathbf{R^{\pi^+}_A}$, $\mathbf{R^{\pi^-}_A}$ and $\mathbf{R^{K^-}_A}$ at high values of **z** which might be the result of different modification of fragmentation functions in nuclear medium. Proton data show a significant difference from the other hadrons which can be explained by a contribution of knock-out processes, in addition to the fragmentation process. The idea is that apart from fragmentation process some protons might be knock-outed from nuclei due to the final state interaction. The expected spectrum for these protons should lie at small momentum range which reflected in data by the smallest **z** slice.

Looking on **z** dependence of $\mathbf{R^h_A}$ in three slices of $\boldsymbol{\nu}$ we have found that the attenuation is small for positively charged kaons than it is for negatively charged ones. This phenomena might be a reflection of transformation of proton into a ($\mathbf{K^+\Lambda}$) pair inside a nucleus which is suppressed for negatively charged kaons due to the quark content. We also see that the Cronin effect is suppressed at large values of **z**. A possible explanation based on the phenomenology approach is that at high **z** values the production time is very small thus the contribution

from partonic effects is highly suppressed. On the other hand, it is assumed that the main contribution into transverse momentum broadening comes from the partonic effects.

The hadron multiplicity ratio also depends on azimuthal angle ϕ but our experimental data show no ϕ dependence within the experimental uncertainties. It is also important to mention almost no $\mathbf{Q^2}$ dependence for the nuclear attenuation. Because in the **HERMES** kinematics $\mathbf{Q^2}$ and $\mathbf{x_{Bj}}$ are strongly correlated the same is true for $\mathbf{x_{Bj}}$ dependences.

Having the first multidimensional data of the nuclear attenuation for charged pions, kaons and proton-antiprotons from neon, krypton and xenon targets, it is important to check different models which based on the one-dimensional approach and make a new predictions for hadronization process in nuclear medium. These new more detailed data provide a great opportunity for such a test of various model predictions in wide kinematic regime.

Acknowledgements

I would like to express my thanks of gratitude to the HERMES Yerevan groupe, specially the group leader and my scientific supervisor professor Norik Akopov for the excelent opportunity to deal with the excelent data provided by the HERMES experiment. It has been really amazing and I was enjoyed almost every day dealing with these small guys : hadrons, which sometimes were insufferable(there is a one named pi0).

Thanks to all of you R. Avakian A. Avetisyan, L. Grigoryan, G. Elbakyan, H. Marukyan, Z. Akopov, A. Movsisyan and A. Petrosyan for your help and support during these years.

I am very appreciative of the HERMES management Klaus Rith, Gunar Schnell, Marco Contalbrigo, Ami Rostomyan for supporting my attendence to various conferences where I've learned many things and found to me that not everithing is written in textbooks, although I was not so naive...

I would like to thank to Achim Hillenbrand and Sylvester Joosten, I've worked with on the nice topic called multiplicity.

I also sincerely appreciate Hamlet Mkrtchyan and Jora Arakelyan for their proofreading and constructive remarks of the thesis. Many thanks to Mareta Hakobyan for her huge support to complete the official part of this thesis which I would never did myself.

Last but not least, I greatly appreciate my family for their patience and love during all this time.

References

[1]. *John C. Collins et al., Factorization for hard exclusive electroproduction of mesons in QCD, Phys. Rev. D 56, 2982âĂŞ3006 (1997).* 5

[2]. *John C. Collins, Universality of soft and collinear factors in hard scattering factorization, Phys.Rev.Lett. 93 (2004) 252001.* 6

[3]. *L. Osborne et al., Electroproduction of hadrons from nuclei, Phys.Rev.Lett. 40 (1978) 1624.* 6

[4]. *J. Ashman et al., Comparison of forward hadrons produced in muon interactions on nuclear targets and deuterium, [EMC] Z. Phys. C52 (1991) 1.* 6, 8, 41

[5]. *A. Airapetian et al., Hadronization in Semi-inclusive deep inelastic scattering on nuclei, Nucl. Phys. B 780 (2007) 1-27.* 6, 41

[6]. *W.K. Brooks et al., Studies of parton propogation and hadron formation in the space-time domain, AIP Conf.Proc. 1056 (2008) 215-222.* 6

[7]. *L. Grigoryan (Yerevan Phys. Inst.), Study of the multiplicity of hadrons on nuclei., Armenian J.Phys. 5 (2012) 95-100.* 6

[8]. *B. Andersson et al., Parton fragmentation and string dynamics, Phys.Rept. 97 (1983) 31-45.* 7, 34

[9]. *A. Airapetian et al., Hadron formation in deep-inelastic positron scattering from* ^{14}**N** *and* ^{2}**H** *, Eur. Phys. J. C 20 (2001) 479-486.* 7

[10]. *N. Akopov, L. Grigoryan, Z. Akopov, Study of the hadronization process in cold nuclear medium, Eur.Phys.J C(2010) 70 5-14.* 8

[11]. *B. Kopeliovich, J. Nemchik, E. Predazzi, Nuclear hadronization : Within or without?, Nucl.Phys. A740 (2004) 211-245.* 11, 78

[12]. *A. Accardi, V. Muccifora, H.J. Pirner, Hadron production in deep inelastic lepton nucleuse scattering, Nucl.Phys. A720 (2003) 131-156.* 13

[13]. *T. Falter, W. Cassing, K. Gallmaiser, U. Mosel, Hadron formation and attenuation in deep inelastic lepton scattering off nuclei, Phys.Lett. B594 (2004) 61-68.* 14

[14]. *HERMES Collaboration, A. Airapetian et al., Nucl. Instrum. Meth. A540, 68 (2005), physics/0408137.* 17

[15]. *HERMES Collaboration, K. Ackerstaff et al., Nucl. Instrum. Meth. A417, 230 (1998), hep-ex/9806008.* 17

[16]. *M. G. Beuzekom, E. Garutti, D. Heesbeen, J. J. M. Steijger, and J. Visser, First experience with the HERMES silicon detector, Nucl. Instrum. Meth. A461, 247 (2001).* 19

[17]. *J. T. Brack et al., The HERMES forward tracking chambers: Construction, operation and aging effects, Nucl. Instrum. Meth. A469, 47 (2001).* 19

[18]. *A. Andreev et al., Multiwire proportional chambers in the HERMES experiment, Nucl. Instrum. Meth. A465, 482 (2001).* 19

[19]. *S. Bernreuther et al., The HERMES back drift chambers, Nucl. Instrum. Meth. A416, 45 (1998), hep-ex/9803005.* 19

[20]. *H. Avakian et al., Performance of the electromagnetic calorimeter of the HERMES experiment, Nucl. Instrum. Meth. A417, 69 (1998), hep-ex/9810004.* 21

[21]. *N. Akopov et al., The HERMES dual-radiator ring imaging Cherenkov detector, Nucl. Instrum. Meth. A479, 511 (2002), physics/0104033.* 21

[22]. *U. Elschenbroich, Analysis of luminosity monitor data for different years, HERMES internal note 02-013.* 24

[23]. *Hrayr H. Matevosyan (Adelaide U.), Wolfgang Bentz (Tokai U., Hiratsuka), Ian C. Cloet (Washington U., Seattle & Adelaide U.), Anthony W. Thomas (Adelaide U.). Nov 2011. 13 pp., Transverse momentum dependent fragmenatation and quark distribution functions from the NJL-jet model, Analysis of luminosity monitor data for different years, Phys.Rev. D85 (2012) 014021.* 31

[24]. *S.Mert Aybat (NIKHEF, Amsterdam & Vrije U., Amsterdam), Ted C. Rogers (Vrije U., Amsterdam). Jan 2011. 22 pp., TMD parton distribution and fragmentation functions with QCD evolution., Phys.Rev. D83 (2011) 114042.* 31

[25]. *S.Mert Aybat (NIKHEF, Amsterdam), John C. Collins (Penn State U.), Jian-Wei Qiu (Brookhaven & YITP, Stony Brook), Ted C. Rogers (Vrije U., Amsterdam & YITP, Stony Brook). Oct 2011. 16 pp., The QCD evolution of the Sivers function, Phys.Rev. D85 (2012) 034043.* 31

[26]. *P. Schweitzer, T. Teckentrup and A. Metz, Intrinsic transverse parton momenta in deeply inelastic reactions, Phys. Rev. D81, 094019 (2010).* 31

[27]. *ÌĹ M. Glück, E. Reya and A. Vogt, Dynamical parton distributions revisited, Eur. Phys. J. C5, 461âĂŞ470 (1998).* 34

[28]. *A. D. Martin, R. G. Roberts, W. J. Stirling and R. S. Thorne, Parton distributions and the LHC: W and Z production, Eur. Phys. J. C14, 133âĂŞ145 (2000).* 34

[29]. *J. Pumplin et al., New generation of parton distributions with uncertainties from global QCD analysis, JHEP 07, 012, 1âĂŞ47 (2002).* 34

[31]. *T. Sjostrand, L. Lonnblad, S. Mrenna, and P. Skands, (2003), hep-ph/0308153.* 35

[30]. *CERN Application Software Group. Geant , Detector Descriprion and Simulation Tool. CERN Program Library Long Writeup, W5013, 1994.* 35

[32]. *L. Mankiewicz, A. Schäfer and M. Veltri, PEPSI: A Monte Carlo generator for polarized leptoproduction, Comput. Phys. Commun. 71, 305âĂŞ318 (1992).* 36

[33]. *G. Ingelman, A. Edin and J. Rathsman, LEPTO 6.5 - A Monte Carlo Generator for Deep Inelastic Lepton-Nucleon Scattering, Comput. Phys. Commun.101, 108âĂŞ134 (1997).* 36

[34]. *A.C. Miller Applying radiative corrections to ratios of cross sections for Deeply Inelastic Scattering, HERMES Internal Note.* 37

[35]. *A. Airapetian et al, Multidimensional study of hadronization in nuclei, Eur. Phys. J. A 47 (2011) 113.* 40

[36]. *A. Accardi et al., Parton propagation and fragmentation in QCD matter, Riv. Nuovo Cim. 32, 439 (2010).* 41

[37]. *J.W. Cronin, H. J. Frisch, M. J. Shochet, J. P. Boymond, R.Mermod, P. A. Piroue and R. L. Sumner, Production of hadrons with large transverse momentum at 200-GeV, 300-GeV, and 400-GeV, Phys. Rev. D 11 (1975) 3105.* 78

[38]. *A. Airapetian et al., Transverse momentum broadening of hadrons produced in semi-inclusive deep-inelastic scattering on nuclei, Phys. Lett. B 684 (2010) 114-118.* 78

[39]. *B.Z. Kopeliovich (Heidelberg, Max Planck Inst. & Regensburg U. & Dubna, JINR), J. Nemchik (Kosice, IEF), A. Schafer (Regensburg U.), A.V. Tarasov*

(Heidelberg, Max Planck INst. & *Regensburg U.* & *Dubna, JINR), Cronin effect in hadron production off nuclei, Phys. Rev. Lett. 88, 232303 (2002).* 78

[40]. *Alberto Accardi, Cronin effect in proton-nucleus collisions: a survey of theoretical models, arXiv:hep-ph/0212148.* 78